Tangent fermions: massless fermions on a lattice

Proefschrift

ter verkrijging van
de graad van doctor aan de Universiteit Leiden,
op gezag van rector magnificus prof. dr. ir. H. Bijl,
volgens besluit van het college voor promoties
te verdedigen op woensdag 3 juli 2024
klokke 13:45

door

Álvaro Donís Vela

geboren te Valladolid, Spanje
in 1996

Promotores: Prof. dr. C. W. J. Beenakker
Prof. dr. J. Tworzydło (University of Warsaw)

Promotiecommissie: Prof. dr. S. J. van der Molen
Prof. dr. A. Achúcarro
Dr. V. Cheianov
Prof. dr. D. Tong (University of Cambridge)
Dr. M. Wimmer (Technische Universiteit Delft)

Cover:
Two tulips, one faceted and one fully rendered, represent the concepts of discreteness and continuity. Their stems are interlaced and wrapped in a ribbon, forming a Möbius strip in reference to non-Abelian braiding and topology. Several key formulas accompany the lines of the painting.
By Yevheniia Cheipesh.

To my family

Contents

CHAPTER 1

Introduction

1.1. Preface

A fundamental concept in condensed matter physics is that the effective behavior of electrons is strongly influenced by the medium in which they exist. An example of this is graphene, in which electrons are effectively massless. The symmetry of its celebrated honeycomb lattice imposes a band structure with two gap closings at two points in the Brillouin zone (BZ) [1, 2] around which the dispersion relation is a *Dirac cone* (Fig. 1.1)

$$E^2 = v^2(p_x^2 + p_y^2). \tag{1.1}$$

These points are called *Dirac points* and the Hamiltonian describing the low energy excitations around each of them is respectively

$$H_\pm = -i\hbar v(\partial_x \sigma_x \pm \partial_y \sigma_y). \tag{1.2}$$

This Hamiltonian realises the Dirac equation for massless fermions with velocity v in 2D, where the sign choice fixes the chirality of the particles.[1] The presence of two species of massless Dirac fermions with opposite chirality is not an accident but a consequence of a fundamental fact about

---

[1] For massless particles chirality and helicity coincide.

lattice Hamiltonians. Nielsen and Ninomiya [3] proved, in the context of high energy physics, that the following statements about a lattice Hamiltonian cannot be simultaneously true:

- The Hamiltonian is local.
- The Hamiltonian preserves chiral symmetry.
- The sum of chiralities of the Dirac points in the Brillouin zone is not zero.

This no-go theorem seems to imply that we cannot have a crystal with a single species of massless fermions. However, nature often manages to find a way around our expectations, and 3D topological insulators (3DTIs) are an example of this. These materials have a gapped bulk but a gapless surface whose low energy dispersion relation consists of a *single Dirac cone*. Nature is showing us that we can have a single species of massless chiral fermions as long as they are embedded in a lattice of larger dimension.

Yet, this does not mean that in order to simulate the 2D surface modes of a 3DTI we need to spend resources representing the whole 3D lattice. The problem of building a lattice model with a single Dirac cone is commonly referred to as the *fermion doubling problem* and it is well known in the field of lattice gauge theories where there have been many ways of tackling it [4–7]. The main part of this thesis focuses on addressing this problem within the framework of topological condensed matter by developing the *tangent fermions* approach, a scheme pioneered by Stacey that breaks the locality assumption [8].

The present chapter is dedicated to laying out some fundamental concepts related to the fermion doubling problem, as well as showing how 3DTIs can be used to build chiral superconductors and introducing the concept of non-Abelian braiding.

1.2. Topological protection of the Dirac cone and no-go theorem in 2D

Since disorder is unavoidable in real materials, we would like it to be accurately featured by our discretization scheme. One crucial trait of massless fermions on the surface of topological materials is the gapless nature of the Dirac cone even when disorder is present. This robustness is referred to as *topological protection*, and it relies on the presence of either

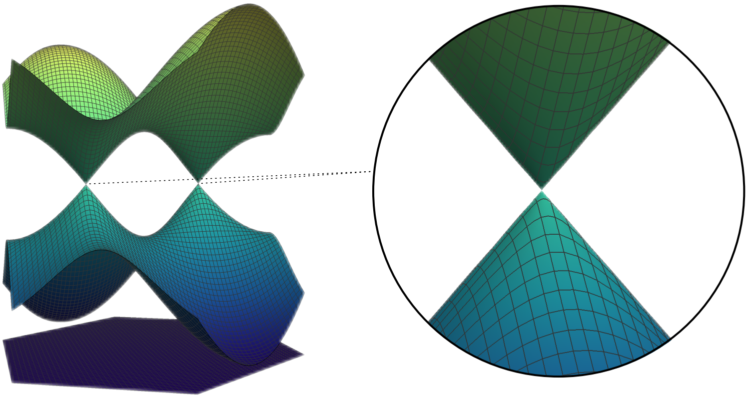

Figure 1.1: Band structure of graphene in the first Brillouin zone. Inset: Conical dispersion relation (Dirac cone) around the gap closings (Dirac points).

chiral or symplectic symmetries[2] but also on the Dirac cone to be the only one in the Brillouin zone.

In this section, we demonstrate how chiral and symplectic symmetries provide this topological protection for local Hamiltonians in 2D. By doing it, we also uncover the main obstacle to achieving it in a lattice model. Namely, that *a local discretization of the 2D Dirac Hamiltonian cannot have an unpaired Dirac cone, unless it breaks both chiral and symplectic symmetries.*

Chiral symmetry

A system has chiral symmetry if there exists a unitary and hermitian *chirality operator* Γ that anticommutes with the Hamiltonian. The conditions on Γ imply that it has two eigenspaces with eigenvalues ± 1 respectively and $\Gamma^2 = 1$. Also, the anticommutation with the Hamiltonian implies

$$\langle\psi_\pm| H |\phi_\pm\rangle = \langle\psi_\pm| \Gamma^2 H |\phi_\pm\rangle = -\langle\psi_\pm| \Gamma H \Gamma |\phi_\pm\rangle = -\langle\psi_\pm| H |\phi_\pm\rangle\,, \tag{1.3}$$

being $|\chi_+\rangle$ ($|\chi_-\rangle$) a state of positive (negative) chirality. So in the basis of eigenstates of Γ, the diagonal blocks of H are zero. We can then write

---

[2] Crystalline symmetries can also stabilize the Dirac point, in which case we talk about “fragile” topological protection [9].

our Hamiltonian by blocks as[3]

$$H(\boldsymbol{k}) = \begin{pmatrix} 0 & A^\dagger(\boldsymbol{k}) \\ A(\boldsymbol{k}) & 0 \end{pmatrix}. \tag{1.4}$$

Given a closed loop γ in the reciprocal space along which $\det A \neq 0$, we can define a *winding number* as

$$W = \frac{1}{2\pi} \operatorname{Im} \oint_\gamma \nabla_k \log\left(\det A(\boldsymbol{k})\right) \cdot d\boldsymbol{k}. \tag{1.5}$$

If the Hamiltonian is local, $A(\boldsymbol{k})$ is continuous and single valued. This implies that W must be integer and therefore we can use it as a topological invariant to classify Hamiltonians and loops. If there are no zeros of $\det A$ inside of γ, then the loop can be contracted to a point and $W = 0$.

From equation (1.2), it follows that at a Dirac point $\det A(\boldsymbol{k}_\mathrm{D})$ vanishes. This means that a loop containing a Dirac point cannot be contracted to a point. Indeed, calculating the winding number along such loop, one finds that it is equal to the chirality of the cone $W = \pm 1$. If we then continuously deform the Hamiltonian (always making sure that $\det A$ does not vanish on the loop), since W cannot change, the Dirac cone can only move around, but never gap out. Therefore, we say that the Dirac cone is topologically protected.

In general, the winding number of a loop is equal to the sum of the chiralities of the Dirac points that it encloses, so a loop surrounding two Dirac points with opposite chiralities has $W = 0$. In consequence, pairs of Dirac cones with opposite chiralities can gap each other out without changing W. This means that *only unpaired Dirac cones are protected.*

The winding number can also help us derive the no-go theorem in 2D. The winding number of the loop γ_e that goes along the edges of the Brillouin zone will be equal to the sum of the chiralities of all the Dirac cones in the Brillouin zone.[4] For this loop, the integral (1.5) can be separated into four integrals along each of the edges of the Brillouin zone. Due to the periodicity of $H(\boldsymbol{k})$, these integrals must cancel out by pairs, so the sum of the chiralities of the Dirac points in the BZ is always zero.

---

[3] In the most general case, A does not need to be a square matrix. In that case, there is always a set of states of fixed chirality pinned to zero energy, and the following discussion must be slightly adapted. Since this is not the case for the Dirac Hamiltonian, we will not get into these details.

[4] If there is a Dirac point on the edges of the Brillouin zone, we can always sligthly deform our path γ_e to avoid it while making sure that the whole BZ is contained in the loop and the argument still applies.

This proves that if the Hamiltonian is local and has chiral symmetry, it cannot have a single unpaired Dirac cone.

Symplectic symmetry

The time reversal symmetry of spinful systems is called symplectic symmetry. If it holds, Kramers theorem applies [10]. This theorem dictates that all eigenstates of the Hamiltonian must be doubly degenerate. Since time reversal maps $\boldsymbol{k} \to -\boldsymbol{k}$, a band crossing is necessary at time reversally invariant momenta (TRIMs) for any local Hamiltonian (namely, continuous in reciprocal space).[5] Therefore, a Dirac cone at a TRIM is protected by symplectic symmetry.

If both chiral and symplectic symmetries are maintained, the Brillouin zone contains a Dirac point at zero energy at each TRIM. There are 2^d such time-reversally invariant momenta in d dimensions, so 4 in 2D. If we then break symplectic symmetry we can move the Dirac points around and gap them out pairwise by merging two Dirac cones with opposite winding number. However, we can not end up with an unpaired Dirac cone unless we also break chiral symmetry, spoiling the topological protection.

In the next section, we review the most commonly used discretization methods for the Dirac Hamiltonian, and in 1.3.5 we introduce the tangent fermions approach which breaks the locality condition to find a work around: a nonlocal discretization can have discontinuities or poles in the dispersion relation, which may "hide" a Dirac point.

1.3. Methods to discretize the Dirac equation

We now turn to the overview of methods to discretize the 2D Dirac Hamiltonian,

$$H_0 = \hbar v(k_x\sigma_x + k_y\sigma_y) = \hbar v \begin{pmatrix} 0 & -i\partial_x - \partial_y \\ -i\partial_x + \partial_y & 0 \end{pmatrix}, \tag{1.6}$$

focusing on the case that the massless electrons can move freely on the x–y plane, without any electromagnetic fields. The Dirac fermions have energy independent velocity v. The Pauli spin matrices $\boldsymbol{\sigma}$ are coupled to the momentum $\boldsymbol{k} = -i\partial_{\boldsymbol{r}}$. In Eq. (1.6) the spin-momentum locking is such that the spin points parallel to the momentum. The alternative

---

[5] a point $\boldsymbol{k}_T$ of the Brillouin zone is at a TRIM if $2\boldsymbol{k}_T$ is a reciprocal lattice vector.

perpendicular spin-momentum locking ($k_x\sigma_y - k_y\sigma_x$) can be obtained by a unitary transformation of H_0, so we need not distinguish the two cases here.

The energy-momentum relation (dispersion relation) of the Dirac Hamiltonian,

$$E(\boldsymbol{k})^2 = (\hbar v)^2(k_x^2 + k_y^2), \tag{1.7}$$

consists of a pair of cones that touch at the point $\boldsymbol{k} = 0$ — the Dirac point. When the Hamiltonian is discretized on a lattice the dispersion relation becomes periodic: $E(\boldsymbol{k} + \boldsymbol{K}) = E(\boldsymbol{k})$ for any reciprocal lattice vector $\boldsymbol{K}$. Momenta which are not related by a reciprocal lattice vector form the Brillouin zone. For some discretization methods the Dirac point at $\boldsymbol{k} = 0$ is copied at other points in the Brillouin zone (fermion doubling).

The Dirac Hamiltonian (1.6) satisfies the two symmetry relations introduced in the previous section,

$$\begin{aligned} \text{chiral symmetry:}\;\; & \sigma_z H_0 \sigma_z = -H_0, \\ \text{symplectic symmetry:}\;\; & \sigma_y H_0^* \sigma_y = H_0. \end{aligned} \tag{1.8}$$

The complex conjugation is taken in the real-space basis, so the sign of both momentum and spin is inverted by the symplectic symmetry operation. For each discretization method we will check whether the symmetries (1.8) are preserved or not.

The topological protection of the Dirac point relies on the absence of fermion doubling and on the conservation of at least one of the two fundamental symmetries (1.8). The linearity of the dispersion relation, $E \propto |\boldsymbol{k}|$, may be a desirable feature, but it is not essential for the protection. What is essential for a practical method is that the eigenvalue problem can be solved using linear algebra of sparse matrices.

In Table 1.1 we summarize the properties of the various discretization schemes that we will discuss. Each discretization has its own dispersion relation, which reduces to the linear dispersion near the physical Dirac point at the center $\boldsymbol{k} = 0$ of the Brillouin zone. The distinguishing properties include:

- the symmetries that the discretization does or does not preserve — the chiral symmetry which defines the handedness of the particles and the symplectic symmetry which is the time-reversal symmetry for spin-1/2 particles;
- the number of Dirac points in the Brillouin zone (1 if there is no fermion doubling);

dispersion	chiral symm.	symplectic symm.	Dirac points	locality	top. prot.
sine	✓	✓	4	✓	×
sine+cosine ([11])	×	×	1	✓	×
staggered ([12])	✓	×	2	✓	×
linear sawtooth ([13])	✓	✓	1	×	×
tangent ([8])	✓	✓	1	×(✓)	✓

Table 1.1: Five approaches to discretize the Dirac equation on a 2D lattice. The presence or absence of a property is indicated by ✓ or ×, respectively. The tangent dispersion has a nonlocal Hamiltonian, but it allows a local formulation of a generalized eigenproblem (hence the ✓ in parentheses). Only the tangent dispersion has an unpaired and topologically protected Dirac point.

- the locality of the discretization, meaning whether the discretized Hamiltonian only couples nearby lattice points;
- and finally the presence or absence of the protection against gap opening by disorder.

1.3.1. Sine dispersion

We start with a square lattice, lattice constant a, and discretize the derivative operator by the first order finite difference:

$$\partial_x f(x,y) \mapsto (2a)^{-1}[f(x+a,y) - f(x-a,y)], \tag{1.9}$$

and similarly for $\partial_y f(x,y)$. Notice that $e^{a\partial_x} = e^{iak_x}$ is the translation operator, $e^{a\partial_x} f(x) = f(x+a)$. The discretization (1.9) therefore gives the Hamiltonian

$$H_{\text{sine}} = (\hbar v/a)(\sigma_x \sin ak_x + \sigma_y \sin ak_y), \tag{1.10}$$

with the sine dispersion

$$E_{\text{sine}}(\boldsymbol{k})^2 = (\hbar v/a)^2(\sin^2 ak_x + \sin^2 ak_y). \tag{1.11}$$

Chiral symmetry and symplectic symmetry (1.8) are both preserved by the Hamiltonian H_{sine}, but there is fermion doubling: In the Brillouin zone $|k_x| < \pi/a$, $|k_y| < \pi/a$ there are Dirac points at each of the time-reversally invariant momenta: the center $\boldsymbol{k} = 0$, the corners $|k_x| = |k_y| = \pi/a$

and the midpoints $k_x = 0, |k_y| = \pi/a$ and $k_y = 0, |k_x| = \pi/a$. The four corners and opposite midpoints are related by a linear combination of reciprocal lattice vectors $\boldsymbol{K} = (2\pi/a, 0)$ and $\boldsymbol{K}' = (0, 2\pi/a)$, so there are 4 inequivalent Dirac points in the Brillouin zone.

1.3.2. Sine plus cosine dispersion

An effective way to remove the spurious Dirac points is to gap them by the addition of a momentum dependent magnetization $\mu(\boldsymbol{k})\sigma_z$ to the Dirac Hamiltonian. If μ vanishes at $\boldsymbol{k} = 0$ the physical Dirac point at the center of the Brillouin zone is unaffected. This is the approach introduced by Wilson [11, 14]. A quadratic $\mu \propto k^2$ is discretized on a square lattice, resulting in the Hamiltonian

$$H_{\text{Wilson}} = (\hbar v/a)(\sigma_x \sin ak_x + \sigma_y \sin ak_y) + m_0\sigma_z(2 - \cos ak_x - \cos ak_y), \tag{1.12}$$

with the sine plus cosine dispersion

$$E_{\text{Wilson}}(\boldsymbol{k})^2 = (\hbar v/a)^2(\sin^2 ak_x + \sin^2 ak_y) + m_0^2(2 - \cos ak_x - \cos ak_y)^2. \tag{1.13}$$

The Dirac points of the sine dispersion acquire a gap $\propto m_0$, only the Dirac point at $\boldsymbol{k} = 0$ remains gapless.

Fermion doubling in Wilson's approach is avoided at expense of a breaking of both chiral and symplectic symmetries. The product of these two symmetries is preserved,

$$\sigma_x H^*_{\text{Wilson}}\sigma_x = -H_{\text{Wilson}}, \tag{1.14}$$

which is sufficient for some applications [15–18].

1.3.3. Staggered lattice dispersion

Much of the particle physics literature follows Susskind's approach [12, 19], which applies a different lattice to each of the two components of the spinor wave function $\Psi = (u, v)$. The two lattices are staggered, see Fig. 1.2, displaced by half a lattice constant. The momentum operator transfers from one lattice to the other, which amounts to a diagonal displacement by a distance of $a/\sqrt{2}$, as expressed by the translation operators $e^{ia(k_x \pm k_y)/2}$.

The discretized Dirac Hamiltonian still acts on the original lattice (black

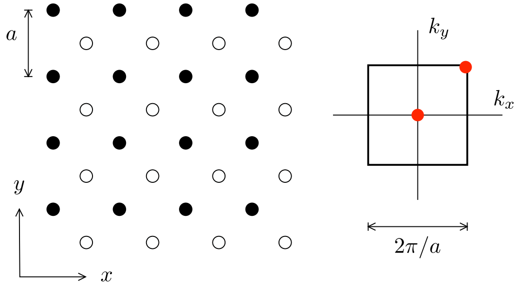

Figure 1.2: Left: Staggered pair of grids for the discretization of Dirac fermions in Susskind's approach. The black and white dots distinguish the u and v amplitudes of the spinor wave function $\Psi = (u, v)$. Right: The square shows the Brillouin zone in momentum space, the red dots indicate two inequivalent Dirac points.

dots in Fig. 3.1). The unitary transformation with operator

$$U_{\text{stagger}} = \begin{pmatrix} 1 & 0 \\ 0 & e^{ia(k_x+k_y)/2} \end{pmatrix} \tag{1.15}$$

initializes the pair of staggered lattices (u component on the black dots, v-component on the white dots). The Hamiltonian then takes the form

$$H_{\text{Susskind}} = \sqrt{2}\frac{\hbar v}{a} U^{\dagger}_{\text{stagg.}} \big(\sigma_x \sin[a(k_x-k_y)/2] + \sigma_y \sin[a(k_x+k_y)/2]\big) U_{\text{stagg.}}. \tag{1.16}$$

Check that the $2\pi/a$ periodicity in the k_x and k_y components is maintained: the minus sign picked up by the sine terms is canceled by the unitaries.

In terms of the rotated momenta $q_x = (k_x - k_y)/\sqrt{2}$, $q_y = (k_x + k_y)/\sqrt{2}$, normalized such that $|\boldsymbol{q}|^2 = |\boldsymbol{k}|^2$, one has

$$H_{\text{Susskind}} = \hbar v[q_x\sigma_x + q_y\sigma_y + \mathcal{O}(q^2)], \tag{1.17}$$

so the Dirac Hamiltonian (1.6) is recovered in the continuum limit.

The corresponding dispersion relation

$$E_{\text{Susskind}}(\boldsymbol{k})^2 = 2(\hbar v/a)^2\big(\sin^2[(k_x - k_y)/2] + \sin^2[(k_x + k_y)/2]\big) \tag{1.18}$$

has two inequivalent Dirac points in the Brillouin zone, at the center and at the corner. Compared to the sine discretization the staggered lattice has reduced the number of Dirac points from four to two, but fermion doubling has not been fully eliminated. Chiral symmetry is preserved, but symplectic symmetry is broken by the relative displacement of the two spinor components.

More generally, on a d-dimensional lattice the sine dispersion has 2^d inequivalent Dirac points in the Brillouin zone (one at each time-reversally invariant momentum), and the staggered lattice reduces that by one half. For $d = 1$ this is sufficient to avoid fermion doubling. In that case the Susskind Hamiltonian (1.16) is equivalent (up to a unitary transformation) to the 1D Wilson Hamiltonian

$$H_{\text{Wilson}}(k_x, k_y = 0) = (\hbar v/a)\sigma_x \sin ak_x + m_0\sigma_z(1 - \cos ak_x) \tag{1.19}$$

for the special value $m_0 = \hbar v/a$. The resulting $\sin(ak_x/2)$ dispersion is shown in Fig. 1.3 (green curve).

1.3.4. Linear sawtooth dispersion

The discretization schemes discussed in the previous subsection are all local, in the sense that they produce a sparse Hamiltonian: each lattice site is only coupled to a few neighbors. If one is willing to abandon the locality of the Hamiltonian, one can eliminate the fermion doubling by a discretization of the spatial derivative that involves all lattice points,

$$\begin{aligned}\partial_x f(x,y) \mapsto a^{-1}\sum_{n=1}^{\infty}(-1)^n n^{-1}[f(x-na,y) - f(x+na,y)]\\ = a^{-1}\sum_{n=1}^{\infty}(-1)^n n^{-1}(e^{-na\partial_x} - e^{na\partial_x})f(x,y) = a^{-1}(\ln e^{a\partial_x})f(x,y).\end{aligned} \tag{1.20}$$

This discretization scheme goes by the name of SLAC fermions [13, 20] in the particle physics literature. It has also been implemented in a condensed matter context [21–24].

In momentum representation, the Hamiltonian takes the form

$$H_{\text{SLAC}} = -i(\hbar v/a)\big(\sigma_x \ln e^{iak_x} + \sigma_y \ln e^{iak_y}\big), \tag{1.21}$$

where the branch cut of the logarithm is taken on the negative real axis. The corresponding dispersion

$$E_{\text{SLAC}}(\boldsymbol{k})^2 = (\hbar v)^2\,(k_x^2 + k_y^2)\ \text{ for }\ |k_x|, |k_y| < \pi/a, \tag{1.22}$$

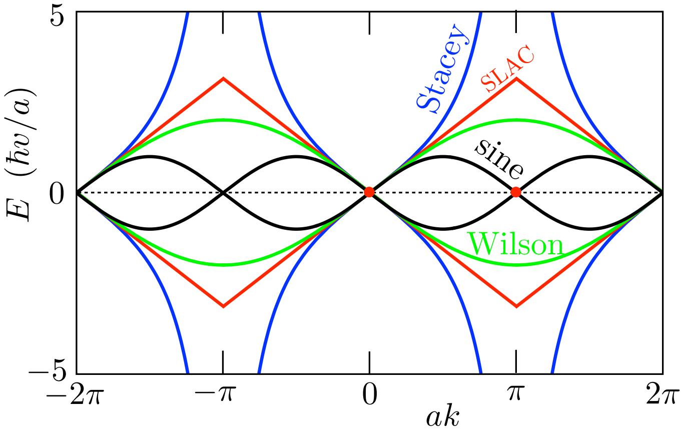

Figure 1.3: Dispersion relations of Dirac fermions on a 1D lattice, for four different discretization schemes. One with fermion doubling (black curve, E_{sine}) and three without fermion doubling: E_{Wilson} (green curve, for $m_0 = \hbar v/a$, when $E_{\text{Susskind}} = E_{\text{Wilson}}$), E_{SLAC} (red curve), and E_{Stacey} (blue curve). Inequivalent Dirac points are indicated by a red dot. The first Brillouin zone is the interval $|k| < \pi/a$, the plot is extended to $|k| < 2\pi/a$ to show the dispersion on both sides of the Brillouin zone boundary.

is a linear sawtooth, with a cusp at the edge of the Brillouin zone (see Fig. 1.3, red curve). Fermion doubling is avoided and both chiral and symplectic symmetries are preserved.

1.3.5. Tangent dispersion

The approach pioneered by Stacey [8, 25] seems a minor modification of the SLAC approach — but it has far reaching consequences. The nonlocal derivative (1.20) is modified by removal of the $1/n$ factor,

$$\begin{aligned}\partial_x f(x,y) &\mapsto 2a^{-1}\sum_{n=1}^{\infty}(-1)^n[f(x-na,y)-f(x+na,y)]\\ &= 2a^{-1}\sum_{n}(-1)^n(e^{-na\partial_x}-e^{na\partial_x})f(x,y)\\ &= -(2i/a)\tan(ia\partial_x/2)f(x,y).\end{aligned}\tag{1.23}$$

The corresponding Hamiltonian

$$H_{\rm Stacey}=(2\hbar v/a)\bigl[\sigma_x\,\tan(ak_x/2)+\sigma_y\tan(ak_y/2)\bigr],\tag{1.24}$$

has a tangent dispersion,

$$E_{\rm Stacey}(\boldsymbol{k})^2=(2\hbar v/a)^2\left[\tan^2(ak_x/2)+\tan^2(ak_y/2)\right].\tag{1.25}$$

The cusp at the Brillouin zone boundary has been replaced by a pole (see Fig. 1.3, blue curve).

As in the SLAC approach, the Stacey approach avoids fermion doubling while preserving chiral and symplectic symmetries, at the expense of a nonlocal Hamiltonian. The key merit of the tangent dispersion is that the nonlocality can be removed by transforming the eigenproblem $H\Psi=E\Psi$ into a generalized eigenproblem $\mathcal{H}\Psi=E\mathcal{P}\Psi$, with local operators $\mathcal{H}$ and $\mathcal{P}$ on both sides of the equation. This transformation is possible because the tangent is the ratio of two operators, sine and cosine, that have a local representation on the lattice.

Ref. [8] formulated the generalized eigenproblem by means of finite differences on a pair of staggered grids. This produces operators $\mathcal{H}$ and $\mathcal{P}$ that are local but not Hermitian, which is problematic in a numerical implementation. The alternative formulation of Ref. [26] resolves this issue, resulting in the generalized eigenproblem

$$\begin{aligned}&\mathcal{H}\Psi=E\mathcal{P}\Psi,\;\;\mathcal{P}=\tfrac{1}{4}(1+\cos ak_x)(1+\cos ak_y),\\&\mathcal{H}=\frac{\hbar v}{2a}\bigl[\sigma_x(1+\cos ak_y)\sin ak_x+\sigma_y(1+\cos ak_x)\sin ak_y\bigr].\end{aligned}\tag{1.26}$$

Both operators $\mathcal{H}$ and $\mathcal{P}$ are Hermitian and $\mathcal{P}$ is also positive definite.[6] Both are sparse matrices, only nearby sites on the lattice are coupled. This combination of properties allows for an efficient calculation of the energy spectrum. In order to do this in practice, it is essential to formulate this problem in real space.

---

[6] To avoid the complications from a noninvertible $\mathcal{P}$, one can choose a lattice with periodic boundary conditions over an odd number of sites; then all eigenvalues of $\mathcal{P}$ are strictly positive.

Real-space formulation of the generalized eigenproblem.

The generalized eigenproblem (1.26) of tangent fermions can be formulated in the position basis upon the substitution

$$e^{iak_\alpha} \mapsto \sum_{\boldsymbol{n}} |\boldsymbol{n}\rangle\langle \boldsymbol{n}+\boldsymbol{e}_\alpha|. \tag{1.27}$$

The sum over $\boldsymbol{n} = n_x\boldsymbol{e}_x + n_y\boldsymbol{e}_y$, with $n_x, n_y \in \mathbb{Z}$, is a sum over lattice sites on the 2D square lattice (lattice constant a).

We thus have the equation $\mathcal{H}\Psi = E\mathcal{P}\Psi$, with on the left-hand-side the operator

$$\mathcal{H} = -\frac{i\hbar v}{a}\boldsymbol{D}\cdot\boldsymbol{\sigma},\quad \boldsymbol{D} = (D_x, D_y), \tag{1.28a}$$

$$D_x = \tfrac{1}{8}\sum_{\boldsymbol{n}}\Big(2|\boldsymbol{n}\rangle\langle\boldsymbol{n}+\boldsymbol{e}_x| + |\boldsymbol{n}\rangle\langle\boldsymbol{n}+\boldsymbol{e}_x+\boldsymbol{e}_y| + |\boldsymbol{n}\rangle\langle\boldsymbol{n}+\boldsymbol{e}_x-\boldsymbol{e}_y|\Big) - \text{H.c.}, \tag{1.28b}$$

$$D_y = \tfrac{1}{8}\sum_{\boldsymbol{n}}\Big(2|\boldsymbol{n}\rangle\langle\boldsymbol{n}+\boldsymbol{e}_y| + |\boldsymbol{n}\rangle\langle\boldsymbol{n}+\boldsymbol{e}_x+\boldsymbol{e}_y| + |\boldsymbol{n}\rangle\langle\boldsymbol{n}+\boldsymbol{e}_y-\boldsymbol{e}_x|\Big) - \text{H.c.}, \tag{1.28c}$$

and on the right-hand-side the operator $\mathcal{P} = \Phi^\dagger\Phi$ with

$$\Phi = \tfrac{1}{4}\sum_{\boldsymbol{n}}\Big(|\boldsymbol{n}\rangle\langle\boldsymbol{n}| + |\boldsymbol{n}\rangle\langle\boldsymbol{n}+\boldsymbol{e}_x| + |\boldsymbol{n}\rangle\langle\boldsymbol{n}+\boldsymbol{e}_y| + |\boldsymbol{n}\rangle\langle\boldsymbol{n}+\boldsymbol{e}_x+\boldsymbol{e}_y|\Big). \tag{1.29}$$

The abbreviation H.c. stands for "Hermitian conjugate". Both operators $\mathcal{H}$ and $\mathcal{P}$ are local, only nearby lattice points are connected.

By way of illustration, we work out the expectation value

$$\langle\psi|\Phi^\dagger\Phi|\psi\rangle = \sum_{\boldsymbol{n}}|\tilde{\psi}_{\boldsymbol{n}}|^2,\quad \tilde{\psi}_{\boldsymbol{n}} = \tfrac{1}{4}(\psi_{\boldsymbol{n}}+\psi_{\boldsymbol{n}+\boldsymbol{e}_x}+\psi_{\boldsymbol{n}+\boldsymbol{e}_y}+\psi_{\boldsymbol{n}+\boldsymbol{e}_x+\boldsymbol{e}_y}). \tag{1.30}$$

One can interpret this in terms of the two staggered lattices shown in Fig. 1.4. The field $\tilde{\psi} = \Phi\psi$ is defined on a white lattice point as the average of the amplitudes of the wave function ψ on the four adjacent black lattice points.

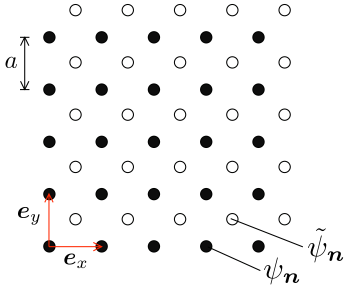

Figure 1.4: Staggered pair of grids to represent the two fields ψ and $\tilde{\psi} = \Phi\psi$. *Figure from Ref. [26].* CC BY 4.0 license

1.4. Chiral superconductors

As shown by Fu and Kane, a 3DTI can be used to engineer a chiral superconductor [27] by proximitizing it with an s-wave superconductor. The Bogoliubov-de Gennes Hamiltonian corresponding to such system is

$$H = \begin{pmatrix} \hbar v \boldsymbol{k} \cdot \boldsymbol{\sigma} - \mu & \Delta^* \\ \Delta & -\hbar v \boldsymbol{k} \cdot \boldsymbol{\sigma} + \mu \end{pmatrix} . \tag{1.31}$$

The unitary transformation given by

$$U = \begin{pmatrix} \exp\big(-i\frac{\pi}{4}(\sin\theta_k \sigma_x - \cos\theta_k \sigma_y)\big) & 0 \\ 0 & \exp\big(i\frac{\pi}{4}(\sin\theta_k \sigma_x - \cos\theta_k \sigma_y)\big) \end{pmatrix} , \tag{1.32}$$

being θ_k the polar angle of $\boldsymbol{k}$, transforms our Hamiltonian into

$$UHU^\dagger = \begin{pmatrix} \hbar v|\boldsymbol{k}| - \mu & 0 & 0 & \Delta^* e^{-i\theta_k} \\ 0 & -\hbar v|\boldsymbol{k}| - \mu & -\Delta^* e^{i\theta_k} & \\ 0 & -\Delta e^{-i\theta_k} & \hbar v|\boldsymbol{k}| + \mu & 0 \\ \Delta e^{i\theta_k} & 0 & 0 & -\hbar v|\boldsymbol{k}| + \mu \end{pmatrix} . \tag{1.33}$$

For $\mu \gg |\Delta|$, the low energy spectrum is given by the first and fourth blocks, so we can project on them to obtain

$$H_C = \begin{pmatrix} \hbar v|\boldsymbol{k}| - \mu & \Delta^* e^{-i\theta_k} \\ \Delta e^{i\theta_k} & -\hbar v|\boldsymbol{k}| + \mu \end{pmatrix} . \tag{1.34}$$

Since the superconducting phase along the normal Fermi surface winds once, this effective Hamiltonian realises a chiral superconductor. These

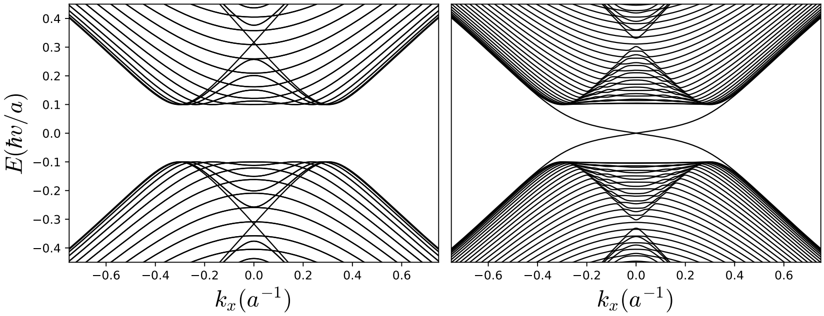

Figure 1.5: Low energy band structure in x direction of a tight-binding version of the Hamiltonian 1.31 for a periodic system in y direction (left) and a finite system with magnetic boundaries (right). In the finite system, we can appreciate two gapless edge modes with opposite velocity. The boundaries also lift the degeneracy of the bulk bands.

systems are topological [28], and they can host chiral edge modes. This is only possible if time reversal symmetry is broken. Since Hamiltonian 1.31 does not break it, the boundaries must. This is achieved by a magnetization term in z direction. The corresponding band structure is shown in Fig. 1.5.

In [29], they used this realisation of a chiral superconductor to observe the gap closing caused by a net superconducting current [30]. This happens due to the Doppler shift δE of the bands $\varepsilon(\boldsymbol{p})$ caused by the Cooper pair momentum $\boldsymbol{p}_s$ [31],

$$\delta E(\boldsymbol{p}) = \boldsymbol{p}_s \cdot \frac{\partial \varepsilon(\boldsymbol{p})}{\partial \boldsymbol{p}}. \tag{1.35}$$

In chapter 5, we study the effect of a net supercurrent on the chiral edge modes of such system.

1.5. Non-abelian anyons and braiding

A fundamental property that distinguishes fermions from bosons is their *exchange statistics*. This term refers to how the state of a system transforms when two particles are exchanged. We can express it as

$$|\Psi_{21}\rangle = U\,|\Psi_{21}\rangle\,. \tag{1.36}$$

For fermions the wavefunction changes sign, $U = -1$, while for bosons it stays the same, $U = 1$. A detail that is often overlooked in this regard is the fact that we can mean two different things by "particle exchange" [32]. On one hand, we can switch the quantum numbers of two particles. The statistics of fermions under this notion of exchange is responsible for the Pauli exclusion principle.

On the other hand, we can think of exchanging two particles by adiabatically driving them to each other's position without encountering each other along the way. In 3D, the Berry phase associated to such an exchange can only take the values ± 1, corresponding to bosons and fermions respectively. However, in 2D there can exist particles that acquire any phase.[7] We call this particles anyons, and for them $U = e^{i\theta}$.

If the ground state of a 2D system with two particles is degenerate, there is still a more general scenario. In such case, it is possible for the exchange to produce a linearly independent state. Particles with this behavior are called non-Abelian anyons and their exchange is described by a unitary transformation U rather than just a phase.

Kitaev managed to show how this property can be exploited to build a fault-tolerant quantum computer [33]. The idea is to encode a set of qubits in the ground state of a system of non-Abelian quasiparticles and use exchange operations to implement quantum gates on them. The world lines of the quasiparticles during this process interlace each other, and every possible braid results in a specific unitary transformation, hence the term *non-abelian braiding*. These systems store information non-locally and this makes the process immune to decoherence.

The first physical systems found to host non-Abelian anyons were fractional quantum Hall states at some specific filling factors (e.g. $\nu = 5/2$) [34, 35], but recently more attention has been given to topological superconductors like the ones described in the previous section. A $\varphi = h/2e$ magnetic flux tube threading a 2D topological superconductor creates an Abrikosov vortex in the superconducting pairing that binds a zero energy state. This state is called Majorana zero mode (MZM) because it is its own particle-hole partner.

A qubit can be encoded in the parity of two MZMs, i.e. in the filling of the fermionic degree of freedom that is split between them. Since the total parity of a superconductor is fixed, the minimal example of braiding with MZMs requires two pairs of these quasiparticles. Braiding one MZM from the first pair around another from the other pair induces a transfer

---

[7] The reason behind this difference comes down to the fact that in the 2D space, a loop around the origin cannot be contracted to a point without crossing it, while in 3D this can be done by lifting up the loop in the third dimension.

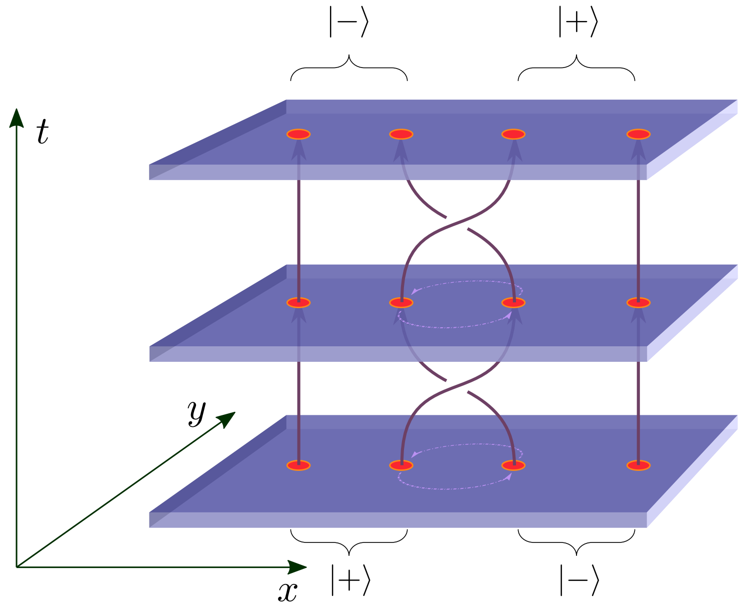

Figure 1.6: Schematics of the implementation of a σ_x gate on the state $\psi_{\text{in}} = |+\rangle\,|-\rangle$ to turn it into $\psi_{\text{out}} = |-\rangle\,|+\rangle$.

of a fermion between the pairs. This transformation corresponds to a σ_x gate (see [36]). A measurement of the state can be carried out by fusing a pair and measuring the corresponding parity.

A big obstacle stands in the way of implementing this protocol in practice, namely the fact that adiabatically moving around individual Abrikosov vortices is beyond our current technical capabilities. Fortunately, another kind of non-Abelian quasiparticles that can exist on the chiral edges of topological superconductors provides us with a solution. We are not referring to the ordinary edge Majorana fermions, which are Bogoliubov excitations with fermionic statistics, but to a special kind of many-body excitation called *edge-vortex*. They consist of a π-phase kink on the Majorana edge ground state, which is stable due to the reality condition of Majorana wavefunctions [37]. These excitations have non-Abelian statistics and they propagate along the edge of the superconductor at the edge mode velocity.

In chapter 6, we demonstrate a protocol to inject, braid and fuse edge vortices proposed by Beenakker *et al.* [38]. Although we model the process with a proximitised Chern insulator, a proximitised 3DTI surface surrounded by magnetic regions with opposite magnetizations would realise the same low energy phenomenology.

1.6. This thesis

Although the overarching theme of this thesis falls within the topic of lattice massless fermions, two distinct parts can be established. Chapters 2, 3 and 4 are devoted to developing various aspects of the *tangent fermions* discretization method, such as the implementation of time evolution or the inclusion of a magnetic field in a gauge invariant way. In contrast, chapters 5 and 6 study specific phenomena associated to chiral superconductors, using both analytical and numerical methods.

Chapter 2

As discussed in section 1.2, symmetries are crucial for the topological protection of a single Dirac cone. However, they will only provide such protection if the Hamiltonian is continuous in the whole reciprocal space, including across the edges of the Brillouin zone. This is often overlooked in many discretization methods.

In this chapter, we introduce a way to solve the time-dependent Dirac equation for massless fermions on a lattice that is discrete not only in space but also in time. The resulting evolution operator has unique properties. It preserves chiral and symplectic symmetries, it avoids fermion doubling and, remarkably, it is continuous across the edge of the energy-momentum Brillouin zone. We explicitly show how other methods fail to keep the gaplessness of the Dirac cone while in ours it is robust against any chiral or symplectic symmetry preserving perturbations. Since our dispersion relation reads $\tan^2(\varepsilon/2) = \tan^2(k_x/2) + \tan^2(k_y/2)$, we refer to our approach as the method of *tangent fermions*.

Chapter 3

Apart from the robustness of the Dirac cone, another well known property of massless fermions is a phenomenon known as “Klein tunneling”. It consists on the impossibility of backscattering of electrons that encounter a potential step perpendicular to their direction of motion, irrespective of the size of the barrier. This happens because such backscattering would

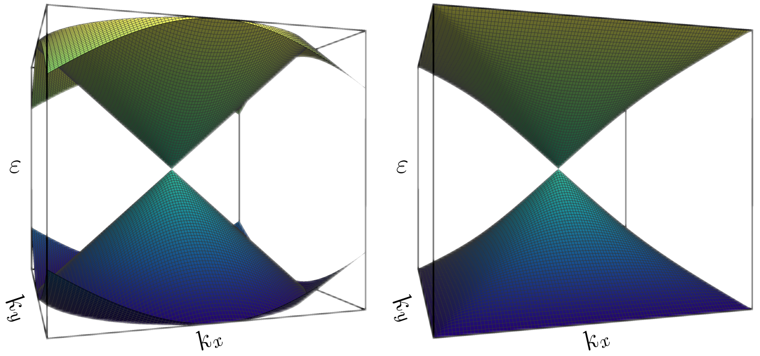

Figure 1.7: Band structure for SLAC (left) and tangent fermions (right). The bands are discontinuous accross the edge of the Brillouin zone only in the former.

require a spin switch, which is forbidden in chiral symmetry preserving systems.

However, this phenomenon may be spoiled by fermion doubling because of scattering to another Dirac cones in the Brillouin zone. To avoid this, a staggered space-time lattice discretization has been developed in the literature, with *one* single Dirac cone in the Brillouin zone of the original square lattice. In this chapter we show that the staggering doubles the size of the Brillouin zone, which actually contains *two* Dirac cones. We find that this fermion doubling causes a spurious breakdown of Klein tunneling, which can be avoided by the alternative single-cone discretization scheme introduced in chapter 2.

Chapter 4

The presence of a magnetic field B in a system of fermions induces Landau quantization, a phenomenon consisting on the emergence of separate flat energy bands known as Landau levels. While this happens for both massive and massless fermions, in the latter case the spectrum contains a particular Landau level at zero energy that is absent in the former. This "zeroth Landau level" is special because it has a well defined chirality, which makes its flatness robust against chirality preserving disorder.

However, a lattice discretization with fermion doubling or chiral symmetry breaking can spoil this protection, inducing a broadening of the zeroth Landau level when B has spatial fluctuations. In this chapter, we

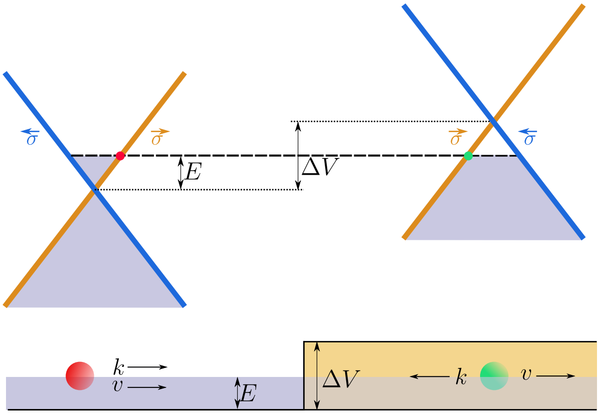

Figure 1.8: Klein tunneling. The incoming electron (red) can only be transmitted, switching its momentum and keeping its spin and velocity (green).

extend the tangent fermions approach to allow for the incorporation of magnetic fields and show how this can be used to obtain robust zeroth Landau levels.

Chapter 5

The right panel of Fig. 1.5 shows the band structure of a spinful chiral superconductor –more specifically, a Fu-Kane heterostructure– for zero supercurrent. In this chapter we explore the effect a non-zero net supercurrent parallel to the edges of such system and find out that something special happens at a critical value of the Cooper pair momentum $\Delta_0^2/\mu v_{\mathrm{F}}$. At this point, the velocity of one of the Majorana edge modes switches sign –we call this a *chirality inversion*–, a process that is accompanied by the emergence of two new states at the Fermi energy.

This chirality inversion leaves traces in the transport properties of the system. Firstly, the heat conductance is doubled because now there are twice as many modes that can transport energy. Secondly, the newly generated modes have non-zero charge, so electrical current can now be transported, and therefore the system acquires a non-zero electrical conductance. We also show that the chirality inversion is a unique signature of Majorana fermions in a spinful topological superconductor: it does not exist for spinless chiral p-wave pairing.

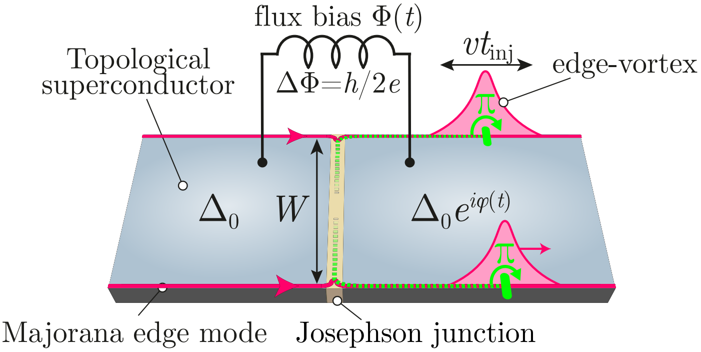

Figure 1.9: Edge vortex injector of [38].

Chapter 6

As introduced in section 1.5, the chiral edge modes of a topological supercondutor can carry non-Abelian excitations. These so-called edge-vortices are a π-phase "twist" of the wavefunctions of the edge Bogoliubov quasiparticles below the Fermi energy. These many-body excitations are made up of chiral edge modes which propagate along the edge of the system at the same velocity. Therefore, edge-vortices themselves must do the same.

In [38], Beenakker *et al.* proposed that such edge-vortices can be injected on the edges of a topological superconductor by splitting it with a Josephson junction and applying an $h/2e$ flux bias over it. In this chapter, we demonstrate it by dynamically simulating the process using a lattice model. Essentially, this amounts to numerically solving the time-dependent Schrödinger equation for the ground state of the superconducting device.

We show how the braiding of edge-vortices with bulk vortices results in a parity switch analogous to the one represented in Fig. 1.6. We also confirm the prediction made in [38] that the braiding process can be detected electrically. More crucially, our approach allows us to account for the dynamics of the junction and go beyond exisiting analytic descriptions that rely on the adiabatic approximation. Our study also reveals that if the flux bias is implemented too fast, residual excitations can remain trapped in the Josephson junction, spoiling the parity switch.

CHAPTER 2

Massless Dirac fermions on a space-time lattice with a topologically protected Dirac cone

2.1. Introduction

2.1.1. Objective

A three-dimensional (3D) topological insulator has gapless surface states with a conical dispersion [39, 40]. This Dirac cone is protected by Kramers degeneracy, no perturbation that preserves time-reversal symmetry can gap it out — provided that the top and bottom surfaces remain uncoupled, to prevent Dirac cones from annihilating pairwise [41].

To study the dynamics of Dirac fermions on a computer, one needs to discretize the Dirac equation

$$i\hbar\left(\frac{\partial}{\partial t}+v\,\boldsymbol{\sigma}\cdot\frac{\partial}{\partial \boldsymbol{r}}\right)\Psi(\boldsymbol{r},t)=V(\boldsymbol{r})\Psi(\boldsymbol{r},t) \tag{2.1}$$

for the two-component spinor $\Psi(\boldsymbol{r},t)$ (with velocity v and Pauli spin matrices σ_α). The electrostatic potential V preserves time-reversal symmetry, so one would expect the Dirac cone to remain gapless for any time-reversally invariant discretization scheme that avoids fermion doubling [3] (only zero-energy states at momentum $\boldsymbol{k}=0$).

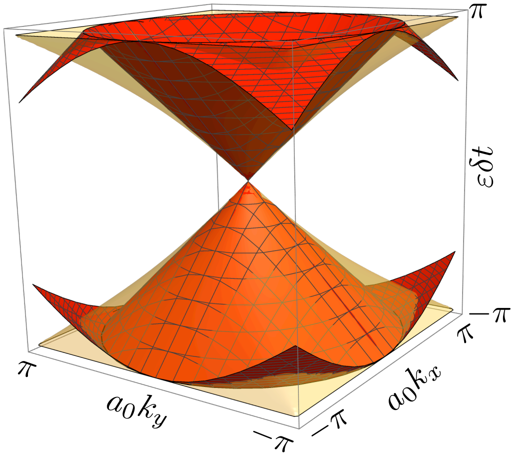

Figure 2.1: Quasi-energy bandstructure $\varepsilon(k_x, k_y)$ for the linear sawtooth dispersion (red) and for the tangent dispersion (yellow). The surfaces are computed, respectively, from the two equations $(\varepsilon\delta t + 2\pi n)^2 = (a_0 k_x)^2 + (a_0 k_y)^2$, $n \in \mathbb{Z}$, and $\tan^2(\varepsilon\delta t/2) = \tan^2(a_0 k_x/2) + \tan^2(a_0 k_y/2)$. Only the first Brillouin zone is shown, the full bandstructure is periodic in momentum k_α with period $2\pi/a_0$ and periodic in quasi-energy ε with period $2\pi/\delta t$. Near $\boldsymbol{k} = 0$ both discretizations have the Dirac cone $\varepsilon^2 = v^2(k_x^2 + k_y^2)$ of the continuum limit, with velocity $v = a_0/\delta t$. A potential that varies rapidly on the scale of the lattice constant can gap out the Dirac cone for the linear sawtooth dispersion, but not for the tangent dispersion.

The objective of this chapter is, firstly, to demonstrate that this expectation is incorrect, it does not apply to the split-operator technique [42] for the discretization of the time-evolution operator, which is commonly used [43–45] because of its computational efficiency. Then, secondly, we will show how a "drop-in" modification of the algorithm can restore a gapless Dirac cone — without reducing the computational efficiency (scaling as $N \ln N$ in the number of lattice sites).

We consider a 2+1-dimensional space-time lattice with lattice constants a_0 in space and δt in time. In the split-operator technique the derivative operator d/dx is evaluated in momentum representation as the linear function k in the first Brillouin zone $|k| < \pi/a_0$ — periodically repeated as a sawtooth for larger momenta. The drop-in modification that we propose is to replace k by $(2/a_0)\tan(a_0 k/2)$. The computational efficiency of the algorithm is not compromised, but the effect on the quasi-energy–momentum band structure is crucially important: While the linear sawtooth disper-

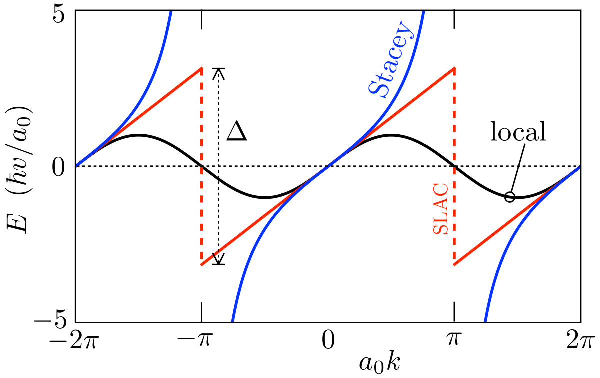

Figure 2.2: Three 1D dispersion relations, corresponding to a local discretization of the derivative operator d/dx (black curve) and to two alternative nonlocal discretizations (red and blue curves).

sion introduces discontinuous derivatives at Brillouin zone boundaries, the tangent dispersion produces a smooth band structure, see Fig. 2.1. As we will show, a potential that varies rapidly on the scale of a_0 is able to gap out the Dirac cone in the former case but not in the latter case.

By way of introduction, before we embark on the space-time discretization, we first discuss the simpler time-independent problem, when only space is discretized.

2.1.2. Time-independent problem

Consider a one-dimensional (1D) lattice along the x-axis, and first take $V \equiv 0$. Different ways to discretize the derivative d/dx will produce different energy-momentum dispersion relations $\pm E(k)$. (The ± sign distinguishes the chirality of the massless Dirac fermions, left-movers versus right-movers.) What all dispersions have in common is that they are periodic with period $2\pi/a_0$ and vanish linearly at $k = 0$. We compare three alternatives, see Fig. 2.2.

The local discretization $df/dx \mapsto [f(x + a_0) - f(x - a_0)]/(2a_0)$ gives a sine dispersion

$$E_{\text{local}}(k) = \frac{\hbar v}{a_0} \sin(a_0 k), \tag{2.2}$$

which vanishes also at the boundary $|k| = \pi/a_0$ of the first Brillouin zone (fermion doubling). A nonlocal discretization, which couples $f(x)$ to distant lattice points, can remove the spurious Dirac cone at nonzero momentum. The socalled "SLAC discretization" [13, 20] produces a dispersion relation that is strictly linear within the first Brillouin zone $|k| < \pi/a_0$. The dispersion has the 2π-periodic sawtooth form[1]

$$E_{\text{SLAC}}(k) = \frac{\hbar v}{a_0} \operatorname{mod}(a_0 k, 2\pi, -\pi). \tag{2.3}$$

Now apply the staggered potential $V(x) = V\cos(\pi x/a_0)$, switching from $+V$ to $-V$ between even and odd-numbered lattice sites. This potential couples the states at k and $k + \pi/a_0$, as described by the Hamiltonian

$$H_V(k) = \begin{pmatrix} E(k) & V/2 \\ V/2 & E(k+\pi/a_0) \end{pmatrix}. \tag{2.4}$$

The Brillouin zone is halved to $|k| < \pi/2a_0$, with the band structure

$$E_V(k) = \tfrac{1}{2}E(k) + \tfrac{1}{2}E(k+\pi/a_0) \pm \tfrac{1}{2}\sqrt{V^2 + [E(k) - E(k+\pi/a_0)]^2}. \tag{2.5}$$

A gap opens in the Dirac cone for both the local and SLAC discretizations, of size

$$\delta E_{\text{local}} = V, \quad \delta E_{\text{SLAC}} = \frac{V^2 a_0}{2\pi\hbar v} + \mathcal{O}(V^4). \tag{2.6}$$

What we learn from this simple calculation is that removing the second cone at $|k| = \pi/a_0$ is not enough to protect the Dirac cone at $k = 0$ from becoming gapped if the potential varies rapidly on the scale of the lattice constant. What happens is that the large gap Δ in the dispersion at $k = \pi/a_0$ is folded onto $k = 0$ by the staggered potential, resulting in a minigap $\delta E = V^2/\Delta$ for $V \ll \Delta$. To avoid the gap opening we thus need a pole $\Delta \to \infty$ in the dispersion at the Brillouin zone boundary.

An alternative discretization due to Stacey [8] gives the dispersion

$$E(k) = (2\hbar v/a_0)\tan(a_0 k/2), \tag{2.7}$$

with a pole at $k = \pi/a_0$. And indeed, substitution of Eq. (2.7) into Eq. (2.5) shows that no gap opens at $k = 0$ (see Fig. 2.3).

---

[1] The function $\operatorname{mod}(q, 2\pi, -\pi) \equiv q - 2\pi \left\lfloor \frac{q+\pi}{2\pi} \right\rfloor \in [-\pi, \pi)$ gives q modulo 2π with an offset $-\pi$. (The floor function $\lfloor x \rfloor$ returns the greatest integer $\leq x$.) The mod function is discontinuous at $q = \pi$, jumping from $-\pi$ to π, we arbitrarily assign to $\operatorname{mod}(\pi, 2\pi, -\pi)$ the value of $-\pi$. The choice $\operatorname{mod}(\pi, 2\pi, -\pi) \equiv 0$ would produce in Fig. 2.3 an isolated doubly degenerate state at $E = 0 = k$, disconnected from the SLAC bands.

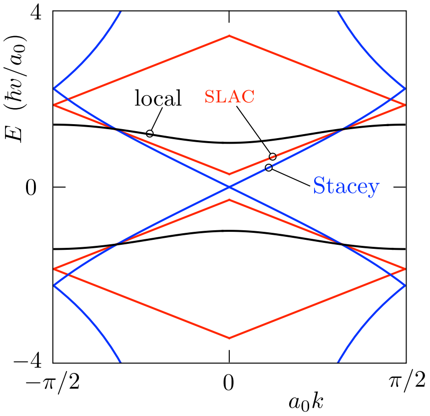

Figure 2.3: Band structure for three different spatial discretizations of the 1D Dirac Hamiltonian, with a staggered potential equal to $\pm 2\hbar v/a_0$ on even and odd-numbered lattice sites. The curves are computed from Eq. (2.5), with $E(k)$ given by Eqs. (2.2), (2.3), and (2.7) for the three discretizations. A gap opens at $k = 0$ for the local discretization and for the SLAC discretization, but not for the Stacey discretization.

The merits of the Stacey discretization for the time-independent problem were studied in Refs. [46] (at the level of the scattering matrix) and in Ref. [26] (at the level of the Hamiltonian). It was shown that the eigenvalue equation $H\Psi = E\Psi$ can be discretized into a *generalized* eigenvalue problem $\mathcal{H}\Psi = E\mathcal{P}\Psi$ with *local* Hermitian tight-binding operators on both sides of the equation.[2] Basically, a local formulation of the generalized eigenvalue problem is possible because tangent is the ratio of sine and cosine, which represent local tight-binding operators on a lattice. If all one would care about would be the presence of a pole in the dispersion at $k = \pi/a_0$, one could work with other functions than the tangent, but the tangent dispersion combines this property with the possibility of a local algorithm.

---

[2] The Stacey discretization is local in the sense that the operators $\mathcal{H}$ and $\mathcal{P}$ in the generalized eigenvalue problem $\mathcal{H}\Psi = E\mathcal{P}\Psi$ can be represented by *sparse* Hermitian matrices. If we would write this as a strict (non-generalized) eigenvalue problem, $\mathcal{P}^{-1}\mathcal{H}\Psi = E\Psi$, we would find that the operator $\mathcal{P}^{-1}\mathcal{H}$ is nonlocal (it is not sparse). There is therefore no violation of the Nielsen-Ninomiya no-go theorem [3], which only applies to strict eigenvalue problems.

2.1.3. Outline

So much for the introduction to the time-independent discretization. In what follows we turn to the dynamical problem, by generalizing the approach of Refs. [8, 26, 46] to the discretization of space and time. In the next section 2.2 we show that the time discretization removes the pole in the tangent dispersion, which becomes a smooth function of momentum $\boldsymbol{k}$ and quasi-energy ε (yellow bands in Fig. 2.1). In Sec. 2.3 we then prove that the Dirac point remains gapless for any perturbation that preserves either time-reversal symmetry or chiral symmetry — even if it varies rapidly on the scale of the lattice constant.

In contrast, the quasi-energy bandstructure of the linear sawtooth dispersion has discontinuous derivatives at the Brillouin zone boundaries (red bands in Fig. 2.1). These spoil the protection of the Dirac cone, which is gapped by a staggered potential.

A key feature of the approach presented in Sec. 2.2 is that it requires only a small modification of the usual split-operator technique, involving the replacement of the linear momentum operator appearing in the time-evolution operator by its tangent. Since this operator is evaluated in momentum representation, the replacement is immediate. It does not degrade the computational efficiency of the algorithm, which retains the favorable $N \ln N$ scaling in the number of lattice sites (limited only by the efficiency of the fast Fourier transform).

An alternative implementation which is fully in real space is possible, taking the form of an implicit finite-difference equation $A\Psi(t+\delta t) = B\Psi(t)$ with sparse matrices A and B. This formulation is a bit more cumbersome to explain, we present it an appendix.

2.2. Space-time discretization without zone boundary discontinuities

2.2.1. Split-operator technique

The Dirac Hamiltonian

$$\mathcal{H} = v\boldsymbol{k}\cdot\boldsymbol{\sigma} + V(\boldsymbol{r}) \tag{2.8}$$

is the sum of a kinetic term that depends on momentum $\boldsymbol{k}$ and a potential term that depends on position $\boldsymbol{r}$. (We set $\hbar$ to unity.) The split-operator

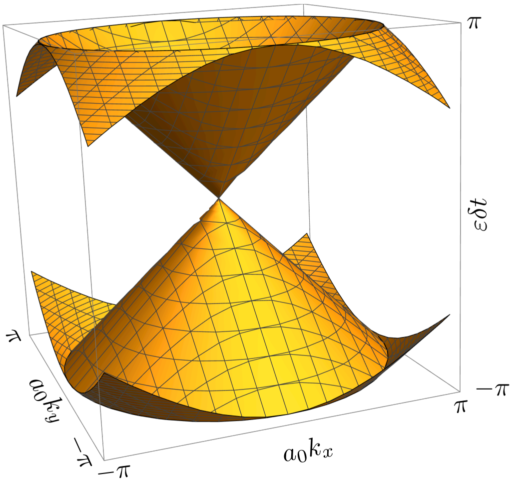

Figure 2.4: Momentum dependence of the quasi-energy for the free evolution operator U, given by Eq. (2.9) with $V = 0$, computed from Eq. (2.11) in the 2+1 dimensional case. The space and time discretization units are related by $a_0 = v\delta t$. Only the first Brillouin zone (2.12) is shown.

technique [42] separates these two terms in the time-evolution operator,

$$\begin{aligned}&\Psi(t+\delta t) = e^{-i\mathcal{H}\delta t}\Psi(t), \quad e^{-i\mathcal{H}\delta t} = U + \mathcal{O}(\delta t)^3,\\ &U = e^{-iV(\boldsymbol{r})\delta t/2}e^{-iv\delta t\,\boldsymbol{k}\cdot\boldsymbol{\sigma}}e^{-iV(\boldsymbol{r})\delta t/2},\end{aligned} \tag{2.9}$$

with an error term that is of third order in the time slice δt [47].

Space is discretized on a square or cubic lattice (lattice constant a_0 in each direction). The periodicity of the Brillouin zone is enforced by the substitution

$$\boldsymbol{k}\cdot\boldsymbol{\sigma} \mapsto a_0^{-1}\sum_{\alpha}\sigma_\alpha \operatorname{mod}(a_0k_\alpha, 2\pi, -\pi). \tag{2.10}$$

In 1D this is the linear sawtooth dispersion of Fig. 2.2, red curve. A discrete fast Fourier transform is inserted between the kinetic and potential terms, so that each is evaluated in the basis where the operators $\boldsymbol{k}$ and $\boldsymbol{r}$ are diagonal. The computational cost scales as $N\ln N$ for N lattice sites.

The eigenvalues $e^{i\varepsilon\delta t}$ of the unitary operator U define the quasi-energies

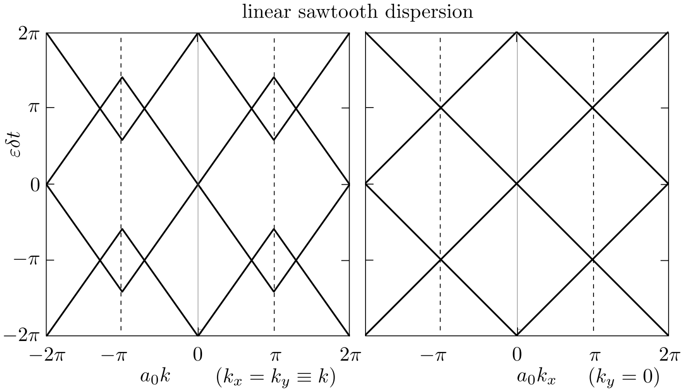

Figure 2.5: Cut through the bandstructure of Fig. 2.4 along the line $k_x = k_y \equiv k$ (left panel) and along the k_x-axis (right panel). In the former direction the dispersion has a discontinuous slope at the Brillouin zone boundaries (dotted lines).

ε modulo $2\pi/\delta t$. For free motion, $V = 0$, these are given by

$$(\varepsilon + 2\pi n/\delta t)^2 = v^2 \sum_{\alpha} k_\alpha^2, \quad n \in \mathbb{Z}, \quad |k_\alpha| < \pi/a_0. \tag{2.11}$$

The 2+1 dimensional band structure in the first Brillouin zone

$$\mathcal{B} = \{k_x, k_y, \varepsilon | -\pi < \varepsilon\delta t, k_x a_0, k_y a_0 < \pi\} \tag{2.12}$$

is plotted in Fig. 2.4 for $v = a_0/\delta t$, when the dispersion is strictly linear along the k_x and k_y-axes. (Alternatively, for $v = 2^{-1/2}\, a_0/\delta t$ the dispersion is strictly linear along the diagonal lines $k_x = \pm k_y$, the corresponding plots are in App. 2.A.)

The band structure repeats periodically upon translation by $\pm 2\pi/a_0$ in the k_x, k_y directions and by $\pm 2\pi/\delta t$ in the ε direction. Upon crossing a zone boundary the dispersion has a discontinuous derivative, see Fig. 2.5.

2.2.2. Smooth zone boundary crossings

To remove the discontinuity at the Brillouin zone boundary we modify the kinetic term in the evolution operator (2.9) in two ways: Firstly we approximate the exponent by a rational function (Cayley transform

[48, 49]),

$$e^{-iv\delta t\,\boldsymbol{k}\cdot\boldsymbol{\sigma}} = \frac{1-\frac{1}{2}iv\delta t\,\boldsymbol{k}\cdot\boldsymbol{\sigma}}{1+\frac{1}{2}iv\delta t\,\boldsymbol{k}\cdot\boldsymbol{\sigma}} + \mathcal{O}(\delta t^3). \tag{2.13}$$

The error of third order in the time slice is of the same order as the error in the operator splitting, Eq. (2.9).

Secondly we replace k_α by $(2/a_0)\tan(a_0k_\alpha/2)$, defining the modified evolution operator

$$\tilde{U} = e^{-iV(\boldsymbol{r})\delta t/2}\frac{1-i(v\delta t/a_0)\sum_\alpha \sigma_\alpha\tan(a_0k_\alpha/2)}{1+i(v\delta t/a_0)\sum_\alpha \sigma_\alpha\tan(a_0k_\alpha/2)}e^{-iV(\boldsymbol{r})\delta t/2}. \tag{2.14a}$$

The inverse of the sum of Pauli matrices can be worked out, resulting in

$$\tilde{U} = e^{-iV(\boldsymbol{r})\delta t/2}\frac{[1-\sum_\alpha\chi^2(k_\alpha)]\sigma_0 - 2i\sum_\alpha\sigma_\alpha\chi(k_\alpha)}{1+\sum_\alpha\chi^2(k_\alpha)}e^{-iV(\boldsymbol{r})\delta t/2}. \tag{2.14b}$$

We abbreviated $\chi(k) = (v\delta t/a_0)\tan(a_0k/2)$ and σ_0 is the 2×2 unit matrix. This looks more complicated than Eq. (2.9), but it can be computed equally efficiently since in both equations each operator is evaluated in the basis where it is diagonal.

The required periodicity when $k_\alpha \mapsto k_\alpha + 2\pi/a_0$ is automatically ensured by the replacement of the linear momentum by the tangent, it does not need to be enforced by hand as in Eq. (2.10). Although $\tan(a_0k_\alpha/2)$ has a pole when $k_\alpha = \pi/a_0$, this pole is removed in the evolution operator (2.14) — which has no singularity at the Brillouin zone boundaries.

The eigenvalues $e^{i\varepsilon\delta t}$ of $\tilde{U}$ for free motion, $V=0$, are given by

$$\tan^2(\varepsilon\delta t/2) = (v\delta t/a_0)^2\sum_\alpha\tan^2(a_0k_\alpha/2), \tag{2.15}$$

plotted in Figs. 2.6 and 2.7. Comparison with Figs. 2.4 and 2.5 shows that the zone boundaries are now joined smoothly. The dispersion is approximately linear near $\boldsymbol{k}=0$ and exactly linear along the lines $k_x=0$ and $k_y=0$ if we choose the discretization units such that $v = a_0/\delta t$. (See App. 2.A for the case $v = 2^{-1/2}\,a_0/\delta t$, when the linear dispersion is along $k_x = \pm k_y$.)

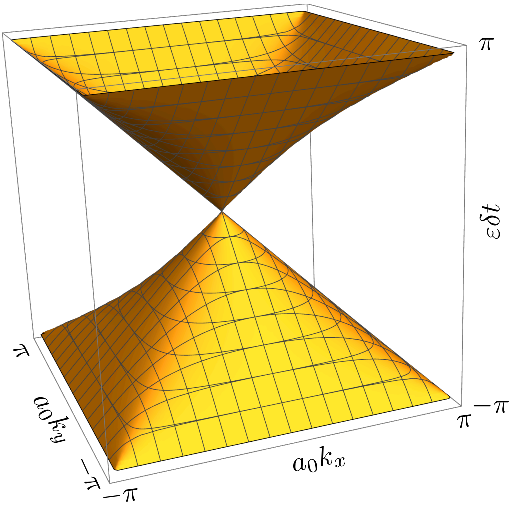

Figure 2.6: Same as Fig. 2.4, but now for the modified evolution operator (2.14) (with $v\delta t/a_0 = 1$).

2.3. Stability of the Dirac point

2.3.1. Protection by time-reversal symmetry

The condition of time-reversal symmetry for the unitary evolution operator U reads

$$\sigma_y U^* \sigma_y = U^{-1}, \tag{2.16}$$

where the complex conjugation should be taken in the real space representation, when $\boldsymbol{k} = -i\nabla$ changes sign. The time-reversal operator, $\sigma_y \times$ complex conjugation, squares to -1, so Kramers theorem applies: In the presence of a periodic potential V, when momentum $\boldsymbol{k}$ remains a good quantum number, the eigenvalues at $\boldsymbol{k} = 0$ should be at least doubly degenerate.[3]

Kramers degeneracy implies a band crossing at $\boldsymbol{k} = 0$ — provided that the bands depend smoothly on $\boldsymbol{k}$ — hence this applies to the evolution

---

[3] Kramers theorem may be more familiar for a Hermitian operator, the proof for a unitary operator proceeds similarly: If $U\psi = e^{i\phi}\psi$ with $\phi \in \mathbb{R}$, and $\sigma_y U^* \sigma_y = U^{-1}$, then $U\sigma_y\psi^* = \sigma_y(\sigma_y U^* \sigma_y \psi)^* = \sigma_y(U^{-1}\psi)^* = e^{i\phi}\sigma_y\psi^*$, thus ψ and $\sigma_y\psi^*$ are eigenstates of U with the same eigenvalue. They cannot be linearly related, because if $\psi = \lambda\sigma_y\psi^*$ for some $\lambda \in \mathbb{C}$, then $\sigma_y\psi^* = -\lambda^*\psi = -|\lambda|^2\sigma_y\psi^*$, which is impossible for $\psi \neq 0$. Hence the eigenvalue $e^{i\phi}$ is at least doubly degenerate.

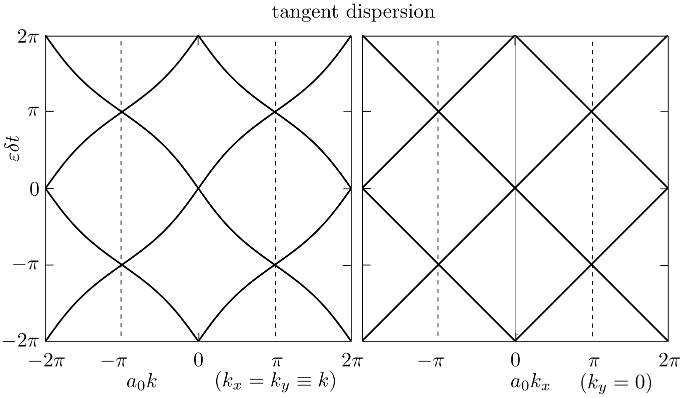

Figure 2.7: Cut through the bandstructure of Fig. 2.6 along the line $k_x = k_y \equiv k$ (left panel) and along the k_x-axis (right panel). In all directions the dispersion smoothly crosses the Brillouin zone boundaries (dotted lines).

operator $\tilde{U}$ for the tangent dispersion, but not to the operator U for the linear sawtooth dispersion. We conclude that the Dirac point of $\tilde{U}$ is protected by time-reversal symmetry, while the Dirac point of U is not.

We demonstrate this difference for the checkerboard potential

$$V(x, y) = V \cos[(\pi/a_0)(x + y)]. \tag{2.17}$$

(The calculation is described in App. 2.B.) In Fig. 2.8 we show the three ways in which this potential can affect the Dirac point. The evolution operator $\tilde{U}$ shows the modification T_0, while U shows T_-, see Fig. 2.9. The other option T_+ appears in Fig. 2.3 and in App. 2.A.

2.3.2. Protection by chiral symmetry

Chiral symmetry of the evolution operator is expressed by

$$\sigma_z U \sigma_z = U^{-1}. \tag{2.18}$$

Since $U^{-1} = U^\dagger$, this implies that U can be decomposed in the block form

$$U = \begin{pmatrix} A & B \\ -B^\dagger & C \end{pmatrix}, \quad A = A^\dagger, \quad C = C^\dagger. \tag{2.19}$$

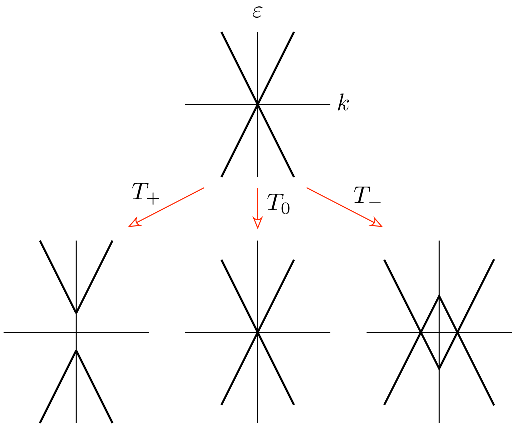

Figure 2.8: Top row: Dirac point in the quasi-energy dispersion $\varepsilon(k)$. Bottom row: Three topologically distinct modifications of the dispersion by the checkerboard potential. Only the Dirac point preserving modification T_0 is allowed for an evolution operator that depends smoothly on momentum.

We consider a 2D periodic potential, so that momentum $\boldsymbol{k} = (k_x, k_y)$ is a good quantum number. The band structure has winding number [50]

$$W = \frac{1}{2\pi} \operatorname{Im} \oint_{\Gamma} d\boldsymbol{k} \cdot \partial_{\boldsymbol{k}} \ln \det B(\boldsymbol{k}) \in \mathbb{Z} \tag{2.20}$$

along a contour Γ in the Brillouin zone on which $\det B$ does not vanish.[4] This is a topological invariant, it cannot change in response to a continuous perturbation [51]. A Dirac point within the contour is signaled by $W = \pm 1$. While pairs of Dirac points of opposite winding number can annihilate, a single Dirac point is protected by chiral symmetry — provided that the evolution operator is continuous.

The 2D Dirac Hamiltonian has chiral symmetry when $V \equiv 0$. An in-plane magnetization

$$M(x, y) = \mu_x(x, y)\sigma_x + \mu_y(x, y)\sigma_y \tag{2.21}$$

preserves the chiral symmetry. We are thus led to compare the two

---

[4] One has $\det B \neq 0$ on Γ if the quasi-energy $\varepsilon(\boldsymbol{k})$ does not cross 0 or π on that contour [50]. This prevents us from extending the contour along the entire first Brillouin zone, when the winding number should vanish.

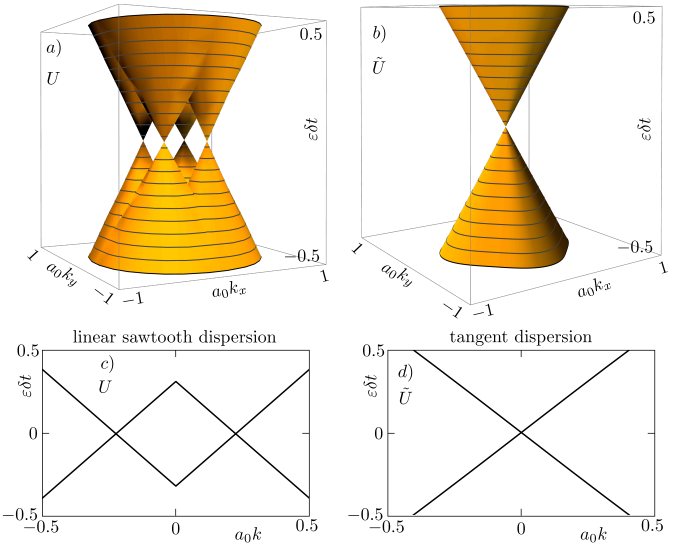

Figure 2.9: Quasi-energy bandstructure for the evolution operators U (panels a,c) and $\tilde{U}$ (panels b,d), in the presence of the 2D checkerboard potential (2.17) (for $V = 2/\delta t = 2\,v/a_0$). Panels c,d show a cut through the bandstructure for $k_x = k_y \equiv k$.

evolution operators

$$U = e^{-iM(x,y)\delta t/2} e^{-i(v\delta t/a_0)\sum_{\alpha=x,y}\sigma_\alpha \bmod (a_0k_\alpha, 2\pi, -\pi)} e^{-iM(x,y)\delta t/2}, \tag{2.22}$$

$$\tilde{U} = e^{-iM(x,y)\delta t/2} \frac{1 - i(v\delta t/a_0)\sum_{\alpha=x,y}\sigma_\alpha \tan(a_0k_\alpha/2)}{1 + i(v\delta t/a_0)\sum_{\alpha=x,y}\sigma_\alpha \tan(a_0k_\alpha/2)} e^{-iM(x,y)\delta t/2}. \tag{2.23}$$

Both satisfy the chiral symmetry relation (2.18), $\tilde{U}$ is a continous function of $\boldsymbol{k}$ while U is not.

The implication for the stability of the Dirac point is shown in Fig. 2.10, where we compare the bandstructure in the presence of the checkerboard magnetization

$$M(x, y) = \mu\sigma_x \cos[(\pi/a_0)(x + y)] \tag{2.24}$$

(see App. 2.B). A gap opens for U (linear sawtooth dispersion), while the

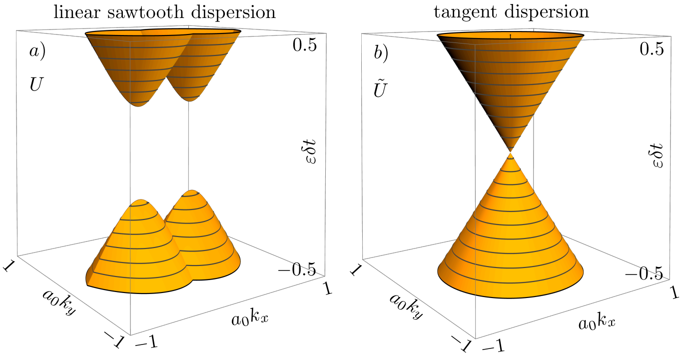

Figure 2.10: Quasi-energy bandstructure for the evolution operators U (panel a) and $\tilde{U}$ (panel b), in the presence of the checkerboard magnetization (2.24) (for $\mu = 2/\delta t = 2\,v/a_0$).

Dirac point for $\tilde{U}$ (tangent dispersion) remains unaffected.

2.4. Conclusion

In conclusion, we have presented a method to cure a fundamental deficiency of the split-operator technique for the space-time discretization of the Dirac equation [42]. The linear sawtooth representation of the momentum operator preserves the time-reversal and chiral symmetries of the continuum limit, but it breaks the topological protection of the Dirac cone that these symmetries should provide. The deficiency originates from the discontinuity of the discretized time-evolution operator at the boundaries of the Brillouin zone. We have demonstrated the breakdown of the topological protection for a simple model: a periodic potential (or magnetization) on a 2D square lattice (lattice constant a_0) which couples the Dirac point at $k = 0$ to the zone boundaries at $k = \pi/a_0$.

To restore the topological protection we modify the split-operator technique without compromising its computational efficiency, basically by replacing a_0k in the evolution operator by $2\tan(a_0k/2)$. Since the momentum operators are evaluated in the basis where they are diagonal, this is a "drop-in" replacement — it does not degrade the $N\ln N$ efficiency of the split-operator algorithm.

One open problem of the split-operator technique that is not addressed by our modification is the difficulty to incorporate the vector potential in a gauge invariant way [52]. For that purpose it would be useful to formulate

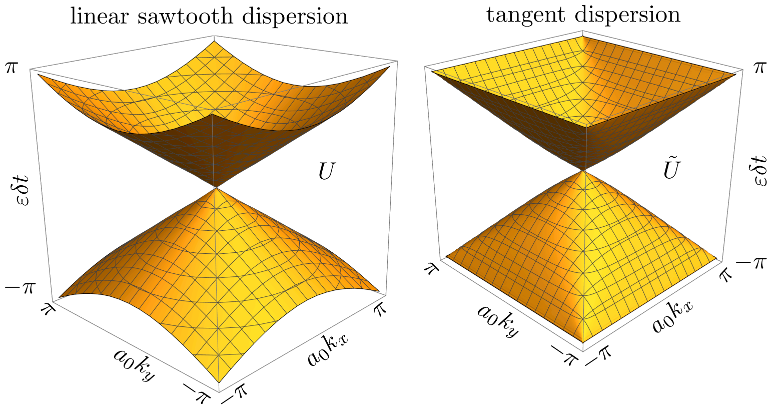

Figure 2.11: Free evolution ($V = 0$) bandstructures of U (left panel) and of $\tilde{U}$ (right panel), for $v = 2^{-1/2}\, a_0/\delta t$.

the split-operator technique fully in real space. This is done in Ref. [45] for the original approach with the linear sawtooth momentum operator. In App. 2.C we show that our tangent modification also allows for a real space formulation.

The availability of a single-cone discretization scheme which is efficient and which does not break the topological protection is a powerful tool for dynamical studies of massless Dirac fermions. One application to Klein tunneling has been published recently [53].

2.A. Bandstructures for $\mathbf{v = 2^{-1/2}\, a_0/\delta t}$

The bandstructures in the main text are for space-time discretization units such that $v = a_0/\delta t$, when the dispersion is strictly linear along the lines $k_x = 0$ and $k_y = 0$. Alternatively, one can have a strictly linear dispersion along the diagonals $k_x = \pm k_y$, by choosing $v = 2^{-1/2}\, a_0/\delta t$. The bandstructures of U and $\tilde{U}$ for free evolution are shown in Fig. 2.11.

For $v = 2^{-1/2}\, a_0/\delta t$ the checkerboard potential in the main text varies along the diagonals where U is continuous, so it does not affect the Dirac point. Instead we choose here a staggered potential $V(x, y) = V \cos(\pi x/a_0)$ that varies along the x-axis. [In Eq. (2.26) we thus replace $(k_x + \pi, k_y + \pi)$ by $(k_x + \pi, k_y)$.] The effect on U is the T_+ gap-opening process of Fig. 2.8, while the Dirac point of $\tilde{U}$ is unaffected, see Fig. 2.12. We can also take the

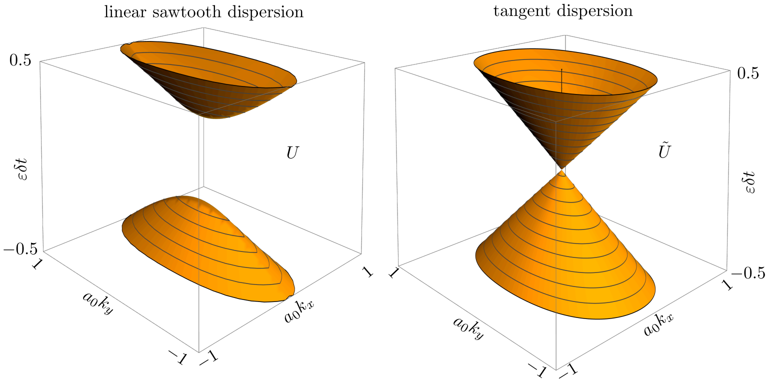

Figure 2.12: Same as Fig. 2.11, but now in the presence of the potential $V(x,y) = V\cos(\pi x/a_0)$ with $V = 2\,\delta t$. The bandstructures for the staggered magnetization $M(x,y) = \mu\sigma_x\cos[(\pi/a_0)x]$ look very similar.

staggered magnetization $M(x,y) = \mu\sigma_x\cos[(\pi/a_0)x]$, with bandstructures very similar to those in Fig. 2.12.

2.B. Bandstructure in the checkerboard potential

In this appendix we choose $v = a_0/\delta t$ and set the discretization units $a_0, \delta t$ to unity. We compute the eigenvalues of the evolution operators U and $\tilde{U}$ in the presence of the 2D checkerboard potential $V(x,y) = V\cos[\pi(x+y)]$. This potential couples states at (k_x, k_y) and $(k_x+\pi, k_y+\pi)$ with amplitude $V/2$.

We denote by $U_0(\boldsymbol{k})$ and $\tilde{U}_0(\boldsymbol{k})$ the free evolution operators, for $V = 0$, given by

$$U_0(\boldsymbol{k}) = \exp\left(-i{\textstyle\sum_\alpha}\sigma_\alpha \operatorname{mod}(k_\alpha, 2\pi, -\pi)\right), \tag{2.25a}$$

$$\tilde{U}_0(\boldsymbol{k}) = \frac{1 - i\sum_\alpha \sigma_\alpha \tan(k_\alpha/2)}{1 + i\sum_\alpha \sigma_\alpha \tan(k_\alpha/2)}. \tag{2.25b}$$

The quasi-energies $e^{i\varepsilon}$ are the eigenvalues of the 4×4 matrices

$$\mathcal{U} = \mathcal{V}\begin{pmatrix} U_0(k_x,k_y) & 0 \\ 0 & U_0(k_x+\pi,k_y+\pi)\end{pmatrix}\mathcal{V}, \tag{2.26a}$$

$$\tilde{\mathcal{U}} = \mathcal{V}\begin{pmatrix} \tilde{U}_0(k_x,k_y) & 0 \\ 0 & \tilde{U}_0(k_x+\pi,k_y+\pi)\end{pmatrix}\mathcal{V}. \tag{2.26b}$$

The 2×2 blocks at (k_x,k_y) and $(k_x+\pi,k_y+\pi)$ are coupled by the matrix

$$\mathcal{V} = \exp\left[-\frac{i}{2}\begin{pmatrix} 0 & V/2 \\ V/2 & 0\end{pmatrix}\right] = \begin{pmatrix} \cos(V/4) & -i\sin(V/4) \\ -i\sin(V/4) & \cos(V/4)\end{pmatrix}. \tag{2.27}$$

Results for $V=2$ are plotted in Fig. 2.9.

For $\tilde{\mathcal{U}}$ the Dirac point at $\boldsymbol{k}=0$ is not affected by the checkerboard potential. In contrast, for $\mathcal{U}$ the T_- modification of Fig. 2.8 replaces the band crossing at $\boldsymbol{k}=0$ by four band crossings at $\pm(q,q)$ and $\pm(q,-q)$, with

$$\cos\left(\frac{\pi-2q}{\sqrt{2}}\right) = \cos\left(\frac{\pi}{\sqrt{2}}\right)\cos(V/2) \Rightarrow q = 0.067\,V^2 + \mathcal{O}(V^4). \tag{2.28}$$

The calculation for a checkerboard magnetization $M(x,y) = (\mu_x\sigma_x + \mu_y\sigma_y)\cos[\pi(x+y)]$ proceeds entirely similar, upon replacement of $\mathcal{V}$ by

$$\mathcal{M} = \exp\left[-\frac{i}{4}\begin{pmatrix} 0 & \mu_x - i\mu_y \\ \mu_x + i\mu_y & 0\end{pmatrix}\right]. \tag{2.29}$$

The bandstructure for $\mu_x=2$, $\mu_y=0$ is shown in Fig. 2.10. For evolution operator $\mathcal{U}$ the spectrum acquires a gap $\Delta\epsilon = 0.095\,\mu_x^2 + \mathcal{O}(\mu_x^4)$. For $\tilde{U}$ the Dirac cone remains gapless.

2.C. Real-space formulation of the split-operator discretized evolution operator

2.C.1. Implicit finite-difference equation

The discretized Dirac equation for the tangent dispersion, $\Psi(t+\delta t) = \tilde{U}\Psi(t)$ with $\tilde{U}$ given by Eq. (2.14), can be rewritten as a *local* implicit finite-difference equation in real space — without requiring a Fourier transform to momentum space.

We introduce the translation operator $r_\alpha \mapsto r_\alpha + a_0$ on a square or cubic lattice, given by $T_\alpha = e^{a_0 \partial_\alpha}$, with $\partial_\alpha = \partial/\partial r_\alpha = ik_\alpha$. We note the identity

$$i \tan(a_0 k_\alpha/2) = \frac{T_\alpha - 1}{T_\alpha + 1}. \tag{2.30}$$

The product operators

$$D_0 = \tfrac{1}{4} \prod_\alpha (T_\alpha + 1), \quad D_\alpha = \tfrac{1}{2}(T_\alpha - 1) \prod_{\alpha' \neq \alpha} (T_{\alpha'} + 1) \tag{2.31}$$

couple nearby sites on the lattice.

The split-operator evolution equation

$$\Psi(t + \delta t) = e^{-iV(\boldsymbol{r})\delta t/2} \frac{1 - i(v\delta t/a_0) \sum_\alpha \sigma_\alpha \tan(a_0 k_\alpha/2)}{1 + i(v\delta t/a_0) \sum_\alpha \sigma_\alpha \tan(a_0 k_\alpha/2)} e^{-iV(\boldsymbol{r})\delta t/2} \Psi(t) \tag{2.32}$$

can be rewritten identically in terms of these local operators,

$$\begin{aligned} \left(D_0 + \frac{v\delta t}{2a_0} \sum_\alpha \sigma_\alpha D_\alpha \right) e^{iV(\boldsymbol{r})\delta t/2} \Psi(t + \delta t) = \\ = \left(D_0 - \frac{v\delta t}{2a_0} \sum_\alpha \sigma_\alpha D_\alpha \right) e^{-iV(\boldsymbol{r})\delta t/2} \Psi(t). \end{aligned} \tag{2.33}$$

The finite-difference equation (2.33) of the form $A\Psi(t + \delta t) = B\Psi(t)$ is called "implicit", because one needs to solve for the unknown $\Psi(t + \delta t)$ given the known $\Psi(t)$. The matrices A and B are both sparse, each of the N sites on the 2D square lattice is only coupled to its four nearest neighbors. The method of nested dissection then allows for an efficient solution of the finite difference equation [54–56]: There is an initial $N^{3/2}$ overhead from the LU decomposition of the matrix A, but subsequently the computational cost per time step scales as $N \ln N$ with the number of lattice sites, which is the same scaling as the split-operator algorithm.

2.C.2. Computational efficiency

To check the efficiency of the discretization schemes we have calculated[5] the spreading of a wave packet in a 2D disordered lattice (of $M \times M$ sites, with periodic boundary conditions in x- and y-directions). We take a random potential $V(x, y)$ which varies independently on each of the $N = M^2$ sites, uniformly in the interval $(-0.5, 0.5) \times \hbar v/a_0$. The initial state is

$$\Psi(x, y, 0) = (4\pi w^2)^{-1/2} e^{ik_0 x} e^{-(x^2+y^2)/2w^2} \begin{pmatrix} 1 \\ 1 \end{pmatrix}, \tag{2.34}$$

with parameters $k_0 = 0.5/a_0$, $w = 30\, a_0$. We follow the time evolution for $T = 10^3$ time steps $\delta t = 2^{-1/2} a_0/v$.

We compare the run time of the finite-difference code for a range of values of N, distinguishing the time t_{initial} spent on the initial LU decomposition from the run time $t_{\text{evolution}}$ per time step needed for the subsequent evolution of the wave packet. (The full run time of the code is $t_{\text{initial}} + T t_{\text{evolution}}$.)

The data shown in Fig. 2.13 is consistent with the expected scaling $t_{\text{initial}} \propto N^{3/2}$ and $t_{\text{evolution}} \propto N \ln N$. The storage requirements also scale as $N \ln N$, governed by the number of nonzero matrix elements in the LU decomposition.

We also show in the same plot the run time per time step for the split-operator algorithm. There is no initialization overhead in that case, the full run time is set by the $N \ln N$ cost of the fast Fourier transform.

---

[5] The computer code used in Sec. 2.C.2 to test the efficiency of the split-operator and finite-difference algorithms is available at the Zenodo repository: `https://dx.doi.org/10.5281/zenodo.7057254`

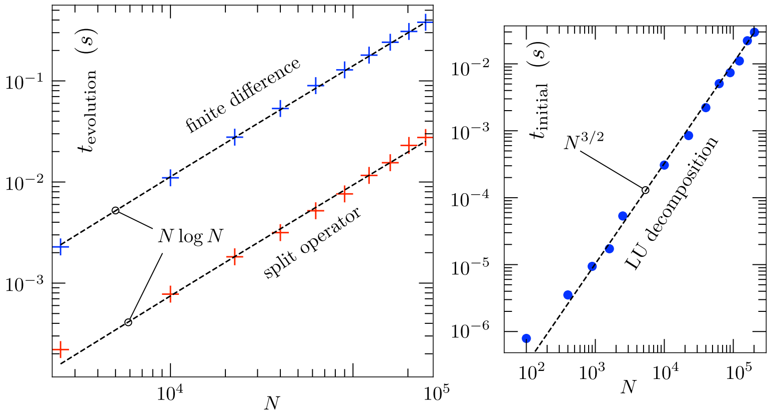

Figure 2.13: Demonstration of the favorable $N \ln N$ scaling with the number N of lattice points of the single-cone discretization scheme with the tangent dispersion. The plot at the left shows the run time $t_{\mathrm{evolution}}$ per time step for the evolution of the wave packet (3.7) through a disordered 2D system: red symbols for the split-operator approach, blue symbols for the implicit finite-difference approach. The latter approach has an initial overhead $t_{\mathrm{initial}} \propto N^{3/2}$ from the LU decomposition, shown in the right plot.

CHAPTER 3

Reflectionless Klein tunneling of Dirac fermions: Comparison of split-operator and staggered-lattice discretization of the Dirac equation

3.1. Introduction

Massless Dirac fermions have an energy-independent velocity, so if they move uphill in a potential landscape they are not slowed down. Even an infinitely high potential barrier cannot stop a particle approaching along a field line. This counterintuitive behavior is referred to as the Klein paradox, and the perfect transmission through a potential barrier is called Klein tunneling. It plays a central role in the "electron quantum optics" of Dirac materials, such as graphene, topological insulators, and Weyl semimetals [57, 58].

The Dirac fermions on the two-dimensional (2D) surface of a 3D topological insulator are of particular interest because they work around the "no-go" theorem for the impossibility to place a single species of massless Dirac fermions on a lattice [3]. The work-around consists in spatially separating two Dirac cones, one on the top surface and one on the bottom surface of the insulating material [59, 60]. An unpaired Dirac cone is topologically protected: electrostatic disorder cannot open up a gap and Klein tunneling is fully reflectionless.

Computer simulations of the electron dynamics on the 2D surface could work with a 3D lattice, but because this is computationally expensive there is a need for methods to implement a single Dirac cone on a 2D lattice.[1] Here we compare two such methods, using Klein tunneling as a test case for the presence or absence of fermion doubling.

Both methods discretize the time-dependent Dirac equation,

$$i\hbar\frac{\partial}{\partial t}\Psi(\boldsymbol{r},t) = v_0 \sum_{\alpha=x,y}(p_\alpha + eA_\alpha)\sigma_\alpha\Psi(\boldsymbol{r},t) + V\Psi(\boldsymbol{r},t), \tag{3.1}$$

where v_0 is the energy-independent velocity of the massless electrons (Dirac fermions), V and $\boldsymbol{A}$ are scalar and vector potentials, and the σ_α's are Pauli spin matrices. One method works in real space on a staggered space-time lattice [61, 62], the other method is the one introduced in chapter 2, and it works in Fourier space using a split-operator technique [63].

The staggered-lattice discretization is due to Hammer, Pötz, and Arnold (HPA) [61, 62], and has been applied to a variety of problems in condensed matter physics [64–67]. For free fermions ($V, \boldsymbol{A} \equiv 0$) it has the bandstructure

$$\sin^2(\varepsilon\delta t/2) = \gamma^2 \sum_{\alpha=x,y}\sin^2(a_0k_\alpha/2), \quad \gamma \equiv \frac{v_0\delta t}{a_0} \leq \frac{1}{\sqrt{2}}. \tag{3.2}$$

Here a_0 and δt are the lattice constants in space and time; $\boldsymbol{k}$ and ε are crystal momentum and quasi-energy.[2]

The split-operator discretization [63] builds on early work of Stacey [8, 26, 46]. The bandstructure has the same form as Eq. (3.2) — but with the sine replaced by a tangent,[3]

$$\tan^2(\varepsilon\delta t/2) = \gamma^2 \sum_{\alpha=x,y}\tan^2(a_0k_\alpha/2). \tag{3.3}$$

A unique property of the HPA technique is that it is fully gauge invariant [61, 62]. It is also highly efficient, because the time evolution is governed by

---

[1] An overview of methods to avoid fermion doubling in the context of lattice gauge theory can be found in chapter 4 of David Tong's lecture notes: `https://www.damtp.cam.ac.uk/user/tong/gaugetheory.html`.

[2] The quasi-energy ε is such that $\Psi(t+\delta t) = e^{i\varepsilon\delta t}\Psi(t)$, so the quasi-energy spectrum repeats itself with period $2\pi/\delta t$.

[3] The tangent $\tan(a_0k_\alpha/2)$ has a pole at the Brillouin zone boundary $k_\alpha = \pm\pi/a_0$, but the pole cancels from Eq. (3.3), which has a continuous quasi-energy dispersion $\varepsilon(\boldsymbol{k})$ for any real γ.

a direct, rather than implicit, difference equation, which moreover is local in real space. These features are lacking in the split-operator discretization [63], which motivated us to compare the two approaches in some detail.

Our central finding, presented in Sec. 3.2, is that the bandstructure (3.2) from the staggered-lattice discretization actually has two inequivalent Dirac cones in the first Brillouin zone: The Dirac points at $\boldsymbol{k} = 0$ and $\boldsymbol{k} = (2\pi/a_0, 0)$ are not related by a reciprocal lattice vector. This Brillouin zone doubling is avoided in the split-operator discretization. We assess the consequences for Klein tunneling in Sec. 3.3 and conclude in Sec. 4.5.

3.2. Brillouin zone doubling

The HPA technique modifies a staggered lattice discretization known as Susskind fermions [12, 19] and implemented in $2+1$ space-time dimensions in Ref. 68. In that approach the two components of the spinor $\Psi = (u, v)$ are discretized on separate lattices, displaced (staggered) from each other by $a_0/2$ and evaluated at alternating time slices (see Fig. 3.1a).

The Susskind fermion quasi-energy bandstructure [68],

$$\cos^2 \varepsilon\delta t = (1 - \gamma^2 + \gamma^2 \cos a_0 k_x \cos a_0 k_y)^2, \quad \gamma \leq 1, \tag{3.4}$$

has two inequivalent Dirac cones in the first Brillouin zone $\mathcal{B}$ shown in Fig. 3.1c, defined by

$$\mathcal{B} = \{k_x, k_y \in \mathbb{R} | -\pi/a_0 < k_x, k_y \leq \pi/a_0\}. \tag{3.5}$$

This is an improvement over the naive discretization, without staggering, which would have four inequivalent Dirac cones, at $(a_0 k_x, a_0 k_y) = (0, 0)$, (π, π), $(\pi, 0)$, and $(0, \pi)$. Susskind fermions do not have the last two, but the first two Dirac cones remain.

In Fig. 3.1b,d we show the HPA modification of the staggered lattice discretization. Comparison with Fig. 3.1a,c shows that the HPA unit cell has one half the area of the unit cell of the original square lattice. Accordingly, the first Brillouin zone $\mathcal{B}'$, defined by

$$\mathcal{B}' = \{k_x, k_y \in \mathbb{R} | -2\pi/a_0 < |k_x \pm k_y| \leq 2\pi/a_0\}, \tag{3.6}$$

has twice the area of $\mathcal{B}$.

Inspection of the HPA dispersion (3.2) then shows that, indeed, within $\mathcal{B}$ there is only a single Dirac cone, at $\boldsymbol{k} = 0$. However, within $\mathcal{B}'$ there is a second cone at the corner $\boldsymbol{k} = (2\pi/a_0, 0)$, see Fig. 3.2. (The other

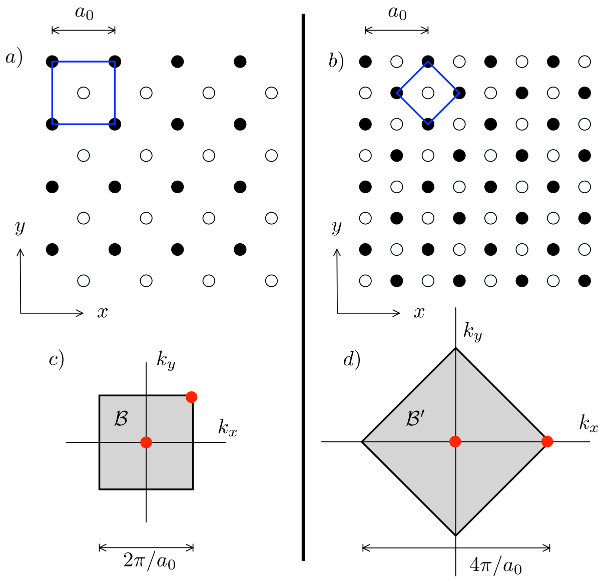

Figure 3.1: Comparison of two types of staggered grids for the spatial discretization of Dirac fermions, in the Susskind fermion approach (panel a, corresponding Brillouin zone $\mathcal{B}$ in panel c) and in the HPA modification (panel b, Brillouin zone $\mathcal{B}'$ in panel d). The black and white dots distinguish the u and v amplitudes of the spinor wave function $\Psi = (u, v)$. The blue squares give the unit cell of the lattice in real space, the grey square is the first Brillouin zone in momentum space, the red dots indicate two inequivalent Dirac points.

Brillouin zone corners are related by a reciprocal lattice vector, so they are equivalent.) We conclude that, once we account for the Brillouin zone doubling, the HPA discretization still suffers from fermion doubling.

3.3. Klein tunneling

The second Dirac cone at the corner of the Brillouin zone $\mathcal{B}'$ is at a relatively large momentum, so it will not play a role if the potentials are smooth: only momenta near $\boldsymbol{k} = 0$ then matter and fermion doubling becomes irrelevant. But realistic disorder potentials may well vary on the scale of the lattice constant, and then fermion doubling has noticeable consequences.

We investigate that here for Klein tunneling [57, 58]: Massless Dirac

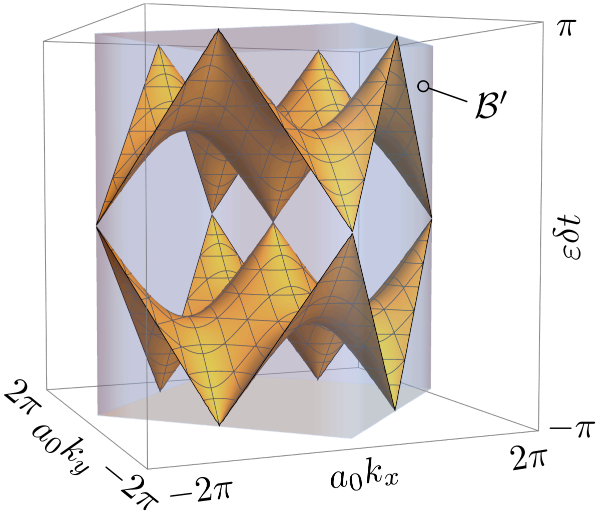

Figure 3.2: Quasi-energy bandstructure (3.2) of the HPA staggered lattice discretization, for $\gamma = 1/\sqrt{2}$, in the first Brillouin zone $\mathcal{B}'$ given by Eq. (3.6). There are two inequivalent Dirac cones, at center and corner of the Brillouin zone.

fermions are transmitted with unit probability when they approach a potential barrier at normal incidence, because conservation of chirality does not allow backscattering within a single Dirac cone. Coupling to a second cone will spoil that.

We contrast the numerical results following from the HPA staggered lattice technique [61] with those obtained using a manifestly single-cone discretization method [63] — a split-operator implementation of the Stacey discretization [8, 26, 46]. Both methods are summarized in App. 3.A and our numerical codes are available in a repository.[4]

We calculate the time dependence of a state $\Psi(x, y, t)$ incident along the x-axis on a rectangular barrier of height V_0 and width $50\,a_0$. The initial state is a Gaussian wave packet,

$$\Psi(x, y, 0) = (4\pi w^2)^{-1/2} e^{ik_0 x} e^{-(x^2+y^2)/2w^2} \begin{pmatrix} 1 \\ 1 \end{pmatrix}, \tag{3.7}$$

with parameters $k_0 = 0.5/a_0$, $w = 30\,a_0$ and normalization condition

---

[4] Our numerical codes are available at DOI:10.5281/zenodo.5877460.

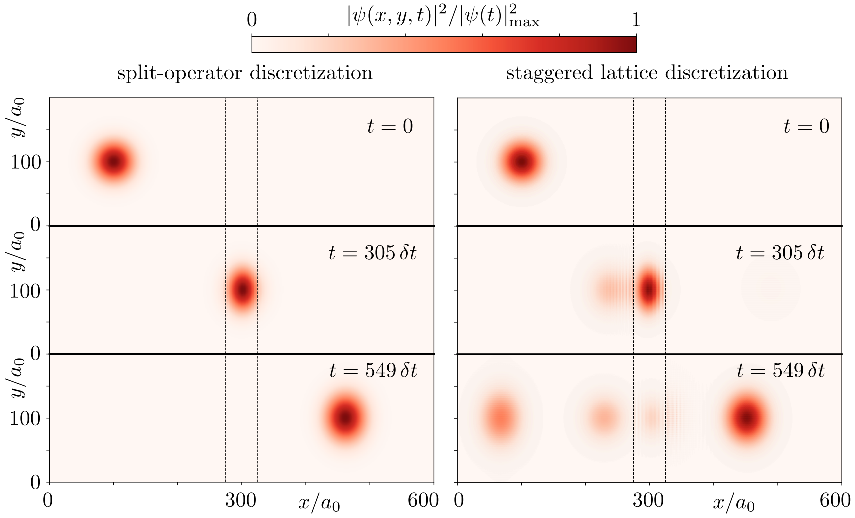

Figure 3.3: Three snapshots of the time-dependent simulation of Klein tunneling, in two alternative methods of discretization of the Dirac equation. A potential barrier of height $V_0 = 1.41\,\hbar/\delta t$ is located between the dotted lines. A wave packet at lower energy ($\bar{E} = 0.35\,\hbar/\delta t$) is normally incident on the barrier. The color scale shows $|\Psi|^2$ normalized to unit peak height at each of the three times.

$\int |\Psi|^2\, d\boldsymbol{r} = 1$. We choose the time step δt such that $\gamma = v_0\delta t/a_0 = 1/\sqrt{2}$. The mean energy is $\bar{E} = \hbar v_0 k_0 = 0.35\,\hbar/\delta t$, much less than the barrier height. The transmission probability T is obtained from the integral of $|\Psi|^2$ over the area to the right of the barrier, at the late time $t = 549\,\delta t$.

As shown in Figs. 3.3 and 3.4, when V_0 is larger than $\bar{E}$ the wave packet is fully transmitted when the Dirac equation is discretized using the split-operator method, but not in the HPA staggered lattice discretization.[5] For example, when $V_0 = 2\bar{E}$ we find, respectively, $T = 1.00$ and $T = 0.87$. We attribute the difference to fermion doubling.

To establish this, we have repeated the calculation with a periodic

---

[5] When V_0 is close to $\bar{E}$ the wave packet disperses side ways and backwards in the barrier region, hence the dashed dip in Fig. 3.4. This is not a lattice artefact, the dip would also appear in the continuum description.

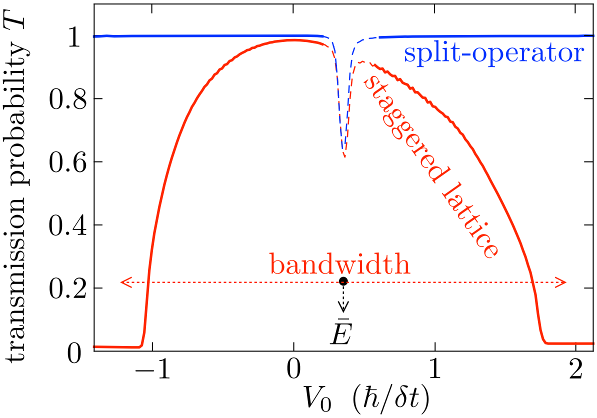

Figure 3.4: Transmission probability T through the potential barrier of Fig. 3.3, as a function of the barrier height V_0. The blue and red curves are for, respectively, the split-operator discretization and the staggered lattice discretization. The mean energy $\bar{E} = 0.35\,\hbar/\delta t$ of the incident wave packet (3.7) is indicated, as well as the finite bandwidth $\pi\hbar/\delta t$ of the staggered discretization. For the split-operator discretization $T \approx 1$ once $V_0 \gtrsim \bar{E}$, while for the staggered discretization T drops significantly below 1 well before $V_0 - \bar{E}$ reaches the bandwidth.

modulation of the barrier height,

$$V(x,y) = \begin{cases} 0 & \text{if } |x/a_0 - 300| > 25, \\ V_0 + \delta V \sin q_0 x & \text{if } |x/a_0 - 300| < 25. \end{cases} \tag{3.8}$$

The wave number $q_0 = 2\pi/a_0 - 2k_0$ is chosen such that it couples a right-moving state at energy $\bar{E} = \hbar v_0 k_0$ in the Dirac cone centered at $\boldsymbol{k} = (0,0)$ to a left-moving state in the Dirac cone centered at $\boldsymbol{k} = (2\pi/a_0, 0)$. As explained in Fig. 3.5, this coupling is forbidden by chirality conservation for the split-operator discretization, while it is allowed for the staggered lattice discretization. Fig. 3.6 shows that, indeed, a small potential modulation causes a nearly complete suppression of the transmission ($T = 0.06$) for the latter discretization only.

The suppressed transmission can be understood as the consequence of the opening of a gap at the Dirac point in the barrier region. The gapless Dirac cone is protected by time-reversal symmetry if there is only a single cone, but fermion doubling breaks that topological protection [41]. In App. 3.B we calculate the bandstructure for the staggered lattice discretization

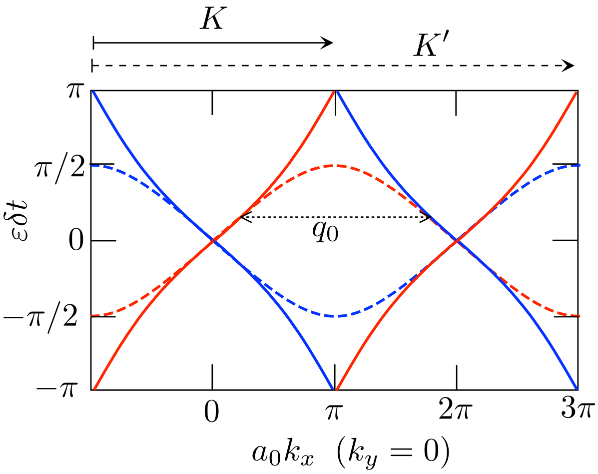

Figure 3.5: Dispersion relation along the k_x-axis for the split-operator discretization [solid curve, given by $\tan(\varepsilon\delta t/2) = \pm\gamma\tan(a_0k_x/2)$], and for the staggered lattice discretization [dashed curve, given by $\sin(\varepsilon\delta t/2) = \pm\gamma\sin(a_0k_x/2)$], both plotted for $\gamma = 1/\sqrt{2}$. The color red or blue distinguishes the eigenvalue ± 1 of σ_x (the chirality). The vectors K and K' are reciprocal lattice vectors for, respectively, the tangent and sine dispersions. A scalar potential can only couple branches of the same chirality. The momentum transfer q_0 thus leads to backscattering for the sine dispersion but it is forbidden for the tangent dispersion.

in the presence of the periodic potential $V(x,y) = V_0\cos(2\pi x/a_0)$. Along the $k_y = 0$ axis it is given by

$$\sin^2(\varepsilon\delta t/2) = \frac{(V_0\delta t/2)^2 + \gamma^2\sin^2(a_0k_x/2)}{1 + (V_0\delta t/2)^2}. \tag{3.9}$$

The gap at $\boldsymbol{k} = 0$ equals $2V_0$ for $V_0\delta t \ll 1$.

One might wonder at this stage whether the staggered lattice discretization is in any way an improvement over the naive discretization of the Dirac equation, without any staggering of the grid points. The staggering reduces the number of Dirac points in the 2D Brillouin zone from four to two — this is one advantage. But the coupling between the Dirac points is equally detrimental to Klein tunneling in the two discretization schemes, see App. 3.C.

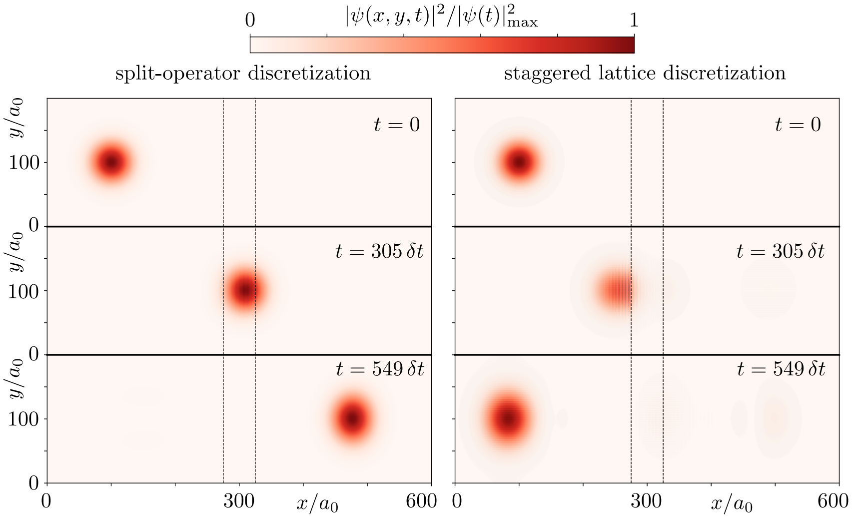

Figure 3.6: Same as Fig. 3.3, but for the modulated potential step (3.8) (with parameters $V_0 = 0.71\,\hbar/\delta t$, $\delta V = 0.071\,\hbar/\delta t$, $\bar{E} = 0.35\,\hbar/\delta t$).

3.4. Conclusion

In conclusion, we have uncovered a difficulty of staggered space-time lattice discretizations of the Dirac equation. In 2D staggered fermions *a la* Susskind have two Dirac cones in the Brillouin zone [12]. To eliminate this lattice artefact known as fermion doubling, Hammer, Pötz, and Arnold [61] introduced a space-time lattice with bandstructure

$$\varepsilon = \pm 2 \arcsin\left(v\sqrt{\sin^2(k_x/2) + \sin^2(k_y/2)}\right) \tag{3.10}$$

(in units where a_0 and δt are 1). The Susskind fermion Brillouin zone is $-\pi < k_x, k_y < \pi$ and in that Brillouin zone the bandstructure (3.10) has only a Dirac cone at the origin $\boldsymbol{k} = 0$.

What we have found is that this bandstructure is accompanied by Brillouin zone doubling: Along the k_x-axis it extends from $-2\pi < k_x < 2\pi$, so the Dirac cone at $\boldsymbol{k} = (2\pi, 0)$ is independent from the one at the origin — they are not related by a reciprocal lattice vector. We have shown that this fermion doubling has physical consequences in the breakdown of Klein tunneling.

To ascertain that fermion doubling is at the origin of these effects, we have compared with an alternative space-time discretization using a split-operator technique [63], with bandstructure

$$\varepsilon = \pm 2 \arctan\left(v \sqrt{\tan^2(k_x/2) + \tan^2(k_y/2)} \right). \tag{3.11}$$

The replacement of sine by tangent avoids the Brillouin zone doubling, essentially because $\sin(k/2)$ is 4π-periodic in k, while $\tan(k/2)$ is 2π-periodic. The Dirac cones at $\boldsymbol{k} = 0$ and $\boldsymbol{k} = (2\pi, 0)$ are now equivalent, related by a reciprocal lattice vector, and indeed we recover the Klein tunneling with unit probability expected for massless Dirac fermions.

The staggered lattice discretization has one feature that the split-operator discretization lacks: the possibility to include the vector potential in a fully gauge invariant way via the Peierls substitution [61, 62]. In chapter 4 we adapt the real space formulation of App. 2.C.1 to do precisely this.

3.A. Two methods of space-time discretization of the Dirac equation

In the main text we compare results from two space-time lattice discretizations of the Dirac equation, the staggered lattice approach of Ref. 61 and the split-operator approach of Ref. 63. We summarize these two methods.

3.A.1. Staggered lattice approach

Hammer, Pötz, and Arnold [61] discretize the $2+1$ dimensional Dirac equation on the space-time lattice shown in Fig. 3.7. The two components of the wave function $\Psi = (u, v)$ are evaluated on two different lattices, staggered in both space and time. The v-lattice is obtained from the u-lattice by a translation of $\delta t/2$ in the time direction and by $a_0/2$ in the x-direction. A translation of either u-lattice or v-lattice by $a_0/2$ in the x-direction without a time translation defines a third lattice of points $\boldsymbol{S}_{nms} = (x_n, y_m, t_s)$, the red points in Fig. 3.7. Each of these three lattices is face-centered square in the x–y plane, with the unit cell and Brillouin zone $\mathcal{B}'$ of Fig. 3.1b,d.

The finite-difference equation for the u component is (abbreviating

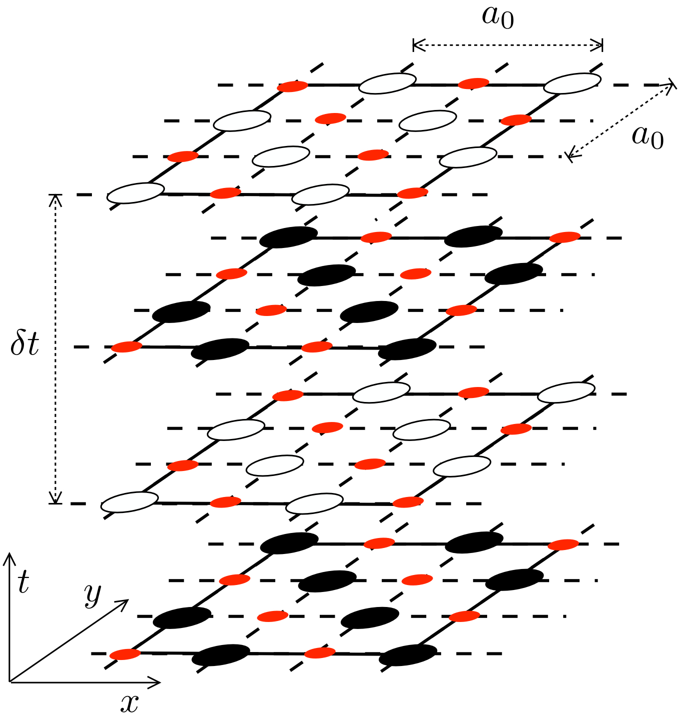

Figure 3.7: Space-time lattice in the HPA method of staggered lattice discretization of the 2+1 dimensional Dirac equation [61]. The u and v components of the spinor wave function $\Psi = (u, v)$ are indicated by black and white dots, respectively. The finite differences are evaluated at the red points.

$\gamma = v_0 \delta t / a_0$)

$$\begin{aligned} & i[u(x_n, y_m, t_s + \tfrac{1}{2}\delta t) - u(x_n, y_m, t_s - \tfrac{1}{2}\delta t)] = \\ = & - i\gamma[v(x_n + \tfrac{1}{2}a_0, y_m, t_s) - v(x_n - \tfrac{1}{2}a_0, y_m, t_s)] \\ & - \gamma[v(x_n, y_m + \tfrac{1}{2}a_0, t_s) - v(x_n, y_m - \tfrac{1}{2}a_0, t_s)] \\ & + \frac{\delta t}{2\hbar} V(x_n, y_m, t_s)[u(x_n, y_m, t_s + \tfrac{1}{2}\delta t) + u(x_n, y_m, t_s - \tfrac{1}{2}\delta t)], \quad (3.12a) \end{aligned}$$

for $(x_n, y_m, t_s \pm \frac{1}{2}\delta t)$ on the u-lattice. The arguments of the v-component are then located on the v-lattice. Similarly, the finite-difference equation for the v-component is

$$\begin{aligned}
&i[v(x_n,y_m,t_s+\tfrac{1}{2}\delta t)-v(x_n,y_m,t_s-\tfrac{1}{2}\delta t)]=\\
=&-i\gamma[u(x_n+\tfrac{1}{2}a_0,y_m,t_s)-u(x_n-\tfrac{1}{2}a_0,y_m,t_s)]\\
&+\gamma[u(x_n,y_m+\tfrac{1}{2}a_0,t_s)-u(x_n,y_m-\tfrac{1}{2}a_0,t_s)]\\
&+\frac{\delta t}{2\hbar}V(x_n,y_m,t_s)[v(x_n,y_m,t_s+\tfrac{1}{2}\delta t)+v(x_n,y_m,t_s-\tfrac{1}{2}\delta t)], \qquad (3.12\text{b})
\end{aligned}$$

for $(x_n, y_m, t_s \pm \frac{1}{2}\delta t)$ on the v-lattice. The computational cost of the solution of these difference equations scales linearly in N on an N-site lattice.

The quasi-energy bandstructure for $V = 0$ is given by

$$\sin^2(\varepsilon\delta t/2) = \gamma^2[\sin^2(a_0k_x/2) + \sin^2(a_0k_y/2)]. \qquad (3.13)$$

The requirement of a real quasi-energy ε restricts $\gamma^2 \leq 1/2$. The bandstructure in the first Brillouin zone is plotted in Fig. 3.2, for $\gamma = 1/\sqrt{2}$.

Figs. 3.3 and 3.6 show at time slice t_s both $|v(x_n, y_m, t_s)|^2$ and $|u(x_n + 1/2, y_m, t_s + 1/2)|^2$, each on its own staggered lattice. Because these amplitudes vary little over a lattice spacing other ways to compute $|\Psi|^2$, by averaging over nearby sites [61], do not make a significant difference.

3.A.2. Split-operator approach

The split-operator approach of Ref. 63 uses the same regular square lattice for both u and v components (Brillouin zone $|k_x|, |k_y| < \pi/a_0$). The time evolution $\Psi(t + \delta t) = U\Psi(t)$ is given by the unitary operator product ("split operator")

$$\begin{aligned}
U = e^{-iV(\boldsymbol{r})\delta t/2\hbar}\mathcal{F}^{-1}&\frac{1 - i\gamma\sum_\alpha \sigma_\alpha \tan(a_0k_\alpha/2)}{1 + i\gamma\sum_\alpha \sigma_\alpha \tan(a_0k_\alpha/2)}\\
&\cdot \mathcal{F}e^{-iV(\boldsymbol{r})\delta t/2\hbar}. \qquad (3.14)
\end{aligned}$$

The Fourier transform $\mathcal{F}$ performs a change of basis, so that the $\boldsymbol{r}$-dependent operators are evaluated in the real-space basis and the $\boldsymbol{k}$-dependent operators are evaluated in the momentum basis — at minimal computational cost. The cost of a Fast Fourier Transform scales as $N \log N$ on an N-site lattice.

The eigenvalues $e^{i\varepsilon t}$ of U for $V = 0$ depend on $\boldsymbol{k}$ according to

$$\tan^2(\varepsilon\delta t/2) = \gamma^2[\tan^2(a_0k_x/2) + \tan^2(a_0k_y/2)]. \qquad (3.15)$$

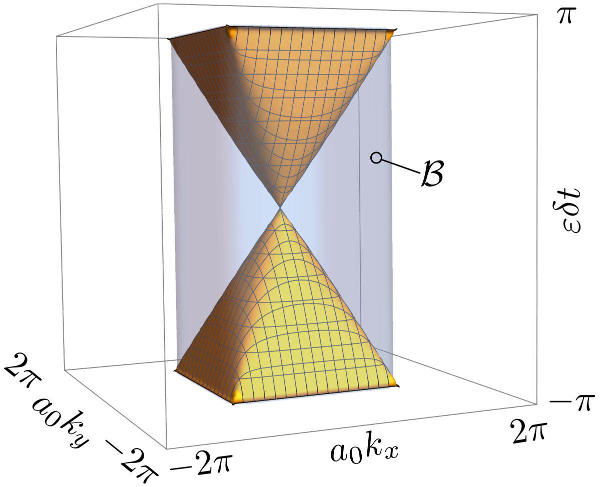

Figure 3.8: Quasi-energy bandstructure (3.15) of the split-operator discretization, for $\gamma = 1/\sqrt{2}$, in the first Brillouin zone $\mathcal{B}$ given by Eq. (3.5). There is only a single Dirac cone, at the center of the Brillouin zone.

The quasi-energy ε is real for any $\gamma > 0$. The bandstructure in the first Brillouin zone is plotted in Fig. 3.8, for $\gamma = 1/\sqrt{2}$.

3.B. Gap opening for the staggered lattice discretization

Because the staggered lattice discretization has two Dirac cones in the Brillouin zone, the gapless Dirac point is not protected by time-reversal symmetry — a gap can open without violating Kramers degeneracy. Here we show this by an explicit calculation.

The gap opening mechanism can be described as “fold and split”: a potential that varies on the scale of the lattice constant a_0 folds the Dirac cone at $\boldsymbol{k} = (2\pi/a_0, 0)$ onto the cone at $\boldsymbol{k} = (0, 0)$, and then the upper and lower cone can split apart while preserving the double degeneracy required by Kramers theorem.

We consider the periodic potential $V(x, y) = V(x+a_0, y) = V(x, y+a_0)$ and solve the finite difference equations (3.12) for the Bloch state $\Psi(x + a_0, y, t) = e^{ia_0k_x}\Psi(x, y, t)$, $\Psi(x, y + a_0, t) = e^{ia_0k_y}\Psi(x, y, t)$. There are four independent equations, involving the spinor amplitudes

$$\begin{aligned}&u_1(t) = u(0,0,t-\delta t/2),\;\; u_2(t) = u(a_0/2,a_0/2,t-\delta t/2),\\&v_1(t) = v(a_0/2,0,t),\;\; v_2(t) = v(0,a_0/2,t),\end{aligned} \tag{3.16}$$

and potential values $V_A = V(0,0)$, $V_B = V(a_0/2,a_0/2)$, $V_C = V(a_0/2,0)$, $V_D = V(0,a_0/2)$. The four equations can be written in the matrix form

$$\mathcal{P}\begin{pmatrix}u_1(t+\delta t)\\u_2(t+\delta t)\\v_1(t+\delta t)\\v_2(t+\delta t)\end{pmatrix} = \mathcal{Q}\begin{pmatrix}u_1(t)\\u_2(t)\\v_1(t)\\v_2(t)\end{pmatrix},$$

$$\mathcal{P} = \begin{pmatrix}i/\delta t - V_A/2 & 0 & 0 & 0\\ 0 & i/\delta t - V_B/2 & 0 & 0\\ i(e^{ia_0k_x}-1) & e^{-ia_0k_y}-1 & i/\delta t - V_C/2 & 0\\ 1-e^{ia_0k_y} & i(1-e^{-ia_0k_x}) & 0 & i/\delta t - V_D/2\end{pmatrix}, \tag{3.17a}$$

$$\mathcal{Q} = \begin{pmatrix}i/\delta t + V_A/2 & 0 & i(e^{-ia_0k_x}-1) & e^{-ia_0k_y}-1\\ 0 & i/\delta t + V_B/2 & 1-e^{ia_0k_y} & i(1-e^{ia_0k_x})\\ 0 & 0 & i/\delta t + V_C/2 & 0\\ 0 & 0 & 0 & i/\delta t + V_D/2\end{pmatrix}. \tag{3.17b}$$

The eigenvalues $e^{i\varepsilon\delta t}$ of the matrix product $\mathcal{P}^{-1}\mathcal{Q}$ give the bandstructure $\varepsilon(k_x,k_y)$. One readily recovers Eq. (3.2) for $V(x,y) \equiv 0$. For the potential $V(x,y) = V_0\cos(2\pi x/a_0)$ we set $V_A = V_D = V_0$, $V_B = V_D = -V_0$. Along the line $k_y = 0$ we then find the result (3.9), with a gap at $\boldsymbol{k} = 0$ of size

$$\Delta\varepsilon = \frac{4}{\delta t}\arcsin\left(\frac{V_0\delta t/2}{\sqrt{1+(V_0\delta t/2)^2}}\right). \tag{3.18}$$

We note that the topological protection of the Dirac cone for the split-operator discretization (3.14) was established in chapter 2 and in Ref. 63.

3.C. Klein tunneling of naive fermions

Fig. 3.4 compares the Klein tunneling probability for staggered-lattice and split-operator discretizations. For completeness, here we compare to

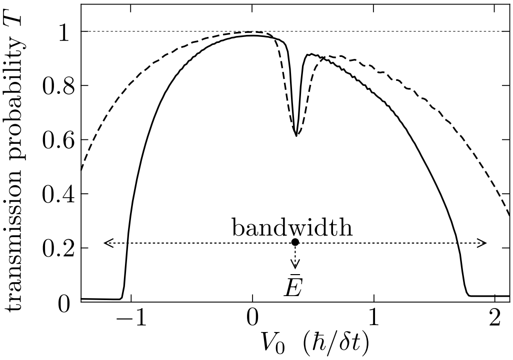

Figure 3.9: Same as Fig. 3.4, but now comparing the staggered-fermion discretization (solid curve) with the naive discretization (dashed curve). To have the same band width $\pi\hbar/\delta t$ in both cases we rescaled v_0 such that $\gamma = 1/\sqrt{2}$ in the former case and $\gamma = 2$ in the latter case.

the naive discretization, without any staggering.

We discretize the Dirac equation (3.1) on a space-time lattice by means of the Crank-Nicolson method,

$$\left(1 - \frac{i\delta t}{2\hbar} H\right) \Psi(\boldsymbol{r}, t + \delta t) = \left(1 + \frac{i\delta t}{2\hbar} H\right) \Psi(\boldsymbol{r}, t), \tag{3.19}$$

$$\begin{aligned} H\Psi(\boldsymbol{r}, t) &= V(\boldsymbol{r})\Psi(\boldsymbol{r}, t) \\ &+ \frac{\hbar v_0}{2ia_0} \sum_{\alpha=x,y} \sigma_\alpha [\Psi(\boldsymbol{r} + a_0\hat{\boldsymbol{r}}_\alpha, t) - \Psi(\boldsymbol{r} - a_0\hat{\boldsymbol{r}}_\alpha, t)]. \end{aligned} \tag{3.20}$$

The unit vectors $\hat{\boldsymbol{r}}_x, \hat{\boldsymbol{r}}_y$ point in the x- and y-directions. The vector potential may be included by Peierls substitution, but here we take zero magnetic field.

The naive-fermion bandstructure

$$\tan^2(\epsilon\delta t/2) = \tfrac{1}{4}\gamma^2(\sin^2 a_0 k_x + \sin^2 a_0 k_y), \quad \gamma = v_0\delta t/a_0, \tag{3.21}$$

has four inequivalent Dirac points in the first Brillouin zone, at $a_0\boldsymbol{k} = (0,0), (0,\pi), (\pi,0)$, and (π,π). The staggered discretization reduces that to two Dirac points.

The naive-fermion band width in the x-direction is $(4\hbar/\delta t)\arctan(\gamma/2)$. This is smaller than the band width $(4\hbar/\delta t)\arcsin\gamma$ of the staggered discretization — as expected, because the staggering introduces additional lattice points in the unit cell (see Fig. 3.1). To compare the two discretization schemes at the same band width, we take $\gamma = 1/\sqrt{2}$ for the staggered discretization and $\gamma = 2$ for the naive discretization — then in both cases the band width is $\pi\hbar/\delta t$.

Results are shown in Fig. 3.9. We conclude that the staggering does not significantly improve the Klein tunneling.

CHAPTER 4

Method to preserve the chiral-symmetry protection of the zeroth Landau level on a two-dimensional lattice

4.1. Introduction

4.1.1. Objective

We address, in a different context, a problem originating from lattice gauge theory: How to place fermions on a lattice in a way that respects both gauge invariance and chiral symmetry [3, 8, 11, 12, 19, 69–71]. Our context is topological insulators [72], three-dimensional (3D) materials having an insulating bulk and a conducting surface, with massless Dirac fermions as the low-energy excitations. The Landau level spectrum of massless Dirac fermions is anomalous, the zeroth Landau level is a flat band pinned to zero energy irrespective of the magnetic field strength [73, 74].

Our objective is to model the surface states on a two-dimensional (2D) lattice, without breaking the chiral symmetry that protects the zeroth Landau level from broadening by disorder. Let us introduce the problem in some detail.

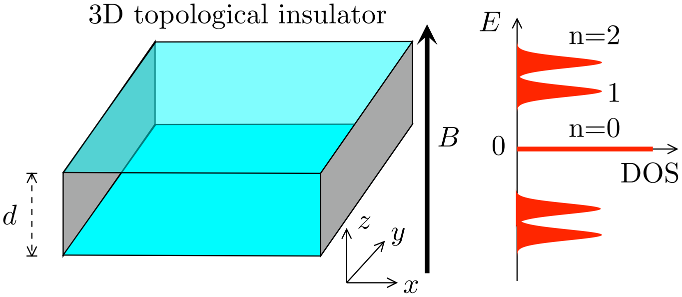

Figure 4.1: Slab of a topological insulator in a perpendicular magnetic field B. Landau levels form on the top and bottom surface at energy $|E| \propto \sqrt{n}$, $n = 0, 1, 2, \ldots$, symmetrically arranged around $E = 0$. The density of states (DOS) of the zeroth Landau level is not broadened by a spatially fluctuating B, provided that the slab thickness d is sufficiently large that the two surfaces are decoupled.

4.1.2. Zeroth Landau level

In a magnetic field B, perpendicular to the surface of the topological insulator, Landau levels form at energies $E_n = \pm\hbar\omega\sqrt{n}$, $n \in \mathbb{N}$, with $\omega \propto \sqrt{B}$. The zeroth Landau level $E_0 = 0$ is magnetic-field independent [75–78]. If the perpendicular field strength has spatial fluctuations, for example, because of ripples on the surface, all Landau levels are broadened *except* the zeroth Landau level [79].

The $E = 0$ flat band is protected by a chiral symmetry, a unitary and Hermitian operator Γ that anti-commutes with the Hamiltonian [80]. Indeed, the massless 2D Dirac Hamiltonian

$$H_\mathrm{D} = v\hbar k_x \sigma_x + v\hbar k_y \sigma_y \tag{4.1}$$

anticommutes with the Pauli matrix σ_z, and this symmetry is preserved if one introduces a space-dependent vector potential by $\hbar\boldsymbol{k} \mapsto \hbar\boldsymbol{k} - e\boldsymbol{A}(\boldsymbol{r})$.

Topological considerations [81–83] then enforce the existence of an $\mathcal{N}$-fold degenerate eigenstate at $E = 0$, with $\mathcal{N}$ the number of flux quanta through the surface. The flat band has a definite chirality, meaning that it is an eigenstate of $\Gamma = \sigma_z$ with eigenvalue ± 1 determined by the sign of the magnetic field.

If we consider a topological insulator in the form of a slab (see Fig. 6.1), the top and bottom surfaces each support a zeroth Landau level, of opposite chirality. The two flat bands will mix and split if the slab is so thin that the wave functions of opposite surfaces overlap, but in thick slabs this breakdown of the topological protection is exponentially small in the ratio of slab thickness and penetration depth.

4.1.3. 2D lattice formulation

A numerical simulation of the 3D system is costly, it would be more efficient to retain only the surface degrees of freedom. If we discretize the 2D surface on a square lattice (lattice constant a), the Hamiltonian must be periodic in the momentum components with period $2\pi/a$. The $\sin ak$ dispersion has the proper periodicity, but it suffers from fermion doubling [71]: a spurious massless degree of freedom appears at $k = \pi/a$.

We contrast two lattice formulations that avoid fermion doubling: an approach due to Wilson [11] with a sine+cosine dispersion, and an approach due to Stacey [8] with a tangent dispersion.

In Wilson's approach [11] the discretized Dirac Hamiltonian is

$$\begin{aligned} H_{\text{Wilson}} = (\hbar v/a) &\sum_{\alpha=x,y} \sigma_\alpha \sin ak_\alpha \\ &+ \Delta\sigma_z \sum_{\alpha=x,y} (1 - \cos ak_\alpha). \end{aligned} \tag{4.2}$$

The cosine term $\propto \Delta\sigma_z$ avoids fermion doubling, the only low-energy excitations are near $\boldsymbol{k} = 0$, but it breaks chiral symmetry: H_{Wilson} no longer anticommutes with $\Gamma = \sigma_z$.

The alternative approach due to Stacey [8] has a tangent dispersion,

$$H_{\text{Stacey}} = (2\hbar v/a) \sum_{\alpha=x,y} \sigma_\alpha \tan(ak_\alpha/2). \tag{4.3}$$

Fermion doubling is avoided without breaking chiral symmetry, at the expense of a nonlocal Hamiltonian: While sines and cosines of momentum only couple nearest neighboring sites, the tangent of momentum represents a long-range coupling.

The merit of Stacey's approach is that the nonlocal Schrödinger equation $H_{\text{Stacey}}\Psi = E\Psi$ can be cast in the form of a *generalized* eigenvalue problem,

$$\mathcal{H}\Psi = E\mathcal{P}\Psi, \tag{4.4}$$

with *local* operators $\mathcal{H}, \mathcal{P}$ given by [26]

$$\begin{aligned}\mathcal{H} = {}& \frac{\hbar v}{2a}\sigma_x(1+\cos ak_y)\sin ak_x \\ & + \frac{\hbar v}{2a}\sigma_y(1+\cos ak_x)\sin ak_y, \end{aligned} \tag{4.5a}$$

$$\mathcal{P} = \tfrac{1}{4}(1+\cos ak_x)(1+\cos ak_y). \tag{4.5b}$$

Because $\mathcal{H}$ and $\mathcal{P}$ are sparse Hermitian operators, and $\mathcal{P}$ is positive definite,[1] the generalized eigenvalue problem (4.4) can be solved efficiently.

4.1.4. Outline

We wish to show that the topological protection of the zeroth Landau in a 3D topological insulator can be obtained in a purely 2D formulation. To preserve chiral symmetry we work with the tangent dispersion, in the local representation (4.5).

The first step is to introduce the vector potential in a gauge invariant way — without breaking the locality of the generalized eigenvalue problem. We do this in the next Section 4.2. In Sec. 4.3 we calculate the Landau level spectrum. The zeroth Landau level contains states of both chiralities, we show that these can be spatially separated by adjoining $+B$ and $-B$ regions. The robustness of the flat band is assessed in Sec. 4.4. We conclude in Sec. 4.5.

4.2. Gauge invariant lattice fermions with a tangent dispersion

In Ref. 26 it was shown how the magnetic field can be incorporated in the generalized eigenvalue problem (4.5) in a way that is gauge invariant to first order in the flux through a unit cell. Here we will go beyond that calculation, and preserve gauge invariance to all orders.

For ease of notation we set $\hbar$ and the lattice constant a both equal to unity in most equations that follow. The electron charge is taken as $+e$, so that the vector potential enters in the Hamiltonian as $\boldsymbol{k} \mapsto \boldsymbol{k} - e\boldsymbol{A}$.

---

[1] The operator $\mathcal{P}$ is in general only positive semidefinite. It becomes positive definite if we choose an odd number of lattice points with periodic boundary conditions in the x– and y–directions.

We recall the definition of the translation operator,

$$T_\alpha \equiv e^{i\hat{k}_\alpha} = \sum_{\boldsymbol{n}} |\boldsymbol{n}\rangle\langle\boldsymbol{n}+\boldsymbol{e}_\alpha|. \tag{4.6}$$

The sum over $\boldsymbol{n}$ is a sum over lattice sites on the 2D square lattice, and $\boldsymbol{e}_\alpha \in \{\boldsymbol{e}_x, \boldsymbol{e}_y\}$ is a unit vector in the α-direction. The Peierls substitution ensures gauge invariance by the replacement

$$\begin{aligned} T_\alpha \mapsto \mathcal{T}_\alpha &= \sum_{\boldsymbol{n}} e^{i\phi_\alpha(\boldsymbol{n})}|\boldsymbol{n}\rangle\langle\boldsymbol{n}+\boldsymbol{e}_\alpha|, \\ \phi_\alpha(\boldsymbol{n}) &= e\int_{\boldsymbol{n}+\boldsymbol{e}_\alpha}^{\boldsymbol{n}} A_\alpha(\boldsymbol{r})\,dx_\alpha. \end{aligned} \tag{4.7}$$

Note that the A-dependent translation operators no longer commute,

$$\mathcal{T}_y\mathcal{T}_x = e^{2\pi i\varphi/\varphi_0}\mathcal{T}_x\mathcal{T}_y, \tag{4.8}$$

where φ is the flux through a unit cell in units of the flux quantum $\varphi_0 = h/e$.

One could now apply the Peierls substitution directly to the Hamiltonian H_{Stacey} from Eq. (4.3), but then one runs into the obstacle noted in Ref. 26: The transformation to a local generalized eigenvalue problem only succeeds to first order in A, higher order terms become nonlocal. Here we therefore follow a different route.

We rewrite the operators $\mathcal{H}$ and $\mathcal{P}$ from Eq. (4.5) in terms of the translation operators (4.6) and apply the Peierls substitution (4.7) at that level. Noting that $1+\cos k_\alpha = \frac{1}{2}(1+T_\alpha)(1+T_\alpha^\dagger)$, $\sin k_\alpha = \frac{1}{2i}(T_\alpha - T_\alpha^\dagger)$, we define

$$\begin{aligned} \mathcal{H} = {} & \frac{\hbar v}{8ia}\sigma_x(1+\mathcal{T}_y)(\mathcal{T}_x-\mathcal{T}_x^\dagger)(1+\mathcal{T}_y^\dagger) \\ & + \frac{\hbar v}{8ia}\sigma_y(1+\mathcal{T}_x)(\mathcal{T}_y-\mathcal{T}_y^\dagger)(1+\mathcal{T}_x^\dagger), \end{aligned} \tag{4.9a}$$

$$\mathcal{P} = \Phi\Phi^\dagger, \tag{4.9b}$$

$$\Phi = \tfrac{1}{8}(1+\mathcal{T}_x)(1+\mathcal{T}_y) + \tfrac{1}{8}(1+\mathcal{T}_y)(1+\mathcal{T}_x). \tag{4.9c}$$

Since $\mathcal{T}_x$ and $\mathcal{T}_y$ do not commute the order matters: In Eq. (4.9) we have ordered these translation operators such that $\mathcal{H}$ and $\mathcal{P}$ remain Hermitian, and moreover $\mathcal{P}$ remains positive definite. Both these properties are essential for an efficient solution of the generalized eigenvalue problem

$$\mathcal{H}\Psi = E\Phi\Phi^\dagger\Psi. \tag{4.10}$$

For completeness we note that a scalar potential V and a magnetization $\boldsymbol{M}$ can be included by adding to $\mathcal{H}$ the terms

$$\mathcal{H} \mapsto \mathcal{H} + \Phi V \Phi^\dagger + \Phi(\boldsymbol{M} \cdot \boldsymbol{\sigma})\Phi^\dagger. \tag{4.11}$$

The potential V and perpendicular magnetization M_z break chiral symmetry, while the parallel magnetizations M_x and M_y preserve it.

4.3. Chirality-resolved zeroth Landau level

4.3.1. Lattice obstruction to chirality polarization

The Landau levels of the Dirac Hamiltonian (4.1) are dispersionless flat bands at energies $\pm E_n$ given by [73, 74]

$$E_n = v\sqrt{2n\hbar e|B|}, \quad n = 0, 1, 2, \ldots. \tag{4.12}$$

Each Landau level has the same degeneracy $\mathcal{N}$ = number of flux quanta through the system. Both chiralities $C = \pm 1$ (eigenvalues of σ_z) contribute equally to each nonzero Landau level: $\langle n|\sigma_z|n\rangle = 0$ for $n \geq 1$. The zeroth Landau level, however, is polarized: $\langle 0|\sigma_z|0\rangle = \operatorname{sign} B$.

The topological protection of the zeroth Landau level rests on this chirality polarization: The chirality index $\mathcal{I}$ of the zero-mode, equal to the number of states with $C = +1$ minus the number of states with $C = -1$, is equal to $\mathcal{I} = (\operatorname{sign} B)\mathcal{N}$. If chiral symmetry is maintained the index is a topological invariant [81–83], preventing a broadening of the flat band.

All of this is for the continuum description. The fundamental obstacle faced by lattice fermions is that the chirality polarization of the zeroth Landau level is lost: A no-go theorem by Stacey [69] enforces that any gauge invariant lattice regularization of the Dirac Hamiltonian which preserves chiral symmetry must have the same number of zero-modes for either chirality. Hence, on the lattice $\mathcal{I} = 0$ and the topological protection breaks down.

That gauge invariance on a lattice is incompatible with a nonzero chirality index might be understood by a topological argument: A uniform magnetic field can be concentrated into an array of h/e flux tubes, each of which is fully contained within a unit cell. The chirality index cannot

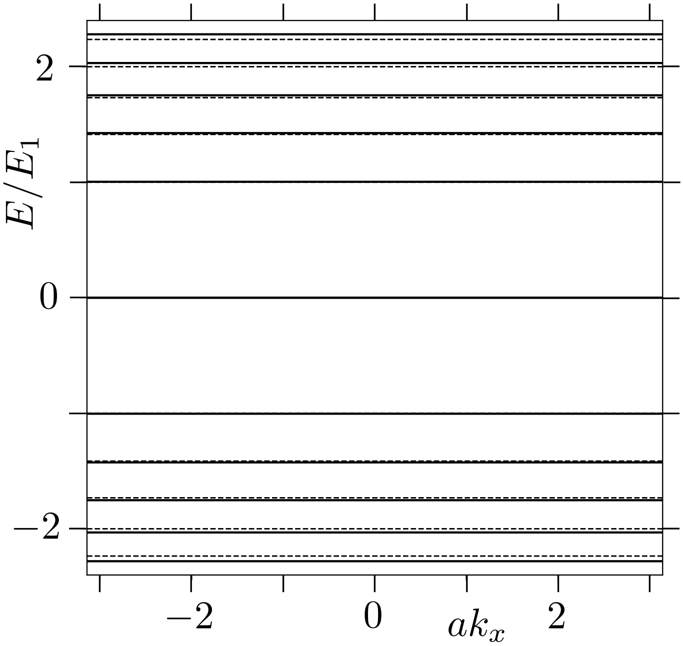

Figure 4.2: Solid lines: Dispersionless Landau levels in a uniform magnetic field $B_0 = (1/201)(h/ea^2)$, calculated from the generalized eigenvalue equation (4.10) in the gauge $\boldsymbol{A} = -B_0 y\hat{x}$. (Energies are plotted in units of $E_1 = \sqrt{2\hbar e v^2 B_0}$.) The dashed lines indicate the continuum limit (4.12). At each k_x-value there are two independent eigenstates in the zeroth Landau level, one with spin up and one with spin down. The other Landau levels each have only a single eigenstate at a given k_x, without any spin polarization.

change by such a smooth deformation, but the resulting magnetic field distribution may be gauged away on the lattice, hence $\mathcal{I}$ must be equal to zero.

4.3.2. Proposed work-around

In accord with these general considerations we have verified by explicit calculation (see Fig. 4.2) that the generalized eigenvalue problem (4.10) has an $\mathcal{N}$-fold degenerate zero-mode $E_0 = 0$ in both the $C = +1$ and $C = -1$ manifold.

To recover the chirality-resolved zeroth Landau we propose a method to spatially separate the opposite chirality manifolds: We double the system

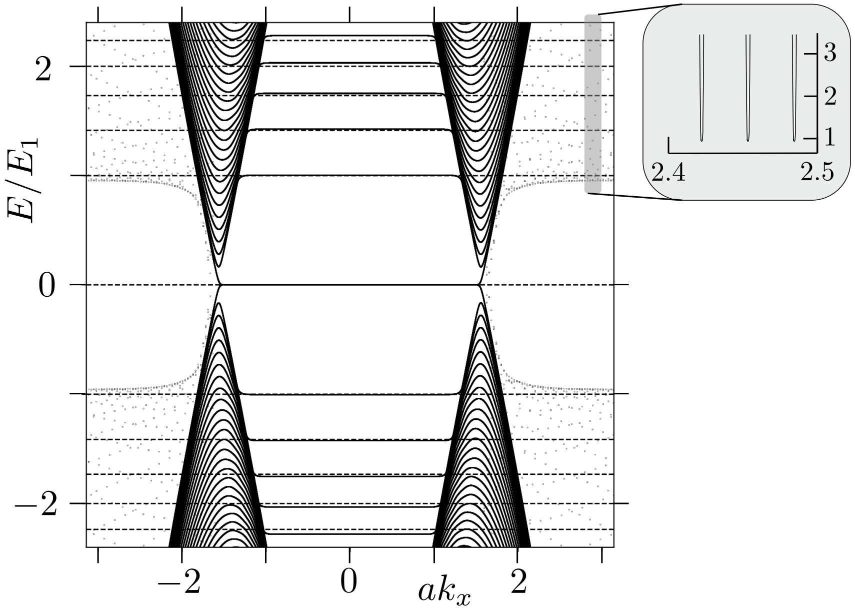

Figure 4.3: Same calculation as in Fig. 4.2, but for the non-uniform magnetic field profile with separate regions of $\pm B_0 = \pm(1/202)(h/ea^2)$. The full profile of length $4L_0 + a = 405\,a$ is repeated periodically along the y-axis and is translationally invariant along the x-axis. The scattered data points near the Brillouin zone boundaries (with a nearly vertical dispersion, see expanded inset) are a lattice artefact.

by adjoining a $+B$ and $-B$ region. Since then $\mathcal{I} = 0$ by construction, the zeroth Landau level in each of the two regions could be chirality polarized without violating the no-go theorem.

Our numerics, see Figs. 4.3 and 4.4, shows that this is indeed what happens: the states in the zeroth Landau level with $C = \pm 1$ are fully contained in the $\pm B$ region.

In the next section we will check to what extent this spatial separation of the chiralities is sufficient to protect the flat band.

4.4. Robustness of the flat band

We introduce chirality-preserving disorder by randomly varying the perpendicular magnetic field component $B(x,y)$. The random field is

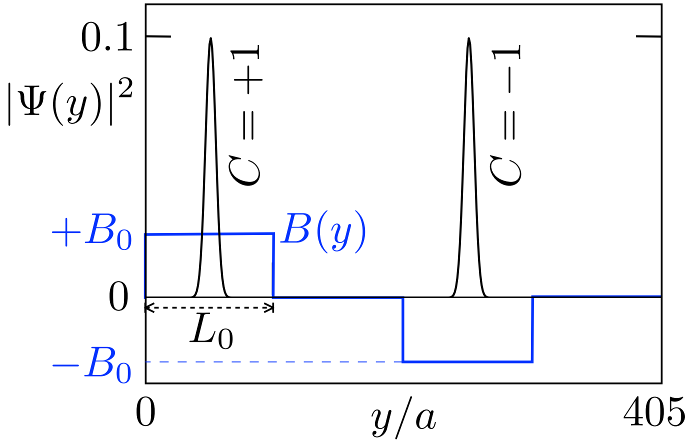

Figure 4.4: Wave function intensity profile in the zeroth Landau level for the band structure of Fig. 4.3, evaluated at $k_x = 0$. As indicated, the eigenstates with chirality $C = \pm 1$ (eigenvalue of σ_z) are spatially separated in the regions with magnetic field $\pm B_0$.

drawn independently on each lattice site, uniformly in the interval $(0, 2B_0)$ in the positive field region and in the interval $(-2B_0, 0)$ in the negative field region.

For the sake of illustration, it is helpful to first keep the translational invariance in the x-direction, so that $B(y)$ fluctuates only as function of y. We can then still plot a band structure as a function of k_x, see Fig. 4.5. All flat bands are destroyed by the disorder, except for the zeroth Landau level, which remains completely dispersionless. The spatial separation of the states of opposite chirality is crucial for this topological protection: In Fig. 4.6 we show that without it the zeroth Landau does broaden in the presence of disorder.

We next consider a disordered field $B(x, y)$ that fluctuates in both x– and y–directions. The wave number k_x is then no longer a good quantum number, instead of a band structure we plot the density of states near $E = 0$, to assess whether the zeroth Landau level is broadened. As shown in Fig. 4.7a the density of states peak persists with only a slight broadening in the disordered system.

Earlier studies of the Landau level spectrum of lattice fermions use Wilson's sine+cosine dispersion [84, 85], which breaks the chiral symmetry. In the Wilson Hamiltonian (4.2) the zeroth Landau level is displaced from

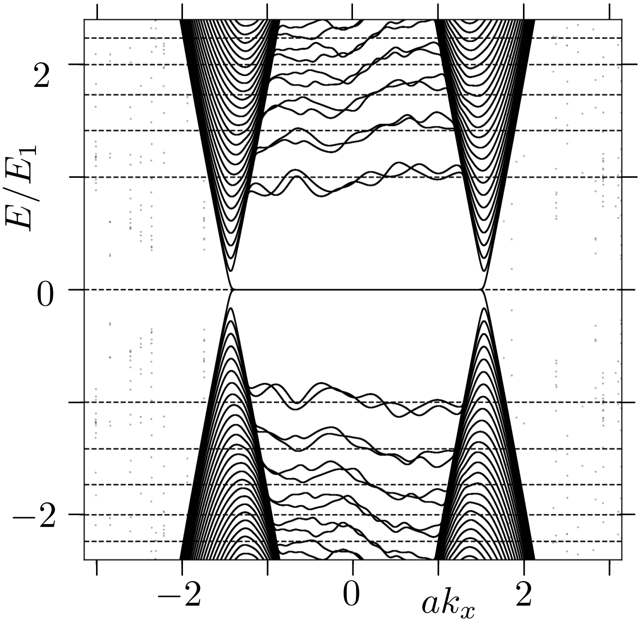

Figure 4.5: Same calculation as in Fig. 4.3, but now for a magnetic field that varies randomly in the y-direction. The zeroth Landau level is protected from broadening because the states of opposite chirality are spatially separated.

$E = 0$ by the Δ-dependent offset

$$\delta E = \tfrac{1}{2} eBa^2\Delta/\hbar. \tag{4.13}$$

The Wilson mass Δ is of order $\hbar v/a$ to effectively gap out the low energy excitations at $k = \pi/a$, hence $\delta E \simeq eBav$.

In Fig. 4.7b we show results for the density of states, computed from the Wilson Hamiltonian for the same magnetic field value as in Fig. 4.7a. Without disorder the only difference with the tangent dispersion is the shift (4.13) of the zeroth Landau level, but with disorder the difference is quite dramatic.

4.5. Conclusion

In summary, we have shown how the quantum Hall effect in a 3D topological insulator can be simulated on a 2D lattice. In a sense, the top

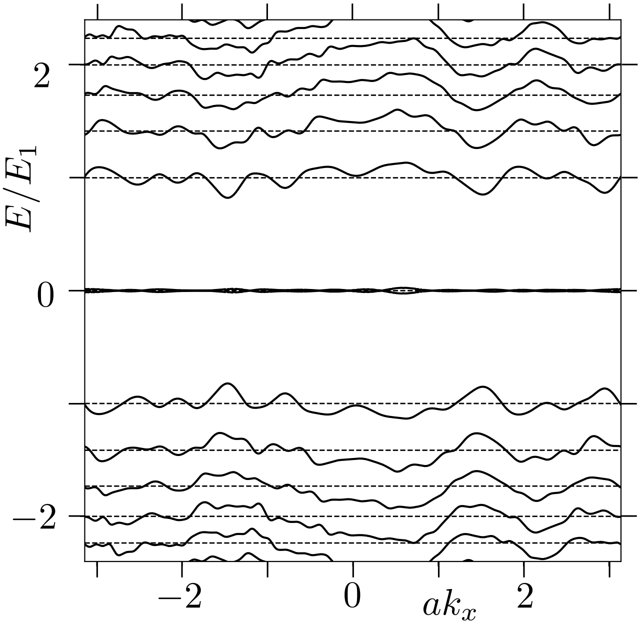

Figure 4.6: Same calculation as in Fig. 4.2, but now for a magnetic field that varies randomly in the y-direction. The zeroth Landau level contains states of opposite chirality which are not spatially separated, so they split in the presence of disorder.

and bottom surfaces in the slab geometry of Fig. 6.1 are unfolded onto a plane. The inward and outward pointing magnetic field then corresponds to adjoining $+B$ and $-B$ regions, each with a zeroth Landau level of opposite chirality.

From a methodological point of view our work provides a gauge invariant way to discretize the Dirac equation on a lattice without breaking chiral symmetry. We note that earlier attempts to achieve this were not succesful [53, 62]. The defining equation (4.10) of tangent fermions has the form of a generalized eigenvalue problem, $\mathcal{H}\Psi = E\mathcal{P}\Psi$, with local Hermitian operators $\mathcal{H}, \mathcal{P}$ on both sides of the equations — allowing for an efficient solution.

The alternative method of Wilson fermions works with a conventional eigenvalue problem, $H_{\text{Wilson}}\Psi = E\Psi$, that is local and gauge invariant, so it is certainly efficient. However, it breaks chiral symmetry, and it therefore lacks the topological protection of the zeroth Landau level.

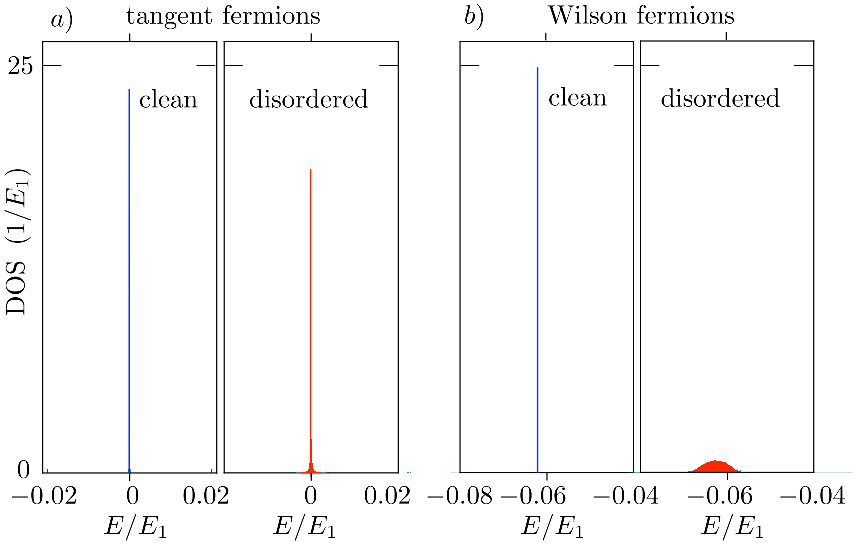

Figure 4.7: Density of states per unit cell for the tangent dispersion (a) and for the sine+cosine dispersion (b), with and without disorder in the magnetic field. (The disordered data is averaged over 1000 realizations.) The energy resolution is $2 \cdot 10^{-4}\, E_1$, so that a peak of height $25/E_1$ corresponds to a degeneracy of 1 state per 200 unit cells. Both panels refer to the same magnetic field $B_0 = (1/202)(h/ea^2)$, and the same disorder strength $B \in (0, 2B_0)$. The geometry of panel a) is the $\pm B_0$ field profile of Fig. 4.4 ($L_0 = 101\, a$), while panel b) is for a single square of dimensions $202\, a \times 202\, a$. In both cases we impose periodic boundary conditions in the x– and y–directions. The parameter Δ in the Wilson Hamiltonian (4.2) is set at $\hbar v/a$.

In the previous chapters and Ref. 63 we have established the topological protection of the Dirac cone of tangent fermions in zero magnetic field. The present chapter completes this line of investigation by showing how the topological protection can be extended to the zeroth Landau level in a magnetic field. Our computer codes and numerical data are available at a repository DOI:10.5281/zenodo.7495175.

CHAPTER 5

Chirality inversion of Majorana edge modes in a Fu-Kane heterostructure

5.1. Introduction

The chiral edge modes of the quantum Hall effect in a semiconductor have a superconducting analogue [28]: A two-dimensional (2D) superconductor with broken time-reversal symmetry and broken spin-rotation symmetry can enter a phase in which the gapped interior supports gapless edge excitations. This is called a topological superconductor, because the number of edge modes is set by a topological invariant [40, 86, 87]. Each edge mode contributes a quantized unit of thermal conductance, producing the thermal quantum Hall effect [88]. The edge modes are referred to as Majorana modes, since the quasiparticle excitations at the Fermi level are their own antiparticle — being equal-weight superpositions of electrons and holes.

Chiral edge modes have not yet been conclusively observed in a superconductor [89, 90], due in part to the complexity of heat transport measurements at low temperatures. In this work we propose an *electrical* signature of a chiral edge mode, triggered by the chirality inversion when a supercurrent flows along the boundary.

Our study was motivated by the recent experimental observation of the Doppler effect from a superflow in a topological superconductor [29]. The 2D electron gas of massless Dirac fermions on the surface of the topological insulator $\mathrm{Bi_2Te_3}$ is proximitized by the superconductor $\mathrm{NbSe_2}$, so that a gap Δ_0 opens up at the Fermi level μ. An in-plane magnetic field B induces a screening supercurrent over a London penetration depth λ_L, which boosts the Cooper pair momentum by an amount $K \simeq eB\lambda_\mathrm{L}$, in-plane and perpendicular to B. The Doppler effect [30, 91] shifts the quasiparticle energy by $\delta E = v_\mathrm{F}K$, closing the gap when K exceeds $K^* = \Delta_0/v_\mathrm{F}$ [92–94].

The ingredient we add to the system of Ref. 29 is the confinement produced by a magnetic insulator (EuS) with magnetization perpendicular to the surface layer (see Fig. 6.1). This is the Fu-Kane proposal [27] for chiral Majorana modes. Our key finding is that the superflow inverts the chirality of a Majorana mode moving in the opposite direction once K exceeds $K_c = K^*\Delta_0/\mu$ — so well before the gap closing transition for $\Delta_0 \ll \mu$. This chirality inversion can be detected in a transport experiment, both in thermal and in electrical conduction.

5.2. Chirality inversion

We base our analysis on the 2D Dirac-Bogoliubov-de Gennes Hamiltonian of a topological insulator surface (Fermi energy $\mu = v_\mathrm{F}k_\mathrm{F}$, $\hbar \equiv 1$) with induced s-wave superconductivity at Cooper pair momentum $\boldsymbol{K}$,

$$\mathcal{H} = \big(v_\mathrm{F}\boldsymbol{k}\cdot\boldsymbol{\sigma} - \mu\sigma_0\big)\tau_z + \big(v_\mathrm{F}\boldsymbol{K}\cdot\boldsymbol{\sigma} + M\sigma_z\big)\tau_0 + \Delta_0\sigma_0\tau_x. \tag{5.1}$$

The vectors $\boldsymbol{k}$, $\boldsymbol{\sigma}$, $\boldsymbol{K}$ have only x and y components, in the plane of the surface. The magnetization M points in the z-direction. The σ and τ Pauli matrices act, respectively, on spin and electron-hole degrees of freedom.[1]

We confine the electrons to a strip of width W parallel to the y-axis, by setting $M = 0$ for $|x| < W/2$ and $M \to +\infty$ for $|x| > W/2$. Integrating

$$-iv_\mathrm{F}\sigma_x\tau_z\partial_x\psi = -M\sigma_z\tau_0\psi \Rightarrow v_\mathrm{F}\partial_x\psi = -M\sigma_y\tau_z\psi \tag{5.2}$$

from $x = \pm W/2$ to $\pm\infty$, and demanding a decaying wave function, we

---

[1] The Hamiltonian (5.1) locks the spin in the direction of motion, via the term $k_x\sigma_x + k_y\sigma_y$. Rashba spin-orbit coupling would lock the spin in the perpendicular direction, via $k_x\sigma_y - k_y\sigma_x$. The two Hamiltonians are related by a unitary transformation, so we can choose one type of coupling without loss of generality. The σ_y-polarization of the Dirac edge mode that we find for the Hamiltonian (5.1) (with a boundary parallel to the y-axis) corresponds to a σ_x-polarization for the Rashba Hamiltonian.

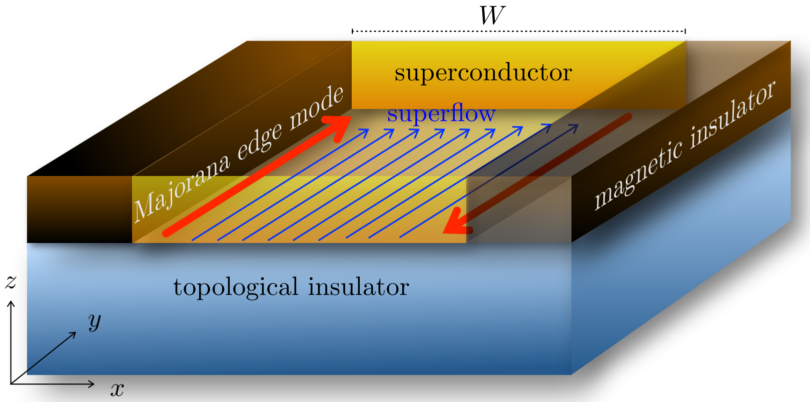

Figure 5.1: Schematic of the Fu-Kane heterostructure [27], a topological insulator with induced s-wave superconductivity (gap Δ_0, Fermi velocity $v_{\rm F}$, Fermi energy μ). The surface electrons are confined to a channel (width W) by a pair of magnetic insulators with perpendicular magnetization. Counterpropagating Majorana edge modes are indicated by red arrows. The blue arrows indicate the superflow (Cooper pair momentum K). The Doppler effect boosts the velocity of the Majorana mode on the left edge, while the right edge mode slows down and inverts its direction of motion when $K > \Delta_0^2/\mu v_{\rm F}$. At that chirality inversion a Dirac mode appears on the right edge, moving oppositely to the superflow.

obtain the boundary condition

$$\psi(x,y) = \pm\sigma_y\tau_z\psi(x,y) \ \text{ at } \ x = \pm W/2. \tag{5.3}$$

The spinor structure of the wave function at the boundaries is therefore a superposition of

$$|u_1\rangle = \begin{pmatrix} i \\ 1 \end{pmatrix} \otimes \begin{pmatrix} 1 \\ 0 \end{pmatrix}, \quad |u_2\rangle = \begin{pmatrix} -i \\ 1 \end{pmatrix} \otimes \begin{pmatrix} 0 \\ 1 \end{pmatrix} \tag{5.4}$$

at $x = -W/2$ and a superposition of $\tau_x|u_1\rangle$, $\tau_x|u_2\rangle$ at $x = W/2$.

We seek the wave function profile $\psi(x,y) = e^{ik_y y}\psi(x)$ at energy E and wave vector k_y parallel to the boundary. The superflow momentum $\boldsymbol{K} = (0, K)$ is oriented along the boundary. Integration of the Schrödinger equation $\mathcal{H}\psi = E\psi$ gives $\psi'(x) = \Omega\psi(x) \Rightarrow \psi(W/2) = e^{W\Omega}\psi(-W/2)$ with

$$\begin{aligned}\Omega = {}& i(E/v_{\rm F})\sigma_x\tau_z + i(\mu/v_{\rm F})\sigma_x\tau_0 - iK_x\sigma_0\tau_z + K\sigma_z\tau_z \\ & + k_y\sigma_z\tau_0 + (\Delta_0/v_{\rm F})\sigma_x\tau_y.\end{aligned} \tag{5.5}$$

The boundary condition (5.3) dictates that $\psi(-W/2)$ is a superposition of the states $|u_1\rangle$, $|u_2\rangle$, while $\psi(W/2)$ is orthogonal to these two states. This gives the determinantal equation

$$\det\Xi = 0,\quad \Xi_{nm} = \langle u_n|e^{W\Omega}|u_m\rangle, \tag{5.6}$$

from which we determine the spectrum $E(k_y)$. In the limit $W \to \infty$ of uncoupled edges we find near $k_y = 0$ the Majorana edge mode dispersion[2]

$$\begin{aligned}E_\pm &= \pm v_{\rm F}k_y\frac{\Delta_0^2 + v_{\rm F}^2K^2 \pm v_{\rm F}K\mu}{\Delta_0^2 \mp v_{\rm F}K\mu + \mu^2} \\ &\to v_{\rm F}k_y(K/k_{\rm F} \pm \Delta_0^2/\mu^2)\ \text{ for }\ \mu \gg \Delta_0.\end{aligned} \tag{5.7}$$

The ± sign distinguishes the modes on opposite edges. These are Majorana modes, because they are nondegenerate and transform into themselves when charge conjugation maps $E \mapsto -E$ and $k_y \mapsto -k_y$.

The group velocity of an edge mode equals dE/dk_y, and hence we conclude from Eq. (5.7) that a chirality inversion appears with increasing K, such that for $K > K_c$ both Majorana edge modes propagate in the same direction. This is illustrated in Fig. 5.2. The critical K_c equals

$$K_c = \frac{2\Delta_0^2/v_{\rm F}}{\sqrt{4\Delta_0^2 + \mu^2} + \mu} \to \frac{\Delta_0^2}{v_{\rm F}\mu}\ \text{ for }\ \mu \gg \Delta_0. \tag{5.8}$$

Since the gap in the bulk spectrum does not close until $K = K^* = \Delta_0/v_{\rm F}$ the bulk remains gapped in the inverted regime — only the edge modes propagate at the Fermi energy ($E = 0$).

For $K > K_c$ the inverted Majorana mode at $k_y = 0$ coexists with two counterpropagating modes at

$$\pm k_{\rm D} = \pm\sqrt{1 + k_{\rm F}/K}\sqrt{K^2 + Kk_{\rm F} - (\Delta_0/v_{\rm F})^2}. \tag{5.9}$$

Check that $k_{\rm D} = 0$ for $K = K_c$. At larger K the Dirac mode momentum $k_{\rm D}$ rises quickly to a value of order $k_{\rm F}$.

The Dirac fermions have charge expectation value $\pm\langle Q\rangle = \pm e\langle\tau_z\rangle$. Near

---

[2] Details of the calculation of the edge mode dispersion are given in App. 5.A.

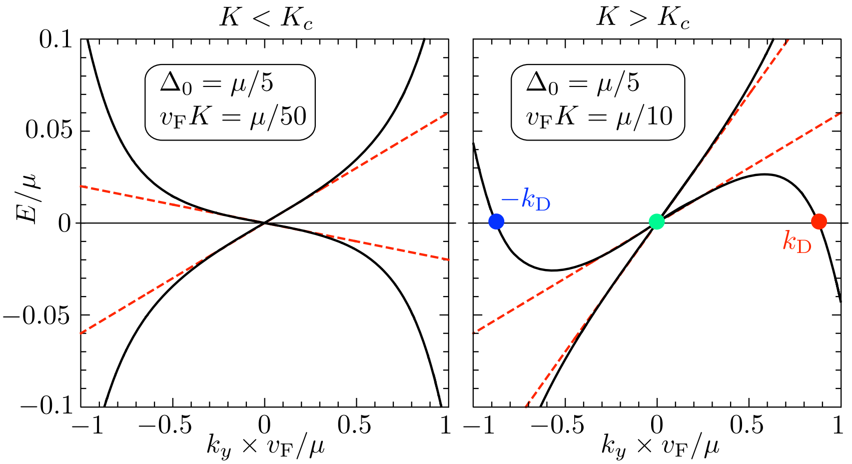

Figure 5.2: Dispersion relation of the edge modes in the non-inverted regime ($K < K_c$) and in the inverted regime ($K > K_c$). The solid curves are calculated numerically from Eq. (5.6) for channel width $W = 100\, v_F/\mu$. The dashed lines are the large-μ, large-W asymptotes (5.7). The colored dots in the inverted regime indicate the charge-neutral Majorana mode (at $k_y = 0$) and the electron-like and hole-like Dirac modes (at $k_y = \pm k_D$).

the transition we find[3]

$$\langle Q \rangle = e(\Delta_0/\mu)\sqrt{(K - K_c)/k_F}, \quad K \gtrsim K_c. \tag{5.10}$$

As shown in Fig. 5.3, the square-root singularity at $K = K_c$ crosses over into an approximately linear increase for larger K, up to $Q_{\max} = \frac{2}{3}e + \mathcal{O}(\Delta_0/\mu)$ at $K = K^*$.

We also show in Fig. 5.3 that the Dirac mode is approximately spin-polarized, with expectation value $\langle \sigma_y \rangle = \pm(1 - \Delta_0/6\mu)$ for $\mu \gg \Delta_0$ and K well above K_c. So the Dirac modes differ from the Majorana modes by their nonzero charge and spin expectation value, and there is one more difference: The decay length λ of the edge modes into the bulk is smaller for the Dirac modes ($\lambda_D \simeq v_F/\sqrt{\mu\Delta_0}$) than it is for the Majorana modes ($\lambda_M = v_F/\Delta_0$, the superconducting coherence length).

---

[3] Details of the calculation of the charge and spin of the Dirac mode are given in App. 5.B.

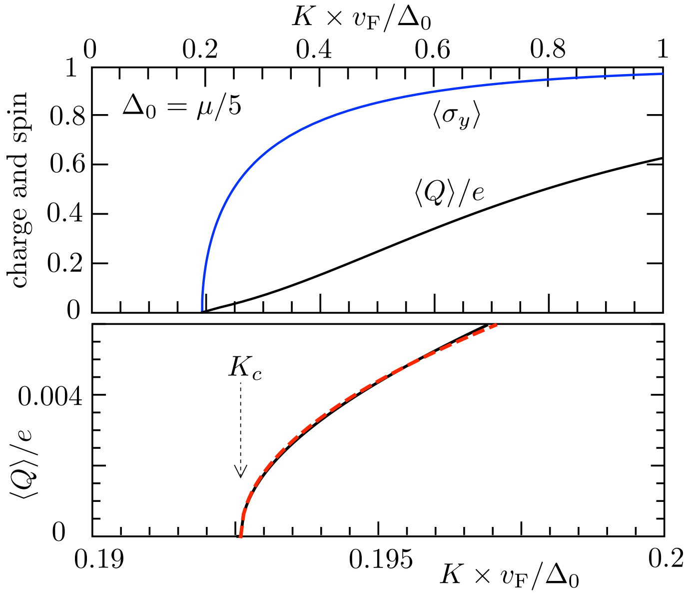

Figure 5.3: Top panel: Charge and spin expectation value of the Dirac fermions at $E = 0$ in the inverted regime. The solid curves are calculated (App. 5.B) in the limit $W \to \infty$. The lower panel shows a close-up of the charge for K close to K_c, the asymptote (5.10) is the dashed curve. The electron-like and hole-like Dirac fermions (red and blue dots in Fig. 5.2) have opposite signs of $\langle Q\rangle$ and $\langle\sigma_y\rangle$.

5.3. No chirality inversion in a *p*-wave superconductor

The Doppler effect of a supercurrent flowing along the boundary of a spinless chiral p-wave superconductor has been studied previously [95, 96] — without producing the chirality inversion we find for the Fu-Kane superconductor. To understand why, we have repeated our calculations for the Hamiltonian

$$\mathcal{H}_{p\text{-}wave} = \begin{pmatrix} (\boldsymbol{k}+\boldsymbol{K})^2/2m - \mu & (\Delta_0/k_F)(k_x + ik_y) \\ (\Delta_0/k_F)(k_x - ik_y) & \mu - (\boldsymbol{k}-\boldsymbol{K})^2/2m \end{pmatrix} \qquad (5.11)$$

of a 2D superconductor with a spinless chiral p-wave pair potential. Gapless edge modes coexist with a gapped bulk for $\mu = k_F^2/2m > 0$ and $K < K^* =$

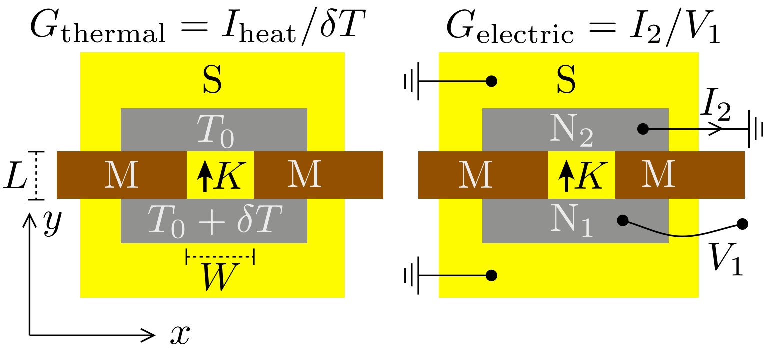

Figure 5.4: Top view of the proximitized topological insulator (S) of Fig. 5.1, with additional normal metal contacts (N_1, N_2) to measure the transport of heat (left panel) and the transport of charge (right panel) through a constriction of width W and length L, confined by magnetic insulators (M).

Δ_0/v_{F}.

As before, we take a channel of width W along the y-axis, parallel to the superflow momentum $\boldsymbol{K} = (0, K)$. For large W we find the edge mode dispersion[4]

$$E = (v_{\text{F}} k_y / k_{\text{F}})(K \pm \Delta_0 / v_{\text{F}}), \tag{5.12}$$

to first order in k_y and K. We see that there is no velocity inversion of the edge modes at any $K < K^*$ for which the bulk remains gapped. Comparison with the dispersion (5.7) in the Fu-Kane superconductor shows that it is the Δ_0 versus Δ_0^2 dependence that forms the obstruction to $K_c < K^*$ in a chiral p-wave superconductor.

5.4. Transport signatures

The chirality inversion of the edge modes in the Fu-Kane superconductor can be observed in both thermal and electrical conduction. The two transport geometries are shown in Fig. 5.4.

The thermal conductance G_{thermal} at temperature T_0 is given by the transmission matrix t (from contact N_1 to contact N_2),

$$G_{\text{thermal}} = G_0 \operatorname{Tr} t^\dagger t, \quad G_0 = \tfrac{1}{6}(\pi^2 k_{\text{B}}^2 / h) T_0. \tag{5.13}$$

---

[4] That the shift of $\boldsymbol{k}$ by the superflow momentum $\boldsymbol{K}$ appears only in the diagonal elements of the Hamiltonian (5.11) is required by gauge invariance, see App. 5.C, which also contains a derivation of Eq. (5.12).

The conductance quantum G_0 has 1/2 the value for normal electrons because of the Majorana nature of the carriers.

The electrical circuit is a three-terminal configuration, with a grounded superconductor in addition to the metal contacts N_1, N_2. The conductance $G_{\text{electric}} = I_2/V_1$, in the zero-temperature, zero-voltage limit, is given by[5]

$$G_{\text{electric}} = (e^2/h)\,\mathrm{Tr}\,(t_{ee}^\dagger t_{ee} - t_{he}^\dagger t_{he}) = \frac{e^2}{2h}\,\mathrm{Tr}\,\tau_z t^\dagger \tau_z t, \tag{5.14}$$

where t_{ee} and t_{he} are submatrices of t for transmission of an electron as an electron and as a hole, respectively.

For $K > K_c$ there are two right-moving edge modes and two left-moving edge modes at the Fermi energy, while for $K < K_c$ there is only a single left-mover and a single right-mover. The thermal conductance is therefore doubled when K becomes larger than K_c. For $K < K_c$ the counterpropagating Majorana edge modes carry no electrical charge, while for $K > K_c$ the two co-propagating modes on the same edge form a Dirac mode that can carry charge — but only in the direction opposite to the superflow.

To test these expectations we have carried out a numerical simulation of a tight-binding Hamiltonian.[6] We compared two models for the normal metal contact, with and without a large potential step at the normal-superconductor (NS) interface. For both models we assumed that the length L of the superconducting region is small compared to the mean free path for disorder scattering, so that any backscattering happens at the NS interfaces. Results are shown in Fig. 5.5.

The thermal conductance makes the transition from a completely flat plateau at G_0 for $K < K_c$ to a modulated plateau at $2G_0$ for larger K. Because of the appearance of counterpropagating modes on one of the edges the conductance is sensitive to backscattering for $K > K_c$, as is evident by the Fabry-Perot-type oscillations at the onset of the step (when the longitudinal momentum is small). After the onset the plateau is quite flat and close to the quantized value of $2G_0$.

The electrical conductance shows a striking asymmetry in K, it remains close to zero for $K > K_c$ and only switches on for $K < -K_c$. This asymmetry under exchange of N_1 and N_2 is not a violation of reciprocity,

---

[5] The second equality in Eq. (5.14) follows from the first by rewriting

$$G_{\text{electric}}/G_0 = (1/2)\,\mathrm{Tr}\,(1 + \tau_z)t^\dagger \tau_z t,$$

and then using particle-hole symmetry to identify $\mathrm{Tr}\, t^\dagger \tau_z t = 0$.

[6] Details of the tight-binding simulation are given in App. 5.D. We used the *Kwant* package [97].

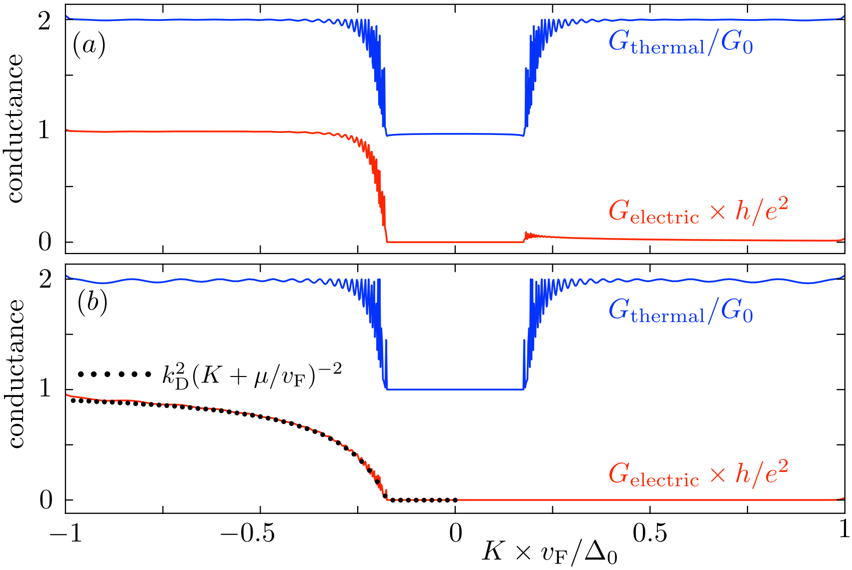

Figure 5.5: Results for the thermal and electrical conductance, obtained by the numerical simulation (App. 5.D) of a tight-binding model of the Fu-Kane superconductor ($\mu = 12\,\Delta_0$, $W = L = 1200\,v_F/\mu$). In panel (a) the chemical potential μ_N in the normal-metal contacts is equal to the value μ in the superconducting region, while panel (b) is for the case $\mu_N \gg \mu$. The transition starts at a superflow momentum K that is larger than the value $K_c = 0.08\,v_F/\Delta_0$ from Eq. (5.8), because of the finite lattice spacing ($k_F a_0 = 0.2$). The data points in panel (b) give the analytical result (5.15), with k_D from the simulation.

since it appears in a three-terminal configuration. The conductance rises to e^2/h in a step-like manner or more slowly, depending on whether or not there is a potential step at the interface.

The reason that the electrical conductance is sensitive to the details of the NS interface, while the thermal conductance is not, is that the heat current from contact N_1 to contact N_2 is conserved while the charge current is not. (Charge can be drained into the grounded superconducting terminal, but the gapped superconductor cannot absorb heat.)

In the absence of a potential step the simulation shows a conductance plateau at $G_{\text{electric}} \approx e^2/h$, indicating that a Dirac fermion at $k_D \approx k_F$ approaching the NS interface transfers a charge e — notwithstanding its charge expectation value $\langle Q \rangle < e$. We explain this by noting that for $\mu_N = \mu$ the longitudinal momentum is approximately conserved across the interface, coupling to states at $-k_{\mathrm{F}}$ is suppressed, and since the only outgoing states near k_{F} in the normal region are electrons, the bare charge e is transferred.

In the presence of a large potential step the longitudinal momentum is not conserved, it is boosted to $+k_{\mathrm{F}}$ for the electron component and to $-k_{\mathrm{F}}$ for the hole component of the Dirac mode. A mode matching calculation in the limit $\mu_{\mathrm{N}}/\mu \to \infty$ (see App. 5.E) gives

$$G_{\text{electric}} = \frac{e^2}{h} \frac{k_{\mathrm{D}}^2}{(K + \mu/v_{\mathrm{F}})^2} = \frac{e^2}{h} \left(1 - \frac{(\Delta_0/v_{\mathrm{F}})^2}{K(K + \mu/v_{\mathrm{F}})} \right), \tag{5.15}$$

in excellent agreement with the simulation.

Eq. (5.15) can be interpreted in terms of an effective transferred charge, $G_{\text{electric}} = (e^*)^2/h$ with $e^* = ek_{\mathrm{D}}/(K + k_{\mathrm{F}})$, but e^* is very different from $\langle Q \rangle$: While the charge expectation value $\langle Q \rangle$ increases approximately linearly from 0 to $\frac{2}{3}e$ as K increases from K_c to K^* (see Fig. 5.3), the effective transferred charge e^* increases much more rapidly from 0 all the way to e. We note that in a different charge transfer problem [98], in a Weyl superconductor, the identification of e^* and $\langle Q \rangle$ did hold.

5.5. Conclusion

In summary, we have reported on a manifestation of the Doppler effect from a supercurrent in a spinful topological superconductor: A supercurrent flowing along the magnetic boundary of a Fu-Kane superconductor can reverse the chirality of the Majorana edge mode, without closing the bulk gap. The chirality inversion is accompanied by the appearance of a Dirac mode that propagates counter to the superflow, such that the net number of right-movers minus left-movers is unchanged.

The effect is absent in a spinless chiral p-wave superconductor,[7] which is remarkable because the low-energy effective Hamiltonian in the bulk of the Fu-Kane superconductor has $p_x + ip_y$-wave pairing symmetry [27]. We have traced the origin of the difference to the linear versus quadratic dependence of the Majorana edge mode velocity on the bulk gap. It is the quadratic dependence that allows the superflow to restructure the edge modes without affecting the bulk spectrum.

The chirality inversion produces a fully electrical signature of the edge

---

[7] An apparently unrelated difference in the edge mode spectrum between spinless and spinful topological superconductors has been reported by A. Yamakage, Y. Tanaka, and N. Nagaosa in [99].

currents: charge can be transported upstream relative to the superflow, but not downstream — because a Majorana mode transports no charge while a Dirac mode does. Such a distinctive effect should help the conclusive observation of chiral Majorana fermions in a topological superconductor.

5.A. Calculation of the dispersion relation

The determinantal equation (5.6), with the 4 × 4 matrix Ω given by Eq. (5.5), is suitable for a numerical calculation of the dispersion relation $E(k_y)$ for finite W. Analytical expressions can be obtained in the limit $W \to \infty$ of uncoupled edges. In this appendix and the next one we set v_F to unity, for ease of notation.

The elements of the transfer matrix $e^{W\Omega}$ have an exponential dependence $\propto e^{W\xi_\pm}$ and $\propto e^{-W\xi_\pm}$ on W, with

$$\xi_\pm = \sqrt{\Delta_0^2 - E^2 - \mu^2 + k_y^2 + K^2 \pm 2\sqrt{\Delta_0^2\,(K^2-\mu^2) + (k_yK - E\mu)^2}}. \tag{5.16}$$

The sign ambiguity in the square roots is resolved by taking the square root with a positive real part (branch cut along the negative real axis). The edge modes in the limit $W \to \infty$ are obtained by setting $e^{-W\xi_\pm} \to 0$ in the transfer matrix. The determinantal equation (5.6) then reduces to

$$\begin{aligned}\Delta_0^2(K^2-\mu^2)(E^2-k_y^2-K^2+\mu^2)\\ + (\Delta_0^2 - \xi_-\xi_+)\left(\Delta_0^2(K^2-\mu^2) + 2(k_yK-E\mu)^2\right) = 0.\end{aligned} \tag{5.17}$$

We eliminate the square roots in the product $\xi_-\xi_+$ by rearranging the equation as $\xi_-\xi_+ = \cdots$ and then squaring both sides, resulting in

$$\begin{aligned}&\left(\Delta_0^2 - (E-K)^2 + (k_y-\mu)^2\right)\left(\Delta_0^2 - (E+K)^2 + (k_y+\mu)^2\right) =\\ &= \Delta_0^4\left(1 + \frac{(K^2-\mu^2)(E^2-k_y^2-K^2+\mu^2)}{\Delta_0^2(K^2-\mu^2) + 2(k_yK-E\mu)^2}\right)^2.\end{aligned} \tag{5.18}$$

Eq. (5.18) has eight solutions for E, the two physical solutions are the dispersions $E_\pm(k_y)$ that cross zero at $k_y = 0$. The full expressions are a bit lengthy and not recorded here. The linear dispersion near $k_y = 0$ does have a compact expression, given by Eq. (5.7) in the main text. Eq. (5.8) for K_c is the value of K at which the slope of $E_-(k_y)$ vanishes. To find the momenta $k_y = \pm k_\mathrm{D}$ of the Dirac modes for $K > K_c$ we solve Eq. (5.18) for k_y at $E = 0$, resulting in Eq. (5.9).

5.B. Calculation of the charge and spin of the Dirac mode

The charge expectation value $\langle Q \rangle = e\langle \tau_z \rangle$ can be obtained from the dispersion relation via the derivative $\langle Q \rangle = -e\partial E/\partial\mu$. It vanishes for the Majorana fermions at $k_y = 0$, but it is nonzero for the Dirac fermions at $k_y = \pm k_\mathrm{D}$, with $E(k_\mathrm{D}) = 0$. We can compute this directly from the determinantal equation (5.18), by substituting $E \mapsto E(\mu)$, differentiating with respect to μ, solving for $E'(\mu)$, and finally setting $E(\mu) \mapsto 0$, $k_y \mapsto k_\mathrm{D}$.

We thus arrive at the Dirac fermion charge

$$\langle Q \rangle = e\frac{\sqrt{K}\sqrt{K(K+\mu)-\Delta_0^2}\left(2K(K+\mu)-\Delta_0^2\right)}{\sqrt{K+\mu}\,[\Delta_0^2(\mu-K)+2K^2(K+\mu)]}. \tag{5.19}$$

This is the black curve plotted in the top panel of Fig. 5.3. Expansion near $K = K_c$ gives for $\mu \gg \Delta_0$ the square-root result (5.10) in the main text. The charge increases monotonically with increasing K, reaching its maximal value

$$Q_\mathrm{max} = e\sqrt{\frac{\mu}{\Delta_0+\mu}\,\frac{\Delta_0+2\mu}{\Delta_0+3\mu}} \tag{5.20}$$

at $K = K^* = \Delta_0$.

In a similar way we can calculate the spin expectation value $\langle \sigma_y \rangle = \partial E/\partial K$ of the Dirac fermions, with the result

$$\langle \sigma_y \rangle = \frac{\sqrt{K(K+\mu)-\Delta_0^2}\left(2K^2(K+\mu)+\Delta_0^2\mu\right)}{\sqrt{K(K+\mu)}\,[\Delta_0^2(\mu-K)+2K^2(K+\mu)]}, \tag{5.21}$$

see the blue curve in Fig. 5.3. The behavior for $K \gtrsim K_c$ is again a square root increase, $\langle \sigma_y \rangle \approx (\sqrt{\mu}/\Delta_0)\sqrt{K-K_c}$, rising rapidly to a value

$$\langle \sigma_y \rangle_\mathrm{max} = \sqrt{\frac{\mu}{\Delta_0+\mu}\,\frac{2\Delta_0+3\mu}{\Delta_0+3\mu}} \to 1 - \frac{\Delta_0}{6\mu} \quad \text{for} \quad \mu \gg \Delta_0, \tag{5.22}$$

close to unity.

The signs of spin and charge are such that $\langle Q \rangle < 0$ and $\langle \sigma_y \rangle > 0$ for the Dirac mode at $k_y = k_\mathrm{D}$. The mode at $k_y = -k_\mathrm{D}$ has the opposite signs.

5.C. Doppler-boosted edge modes in a chiral p-wave superconductor

The chiral p-wave Hamiltonian has the form

$$\mathcal{H}_{\text{p-wave}} = \begin{pmatrix} H_0 & \hat{\Delta} \\ \hat{\Delta}^\dagger & -H_0^* \end{pmatrix}, \tag{5.23a}$$

$$H_0 = \frac{1}{2m}(k_x^2 + k_y^2) - \mu, \tag{5.23b}$$

$$\hat{\Delta} = k_{\text{F}}^{-1}\{\Delta(\boldsymbol{r}), k_x + ik_y\}, \tag{5.23c}$$

with $\boldsymbol{k} = -i\partial/\partial\boldsymbol{r}$ and $\{a,b\} = \frac{1}{2}(ab+ba)$ the symmetrization operator.

The superflow momentum $\boldsymbol{K}$ enters in the pair potential via $\Delta(\boldsymbol{r}) = \Delta_0 e^{2i\boldsymbol{K}\cdot\boldsymbol{r}}$. We remove it by a gauge transformation,

$$\mathcal{H}_{\text{p-wave}} \mapsto U^\dagger H_{\text{p-wave}} U, \;\; U = \begin{pmatrix} e^{i\boldsymbol{K}\cdot\boldsymbol{r}} & 0 \\ 0 & e^{-i\boldsymbol{K}\cdot\boldsymbol{r}} \end{pmatrix}. \tag{5.24}$$

In view of the identity

$$e^{-i\boldsymbol{K}\cdot\boldsymbol{r}}\{e^{i\boldsymbol{K}\cdot\boldsymbol{r}}, \partial_x + i\partial_y\}e^{-i\boldsymbol{K}\cdot\boldsymbol{r}} = \partial_x + i\partial_y, \tag{5.25}$$

the transformed Hamiltonian (5.11) contains the Doppler shifted momentum only in the diagonal elements, not in the off-diagonal elements.

In terms of the Pauli matrices τ_α acting on the electron-hole degree of freedom, we have

$$\mathcal{H}_{\text{p-wave}} = \frac{k^2}{2m}\tau_z - \mu\tau_z + \frac{K}{m}k_y\tau_0 + \frac{\Delta_0}{k_{\text{F}}}(k_x\tau_x - k_y\tau_y), \tag{5.26}$$

to first order in $\boldsymbol{K} = (0, K)$. We introduce a boundary at $x = 0$ and seek the velocity of an edge mode in the y-direction. The velocity operator at $k_y = 0$ is

$$\hat{v}_{\text{edge}} = \lim_{k_y \to 0} \frac{\partial}{\partial k_y}\mathcal{H}_{\text{p-wave}} = \frac{K}{m}\tau_0 - \frac{\Delta_0}{k_{\text{F}}}\tau_y. \tag{5.27}$$

The edge mode wave function at $E = 0$, $k_y = 0$ solves

$$\frac{1}{2m}\psi''(x) + \mu\psi(x) - \frac{\Delta_0}{k_{\text{F}}}\tau_y\psi'(x) = 0, \tag{5.28}$$

for $x > 0$, with boundary condition $\psi(0) = 0$. A normalizable solution exists for $\mu > 0$, it is an eigenstate of τ_y with eigenvalue -1. The expectation value $v_{\rm edge}$ of the velocity follows directly,

$$v_{\rm edge} = \langle\psi|\hat{v}_{\rm edge}|\psi\rangle = K/m + \Delta_0/k_{\rm F}. \tag{5.29}$$

At the opposite edge the solution ψ is an eigenstate of τ_y with eigenvalue $+1$, resulting in a velocity $v_{\rm edge} = K/m - \Delta_0/k_{\rm F}$. The corresponding edge mode dispersion is given by Eq. (5.12).

5.D. Details of the tight-binding simulation

For the numerical calculations we model the Fu-Kane superconductor by a tight-binding Hamiltonian on a 2D square lattice (lattice constant a_0),

$$\begin{aligned}\mathcal{H} = {}& \frac{v_{\rm F}}{a_0}\sum_{\alpha=x,y}\sin(a_0k_\alpha + a_0K_\alpha)\sigma_\alpha\tau_z \\ &+ M\sigma_z\tau_0 - \mu\sigma_0\tau_z + \Delta_0\sigma_0\tau_x \\ &+ \frac{M_0v_{\rm F}}{a_0}\sum_{\alpha=x,y}[1-\cos(a_0k_\alpha + a_0K_\alpha)]\sigma_z\tau_0. \end{aligned}\tag{5.30}$$

In the limit $a_0 \to 0$ the continuum Hamiltonian (5.1) is recovered. The term $\propto M_0$ is introduced to avoid spurious Dirac points at the edge of the Brillouin zone (fermion doubling).

We consider a channel geometry of width W along the y-axis, with mass $M = 0$ for $|x| \leq W/2$ and infinite mass $M \to \infty$ for $|x| > W/2$. It is efficient if we can replace the infinite-mass term by a lattice termination at $|x| = W/2$, so that we only have to consider the lattice points inside the channel. This is allowed if the lattice termination enforces the boundary condition (5.3). We can set $M_0 = -1$ to achieve that goal.

To see this, consider the matrix elements for hopping in the $\pm x$-direction,

$$\mathcal{H}_{n_x\pm1,n_x} = \pm\frac{v_{\rm F}}{2ia_0}e^{\pm ia_0K_x}\sigma_x\tau_z - \frac{M_0v_{\rm F}}{2a_0}e^{\pm ia_0K_x}\sigma_z\tau_0. \tag{5.31}$$

To represent the boundary condition (5.3) by a lattice termination at the right edge, we need to ensure that $\mathcal{H}_{n_x-1,n_x}\psi = 0$ at $x = W/2 + a_0$ when $\psi = +\sigma_y\tau_z\psi$. Similarly, for $x = -W/2$ we need $\mathcal{H}_{n_x+1,n_x}\psi = 0$ at $x = -W/2 - a_0$ when $\psi = -\sigma_y\tau_z\psi$. One readily checks that both conditions are realized if $M_0 = -1$.

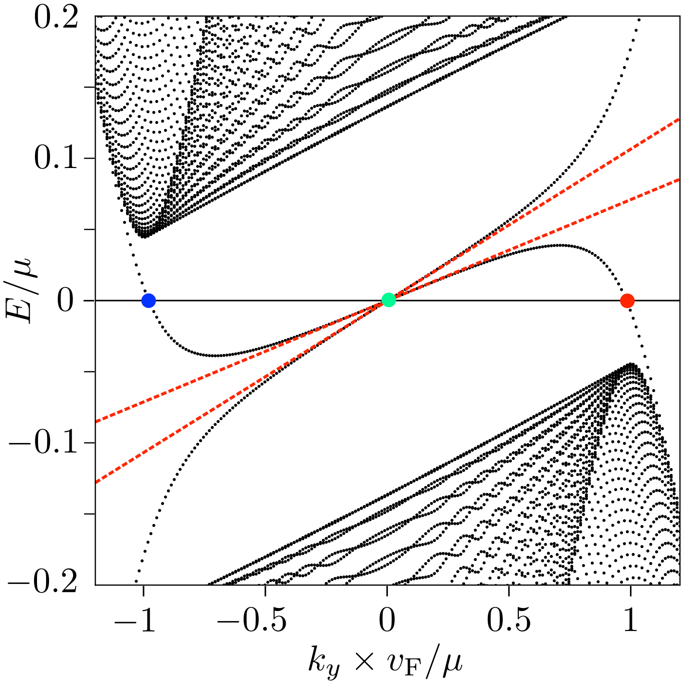

Figure 5.6: Energy spectrum of the superconducting channel, calculated numerically from the tight-binding Hamiltonian (5.30) ($\mu = 7.5\,\Delta_0$, $W = 100\,v_{\mathrm{F}}/\mu$, $K = \frac{2}{3}\Delta_0/v_{\mathrm{F}}$, $a_0 = 0.02\,v_{\mathrm{F}}/\mu$). The red dashed lines are the large-μ, large-W asymptotes (5.7) of the Majorana edge mode dispersion. The red and blue dots indicate the Dirac fermion mode at $k_y = \pm k_{\mathrm{D}}$, the green dot is the Majorana fermion at $k_y = 0$.

In Figs. 5.6 and 5.7 we show that we recover the analytical results for the edge mode dispersion and for the expectation value of the charge and spin of the Dirac fermions. To achieve this accurate agreement the tight-binding model needs to be close to the continuum limit. For that purpose we took a small lattice contant ($k_{\mathrm{F}}a_0 = 0.02$), which is computationally feasible in an effectively 1D simulation. The transport calculations are fully 2D and we were forced to take a ten times larger lattice constant to keep the problem tractable. This is why the numerical value of K_c in Fig. 5.5 differs substantially from the analytical result in the continuum limit.

For the transport calculations we take a finite length L of the superconducting segment (S), and attach semi-infinite normal metal leads (N) at

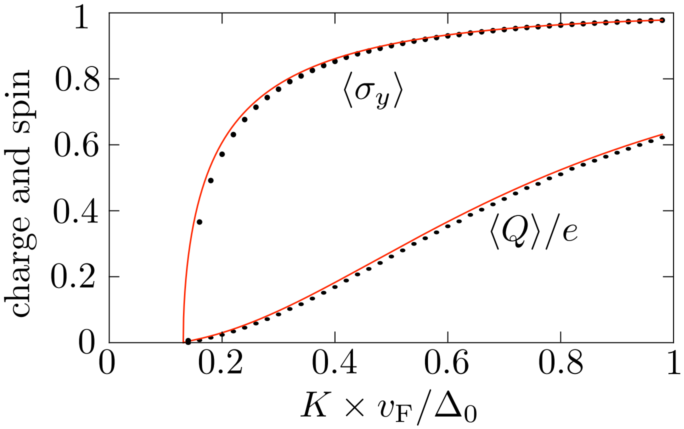

Figure 5.7: Expectation value of the charge and the spin of the Dirac fermions in the inverted regime, as a function of the superflow momentum K. The data points result from the tight-binding simulation (same parameters as in Fig. 5.6), the solid curves are the analytical results (5.19) and (5.21) in the limit $W \to \infty$.

the two ends (see Fig. 5.8). We set $\Delta_0 = 0$ in N, no coupling of electrons and holes (the value of K then becomes irrelevant and may be set to zero),

$$\mathcal{H}_{\mathrm{lead}} = \frac{v_{\mathrm{F}}}{a_0} \sum_{\alpha=x,y} \sigma_\alpha \tau_z \sin a_0 k_\alpha - \mu \sigma_0 \tau_z + \frac{M_0 v_{\mathrm{F}}}{a_0} \sum_{\alpha=x,y} (1 - \cos a_0 k_\alpha) \sigma_z \tau_0. \tag{5.32}$$

We again set $M_0 = -1$ to implement the infinite-mass boundary condition by a lattice termination at $x = \pm W/2$.

Eq. (5.32) is the model without a potential step at the NS interface (panel *a* in Fig. 5.5). If the chemical potential μ_{N} in the normal metal leads is much larger than the value μ in the superconducting region, only modes with a large longitudinal momentum k_y are transmitted across the NS interface. We cannot directly take the large-μ_{N} limit in the Hamiltonian (5.32), because of the finite band width. Instead, we achieve the same goal of suppressing transverse momenta by cutting the transverse hoppings at

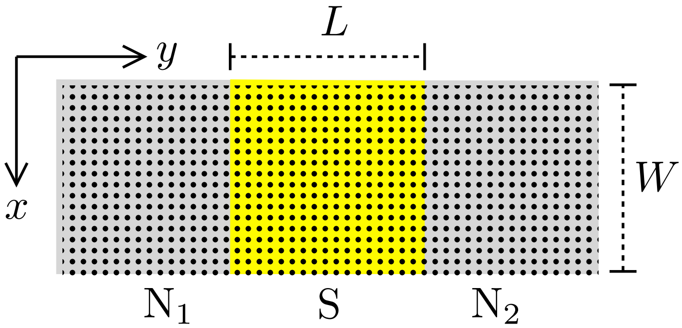

Figure 5.8: Two-dimensional square lattice on which the tight-binding model is defined. The Hamiltonian (5.30) is applied to the superconducting segment of length L (yellow). In the semi-infinite leads (grey) the Hamiltonian is given by Eqs. (5.33) and (5.32), respectively, in the models with and without a potential step at the NS interfaces.

$\mu_{\mathrm{N}} = 0$,

$$\begin{aligned}\mathcal{H}_{\text{lead}}(\text{large potential step}) = {} & \frac{v_{\mathrm{F}}}{a_0}\sigma_y\tau_z \sin a_0 k_y \\ & + \frac{M_0 v_{\mathrm{F}}}{a_0}(1-\cos a_0 k_y)\sigma_z\tau_0. \end{aligned} \tag{5.33}$$

This produces the data in panel *b* of Fig. 5.5.

5.E. Derivation of Eq. (5.15)

5.E.1. Calculation of the transferred charge

We seek to compute the charge e^* transferred across the NS interface at $y = 0$ by a Dirac fermion at $k_y = \pm k_{\mathrm{D}}$. We assume a large potential step at the interface, such that the chemical potential μ_{N} in the normal region $y < 0$ is much larger than the value $\mu = v_{\mathrm{F}} k_{\mathrm{F}}$ in the superconducting region $y > 0$. The Hamiltonian in S is

$$\begin{aligned}\mathcal{H} &= v_{\mathrm{F}}(k_x\sigma_x + k_y\sigma_y)\tau_z + v_{\mathrm{F}} K\sigma_y\tau_0 - \mu\sigma_0\tau_z \\ &\quad + M\sigma_z\tau_0 + \Delta_0\sigma_0\tau_x \\ &\equiv H_0 + v_{\mathrm{F}} k_y\sigma_y\tau_z. \end{aligned} \tag{5.34}$$

For later use we have separated out the k_y-independent part $H_0 = \lim_{k_y\rightarrow 0}\mathcal{H}$.

The potential step boosts the momentum component k_y perpendicular to the interface, without affecting the parallel component k_x, so in N only modes are excited with $|k_y| \gg |k_x|$. These are eigenstates of $\sigma_y\tau_z$ with eigenvalue -1, moving away from the interface in the $-y$ direction. Continuity of the wave function Ψ at the interface then requires that $\lim_{y\rightarrow 0}\Psi \equiv \Psi_0$ satisfies

$$\sigma_y\tau_z\Psi_0 = -\Psi_0 \Leftrightarrow \mathcal{P}\Psi_0 = \Psi_0, \tag{5.35}$$

with projection operator

$$\mathcal{P} = \tfrac{1}{2}(1 - \sigma_y\tau_z). \tag{5.36}$$

The eigenvalue equation $\mathcal{H}\Psi = 0$ at $E = 0$ implies that

$$\begin{aligned} 0 &= \lim_{y\downarrow 0}\mathcal{P}\mathcal{H}\Psi = \mathcal{P}H_0\mathcal{P}\Psi_0 + \lim_{y\downarrow 0}\mathcal{P}v_{\rm F}k_y\sigma_y\tau_z\Psi \\ &= (K + k_{\rm F})\mathcal{P}\hat{\jmath}\mathcal{P}\Psi_0 - i\mathcal{P}\hat{v}\Psi_0', \end{aligned} \tag{5.37}$$

with the definitions $\hat{\jmath} = v_{\rm F}\sigma_y\tau_0$, $\hat{v} = v_{\rm F}\sigma_y\tau_z$, and $\Psi_0' = \lim_{y\downarrow 0}\partial\Psi/\partial y$. The derivative is not continuous at the NS interface, hence the specification that the limit $y \downarrow 0$ should be taken from above. Also note that $\mathcal{P}\Psi_0 = \Psi_0$ but $\mathcal{P}\Psi_0' \neq \Psi_0'$.

We define the y-dependent inner product of two arbitrary states,

$$\langle\Psi_1|\Psi_2\rangle_y = \int dx\, \Psi_1^*(x,y)\Psi_2(x,y). \tag{5.38}$$

With respect to this inner product the operator H_0 is self-conjugate, $\langle\Psi_1|H_0\Psi_2\rangle_y = \langle H_0\Psi_1|\Psi_2\rangle_y$, but the operator $k_y = -i\partial/\partial y$ is not (an integration over y would be needed for that). Still, if Ψ is an eigenstate of $\mathcal{H}$ at eigenvalue E, we have $k_y\hat{v}\Psi = (E - H_0)\Psi$, so $k_y\hat{v}$ inherits the self-conjugate property from H_0, $\langle\Psi|k_y\hat{v}\Psi\rangle_y = \langle k_y\hat{v}\Psi|\Psi\rangle_y$.

We will use this identity in the two forms

$$\langle\Psi|\hat{v}|\Psi'\rangle_y = -\langle\Psi'|\hat{v}|\Psi\rangle_y,\;\; \langle\Psi'|\hat{v}|\Psi'\rangle_y = -\langle\Psi|\hat{v}|\Psi''\rangle_y, \tag{5.39}$$

where $\Psi' = \partial\Psi/\partial y$ and $\Psi'' = \partial^2\Psi/\partial y^2$. (The second equality holds because $\mathcal{H}$ does not depend on y, so if $\mathcal{H}\Psi = E\Psi$ then also $\mathcal{H}\Psi' = E\Psi'$.)

One implication of Eq. (5.39) is that the particle current $\langle\Psi|\hat{v}|\Psi\rangle_y$ is

y-independent, as it should be,

$$\frac{d}{dy}\langle\Psi|\hat{v}|\Psi\rangle_y = \langle\Psi'|\hat{v}|\Psi\rangle_y + \langle\Psi|\hat{v}|\Psi'\rangle_y = 0. \tag{5.40}$$

A more unexpected implication is that also the expectation value $\langle\Psi|\hat{v}|\Psi'\rangle_y$ is y-independent,

$$\frac{d}{dy}\langle\Psi|\hat{v}|\Psi'\rangle_y = \langle\Psi'|\hat{v}|\Psi'\rangle_y + \langle\Psi|\hat{v}|\Psi''\rangle_y = 0. \tag{5.41}$$

We will make essential use of these two properties in just a moment.

The charge current I_{charge} through the NS interface at $y = 0$,

$$I_{\text{charge}} = e\langle\Psi|\hat{j}|\Psi\rangle_0 = e\langle\Psi|\mathcal{P}\hat{j}\mathcal{P}|\Psi\rangle_0, \tag{5.42}$$

can be rewritten by substitution of Eq. (5.37),

$$I_{\text{charge}} = \frac{ie}{K+k_{\text{F}}}\langle\Psi|\mathcal{P}\hat{v}|\Psi'\rangle_0 = \frac{ie}{K+k_{\text{F}}}\langle\Psi|\hat{v}|\Psi'\rangle_0. \tag{5.43}$$

The renormalized charge e^* transferred through the NS interface by a Dirac fermion is the ratio of the charge current and the particle current $I_{\text{particle}} = \langle\Psi|\hat{v}|\Psi\rangle_0$,

$$e^* = \frac{ie}{K+k_{\text{F}}}\frac{\langle\Psi|\hat{v}|\Psi'\rangle_0}{\langle\Psi|\hat{v}|\Psi\rangle_0} = \frac{ie}{K+k_{\text{F}}}\frac{\langle\Psi|\hat{v}|\Psi'\rangle_y}{\langle\Psi|\hat{v}|\Psi\rangle_y}. \tag{5.44}$$

In the second equality we used Eqs. (5.40) and (5.41).

We can evaluate the ratio of y-dependent expectation values at large y, far from the interface, where evanescent waves have decayed to zero and Ψ contains only the propagating Dirac mode $\Psi_{\text{D}} \propto e^{\pm ik_{\text{D}}y}$ — under the assumption that there is no backscattering of quasiparticles at the interface. The ratio then reduces to $\pm ik_{\text{D}}$, resulting in a transferred charge

$$\pm e^* = \pm\frac{ek_{\text{D}}}{K+k_{\text{F}}}. \tag{5.45}$$

The sign of the transferred charge is set by the sign of the charge expectation value $\langle Q\rangle$ of the Dirac mode, but the magnitude is different.

Eq. (5.45) gives the charge of an outgoing mode in N (moving away from the NS interface), when it is matched to an incoming Dirac mode in S (moving towards the NS interface). The entire calculation carries over if the direction of motion is inverted, so when an incoming mode in N is matched to an outgoing Dirac mode in S, the incoming mode has the same charge $\pm e^*$.

5.E.2. Calculation of the electrical conductance

The transferred charge determines the conductance $G_{\text{electric}} = I_2/V_1$ that gives the electrical current I_2 into the normal contact N_2 in response to a voltage V_1 applied to contact N_1 (see Fig. 5.8). This is a three-terminal circuit, the third terminal is the grounded superconductor S connecting N_1 and N_2, separated by a distance L. We assume that both contacts have a chemical potential $\mu_{\mathrm{N}} \gg \mu$.

In the absence of backscattering the transmission matrix t from N_1 to N_2 is a rank-two matrix of the form

$$t = e^{ik_{\mathrm{D}}L}|\Psi_2^+\rangle\langle\Psi_1^+| + e^{-ik_{\mathrm{D}}L}|\Psi_2^-\rangle\langle\Psi_1^-|. \tag{5.46}$$

The incoming mode $|\Psi_1^\pm\rangle$ in contact N_1 is matched in S to a Dirac mode at $k_y = \pm k_{\mathrm{D}}$. The Dirac mode propagates to contact N_2, picking up a phase $e^{\pm ik_{\mathrm{D}}L}$, and is then matched to an outgoing mode $|\Psi_2^\pm\rangle$. The matching condition gives a charge $\pm e^*$ to $\Psi_n^\pm$,

$$\langle\Psi_n^\pm|\tau_z|\Psi_n^\pm\rangle = \pm e^*. \tag{5.47}$$

The modes $|\Psi_n^+\rangle$ and $|\Psi_n^-\rangle$ not only carry opposite charge, they are each others particle-hole conjugate,

$$|\Psi_n^+\rangle = \sigma_y\tau_y|\Psi_n^-\rangle^*, \tag{5.48}$$

as they are matched to Dirac modes that are related by particle-hole conjugation. We will use an orthogonality consequence of this property:

$$\begin{aligned}\langle\Psi_n^+|\tau_z|\Psi_n^-\rangle &= -\langle\Psi_n^+|\sigma_y\tau_y\tau_z\sigma_y\tau_y|\Psi_n^-\rangle = -\langle\Psi_n^-|\tau_z|\Psi_n^+\rangle^* \\ &= -\langle\Psi_n^+|\tau_z|\Psi_n^-\rangle \Rightarrow \langle\Psi_n^+|\tau_z|\Psi_n^-\rangle = 0.\end{aligned} \tag{5.49}$$

So while current conservation by itself requires that $|\Psi_n^+\rangle$ is orthogonal to $|\Psi_n^-\rangle$, the additional constraint of particle-hole symmetry also gives the orthogonality of $|\Psi_n^+\rangle$ and $\tau_z|\Psi_n^-\rangle$.

We now have all the pieces in place to calculate the conductance, given in terms of the transmission matrix by

$$G_{\mathrm{electric}} = \frac{e^2}{2h} \operatorname{Tr} \tau_z t^\dagger \tau_z t. \tag{5.50}$$

Substitution of Eq. (5.46) and use of the orthogonality (5.49) gives

$$G_{\mathrm{electric}} = \frac{e^2}{2h} \sum_{s=\pm} \langle \Psi_2^s | \tau_z | \Psi_2^s \rangle \langle \Psi_1^s | \tau_z | \Psi_1^s \rangle = \frac{(e^*)^2}{h}, \tag{5.51}$$

where in the second equality we used Eq. (5.47). Subsitution of Eq. (5.45) then produces Eq. (5.15) in the main text.

CHAPTER 6

Dynamical simulation of the injection of vortices into a Majorana edge mode

6.1. Introduction

A remarkable property of topological superconductors is that two vortices winding around each other exchange a quasiparticle [36, 88, 100]. This "braiding" operation is a manifestation of the non-Abelian statistics of the Majorana zero-modes bound to the core of an Abrikosov vortex [101–103]. Because Abrikosov vortices are immobile, typically pinned to defects, winding them is a thought experiment that is not easily implemented [104–106].

A proposal to mobilize vortices by injecting them into the edge modes of a topological superconductor was suggested by Beenakker *et al.* [38]. The parity carried by such edge-vortices can be used to encode a qubit. After the injection, the edge-vortices can be braided with bulk vortices due to their chiral motion without requiring any external manipulation. This results in a fermion parity switch (flip of the qubit) between the edges and the bulk that can be detected electrically as an $e/2$ charge pulse when a pair of edge vortices is fused in a normal metal contact [107, 108].

The key component of the braiding device of Ref. 38 is the edge-vortex injector (see Fig. 6.1): it consists of a flux-biased Josephson junction,

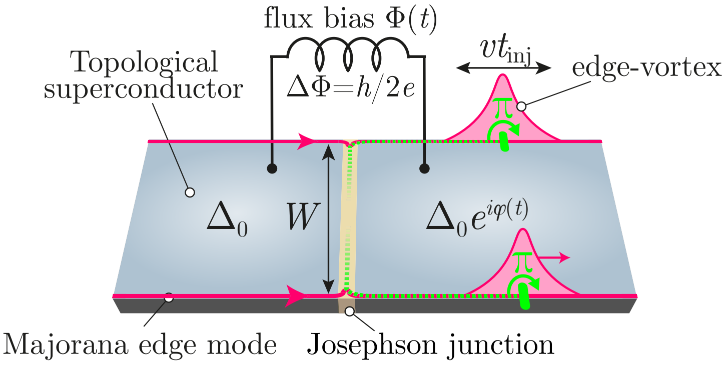

Figure 6.1: Edge vortex injector [38], consisting of a Josephson junction in a topological superconductor with co-propagating chiral edge modes. An $h/2e$ flux increment injects a pair of edge-vortices on opposite edges with a protected fermion parity. The corresponding phase domain wall is represented with green lines. The adiabatic description of the injection process assumes that the injection time $t_{\rm inj} = (2\pi\xi_{\rm J}/W)({\rm d}\varphi/{\rm d}t)^{-1}$ is long compared to the propagation time W/v along the junction. In this work we relax that assumption, to simulate a device (Fig. 6.2) where these dynamically injected edge-vortices are braided with Abrikosov bulk vortices.

connecting co-propagating chiral edge modes. The application of a flux bias of $h/2e$ increments the superconducting phase φ by 2π. For the fermionic edge mode wave functions this amounts to a π-phase domain wall [37], which moves away from the junction with the Fermi velocity v, carrying the edge-vortex excitations. The injection process takes a finite time $t_{\rm inj}$, that translates into a finite width $vt_{\rm inj}$ of the domain wall. Given a rate of change ${\rm d}\varphi/{\rm d}t$, a junction width W, and a superconducting coherence length $\xi_{\rm J}$ one has

$$t_{\rm inj} = (2\pi\xi_{\rm J}/W)({\rm d}\varphi/{\rm d}t)^{-1}. \tag{6.1}$$

A major simplification of the theoretical description of the injection process arises if $t_{\rm inj}$ is large compared to the propagation time W/v, so for a sufficiently slow rate of change ${\rm d}\varphi/{\rm d}t \ll 2\pi v\xi_{\rm J}/W^2$. This is the so-called adiabatic regime, in which one may rely on the instantaneous scattering approximation. Ref. 38 applies to that regime. The purpose of the present work is to relax the adiabatic approximation, to see how large $(v/W)t_{\rm inj}$ should be for the braiding operation to succeed. This is studied via a fully dynamical simulation of the proposed device during the injection, braiding and fusion.

Since an edge vortex is a collective degree of freedom, the dynamics involves the full many-body state. We study it numerically, by means of time-dependent Bogoliubov-de Gennes methods. Our main conclusion is that a factor of two between t_{inj} and W/v is sufficient to avoid the excitations of internal degrees of freedom in the junction that would spoil the fermion parity switch [109–112].

The outline of the chapter is as follows: the simulated device and the time-dependent model are introduced in Sec. 6.2. In Sec. 6.3, we present the results of the braiding protocol which recover the main predictions from the adiabatic theory, namely the charge signature at the exit of the device and the fermion parity exchange of the edges with the bulk. Sec. 6.4 describes the excitation dynamics of the junction in the alternative regime $W > vt_{\mathrm{inj}}$ where the braiding protocol cannot hold. The conclusion is presented in Sec. 6.5.

6.2. Model and device

6.2.1. Setup

We consider the device shown in Fig. 6.2 (a). A quantum anomalous Hall (QAH) insulator ($\mathcal{N} = 2$) exhibits an electronic chiral mode (corresponding to two Majorana fermions in the BdG formalism), on each of the two edges [113–115]. When the edge of a QAH is proxitimitized by an s-wave superconductor, the fermionic edge mode splits into two spatialy separated co-propagating chiral Majorana fermions, localized at the edges of the superconducting region [116, 117]. This proximitized system can be described as a topological superconductor ($\mathcal{N} = 1$). In our setup, such a topological superconductor (TSC) with two co-propagating Majorana edge modes (Fig. 6.2 (b)) is divided in three sections by two Josephson junctions, each of length W and thickness w. The junctions are separated by a distance L. Two vortices of flux $\Phi_0 = h/2e$ are created in the bulk by an external magnetic field, one of which is in the region between the two junctions.

A time-dependent flux bias is applied such that the phase in the middle superconductor is $\varphi(t)$ relative to the others, as in Fig. 6.1. By increasing the phase $\varphi(t)$ from 0 to 2π, the effective gap inside the Josephson junctions closes at $\varphi = \pi$ (Fig. 6.2 (c)). In this process, a Josephson vortex [119] passes through each junction, which must locally change the boundary condition from periodic to anti-periodic along the two edges [37] inducing

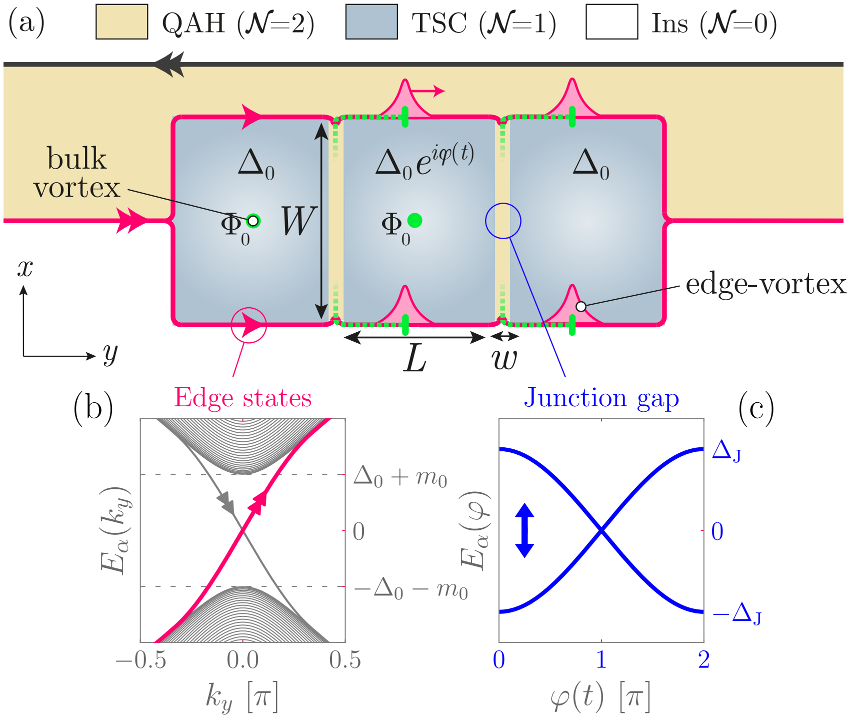

Figure 6.2: (a) Full braiding device: two injectors (as in Fig. 6.1) are used to produce pairs of edge-vortices. The pair of edge-vortices at the back exchanges parity with the bulk vortices upon overtaking a bulk vortex, which is detected by an $e/2$ charge measurement at the exit. (b) Dispersion of Majorana edge modes (magenta), calculated for an infinite strip of a topological superconductor ($\mathcal{N} = 1$). (c) Lowest energy levels in an infinite Josephson junction (described in Sec. 6.2) as a function of the superconducting phase. At $\phi = \pi$ these modes become degenerate and correspond to chiral Majorana edge states propagating along the junction [118].

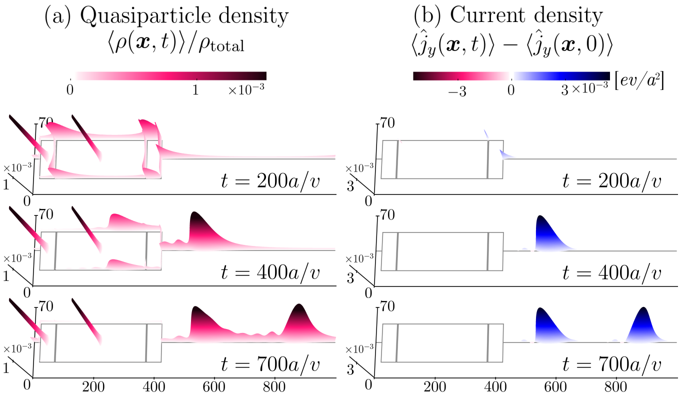
(a) Quasiparticle density $\langle\rho(\boldsymbol{x},t)\rangle/\rho_{\text{total}}$

(b) Current density $\langle\hat{j}_y(\boldsymbol{x},t)\rangle - \langle\hat{j}_y(\boldsymbol{x},0)\rangle$

Figure 6.3: Time snapshots of a dynamical simulation of the full device during the injection and braiding protocol, (a) Bogoliubov quasiparticle density as defined in equation (6.19) and (b) current density as defined in (6.11). In this simulation $vt_{\text{inj}} = 1.5W \ll L$, so the edge-vortices injected at the back and front junction are well separated creating two separate $e/2$ charge pulses upon fusion. An animated version can be found at `http://link.aps.org/supplemental/10.1103/PhysRevB.108.235309`.

a phase domain wall in the wave functions over some characteristic time t_{inj}. This local change of the boundary conditions can be described in terms of an edge vortex field operator $\hat{\mu}(x)$, a collective excitation with non-Abelian statistics [37, 107]. The injected edge-vortices – one pair at the back junction and another pair at the front junction – then propagate along the edges with the Fermi velocity v. The injection time is given by $t_{\text{inj}} = (2\pi\xi_{\text{J}}/W)(\mathrm{d}\varphi(t)/\mathrm{d}t)^{-1}$ where $\xi_{\text{J}} = \hbar v/\Delta_{\text{J}}$ [38] is the coherence length of the junction. Here Δ_{J} denotes the effective gap in the junction [118] (calculated for an infinite junction as shown in Fig. 6.2 (c)). As long as the characteristic injection time is slow compared to W/v, only the two lowest energy states in the finite junction play a role in the dynamics (see App. 6.C).

The edge-vortices of size vt_{inj} then propagate along the edges. The pair of edge-vortices injected at the back overtake a bulk vortex over a distance L. This induces a relative sign flip between the edge vortices and effectively results in a quasiparticle being transferred between the edge vortices and the vortices in the bulk. This parity switch of the edge vortices and the bulk vortices is denoted by $P_{\text{edges}} \to -P_{\text{edges}}$ and $P_{\text{vortices}} \to -P_{\text{vortices}}$, i.e. a flip of the qubit encoded in parity of the edge-vortices.

The braiding event can be detected upon the fusion at the exit of the superconductor via a charge measurement. The edge-vortices injected at the front junction produce a charge $e/2$ independently, while the edge-vortices injected at the back junction produce a charge $\pm e/2$ depending on whether they have braided with the bulk vortex. The resulting net charge at the exit is $e(N_{\mathrm{vortex}} \mod 2)$ with N_{vortex} the number of vortices in between the two injectors. In Fig. 6.3, the local excitation density and local charge during the braiding protocol are shown for an example simulation.

6.2.2. Hamiltonian

The device of Fig. 6.2 is simulated using a tight-binding model of a QAH. In the central regions the QAH is proximitized with an s-wave superconductor. The Hamiltonian is given by [116]:

$$\hat{H}(t) = \frac{1}{2} \sum_{\boldsymbol{x}} \hat{\Psi}^\dagger(\boldsymbol{x}) H(\boldsymbol{k}, \boldsymbol{x}, t) \hat{\Psi}(\boldsymbol{x}) \tag{6.2}$$

where $\hat{\Psi}(\boldsymbol{x}) = (\hat{\psi}_\uparrow(\boldsymbol{x}), \hat{\psi}_\downarrow(\boldsymbol{x}), \hat{\psi}_\downarrow^\dagger(\boldsymbol{x}), -\hat{\psi}_\uparrow^\dagger(\boldsymbol{x}))^\intercal$ is the four component Nambu spinor and H is the Bogoliubov-de-Gennes (BdG) Hamiltonian matrix

$$H(\boldsymbol{k}, \boldsymbol{x}, t) = \begin{pmatrix} H^e(\boldsymbol{k}, \boldsymbol{x}) - \mu & \Delta_0(\boldsymbol{x}) e^{i\vartheta(\boldsymbol{x},t)} \\ \Delta_0(\boldsymbol{x}) e^{-i\vartheta(\boldsymbol{x},t)} & \mu - \mathcal{T} H^e(\boldsymbol{k}, \boldsymbol{x}) \mathcal{T}^{-1} \end{pmatrix} \tag{6.3}$$

with μ the chemical potential and $\mathcal{T} = i\sigma_y \mathcal{K}$ the time-reversal operator (σ_y is the second Pauli matrix in the spin degree of freedom and $\mathcal{K}$ denotes complex conjugation). The electronic block is given by:

$$\begin{aligned} H^e(\boldsymbol{k}, \boldsymbol{x}) = {} & \frac{\hbar v}{a} (\sigma_x \sin(k_x a) + \sigma_y \sin(k_y a)) \\ & + (m_0(\boldsymbol{x}) + M(\boldsymbol{k}))\sigma_z \end{aligned} \tag{6.4}$$

where $M(\boldsymbol{k}) = \frac{2m_1}{a^2} (2 - \cos(k_x a) - \cos(k_y a))$ and $\boldsymbol{k} = -i\nabla$. The simulated system is finite in the x-direction and anti-periodic in the y-direction to ensure that there are no $\boldsymbol{k} = 0$ modes in the edges initially [37, 118].

The different Chern numbers in the regions of Fig. 6.2 are achieved by different values of m_0 and Δ_0:

$$\begin{aligned} m_0(\boldsymbol{x}) &= -0.5,\ \Delta_0(\boldsymbol{x}) = 0:\ \boldsymbol{x} \in \mathrm{QAH} \\ m_0(\boldsymbol{x}) &= -0.5,\ \Delta_0(\boldsymbol{x}) = 1:\ \boldsymbol{x} \in \mathrm{TSC} \\ m_0(\boldsymbol{x}) &= +\infty,\ \ \Delta_0(\boldsymbol{x}) = 0:\ \boldsymbol{x} \in \mathrm{Ins} \end{aligned} \tag{6.5}$$

in units of $\hbar v/a$. The trivial insulating region (Ins) is realized by truncation of the lattice. Furthermore we fix the width of the junction to $w = 2a$ and the length to $W = 42a$. This length ensures that the separation between edges and vortices is much larger than their respective localization lengths. The effective gap Δ_J inside the junctions is estimated numerically from the spectrum of an infinitely long junction (see Fig. 6.2), which yields $\Delta_\mathrm{J} \approx 0.12\Delta_0$.

In the TSC, $\vartheta(\boldsymbol{x}, t) = \eta(\boldsymbol{x}) + \varphi(\boldsymbol{x}, t)$ is the pair potential phase with η describing the vortices by $\nabla \times \nabla\eta = \sum_{\boldsymbol{x}_\mathrm{vortex}} 2\pi\delta(\boldsymbol{x} - \boldsymbol{x}_\mathrm{vortex})$; $\nabla \cdot \nabla\eta = 0$, and $\varphi(\boldsymbol{x}, t)$ describing the time-dependent bias, which is only nonzero in the middle superconductor and given by:

$$\varphi(t) = 2\pi\left(\theta(\tau - t)t/\tau + \theta(t - \tau)\right), \qquad t \geq 0 \tag{6.6}$$

over a characteristic time τ. Here $\theta(t)$ denotes the Heaviside step function. For this profile, the estimated injection time is simply $t_\mathrm{inj} = \tau\hbar v/(\Delta_\mathrm{J} W)$.

6.2.3. Computation of observables in the evolved many-body state

Before the injection, the system is assumed to be in the stationary ground state of $\hat{H}(0)$ denoted by $|\Omega\rangle$. Here, we consider the evaluation of single-particle operators in the evolved many-body state $\hat{U}(t)\,|\Omega\rangle$ with the time-evolution operator $\hat{U}(t) = T\exp\Big(-(i/\hbar)\int_0^t \hat{H}(t')\mathrm{d}t'\Big)$, T being the time-ordering operator. Relative to the initial ground state, the net change in the expectation value of a single-particle operator $\hat{A}$ is denoted:

$$\langle \hat{A}(t)\rangle - \langle \hat{A}(0)\rangle := \langle\Omega|\,\hat{U}^\dagger(t)\hat{A}\hat{U}(t)\,|\Omega\rangle - \langle\Omega|\,\hat{A}\,|\Omega\rangle\,. \tag{6.7}$$

The effective description of the superconductor can be reduced to a non-interacting model using the BdG formalism. In App. 6.A.1, we show how we can transform this many-body problem into single-particle problems which can be solved within the first quantization formalism. Eq. (6.7) can be written as:

$$\langle \hat{A}(t)\rangle - \langle \hat{A}(0)\rangle = \frac{1}{2}\sum_{\alpha\in S^-}\Big(\langle\alpha(t)|\,A\,|\alpha(t)\rangle - \langle\alpha|\,A\,|\alpha\rangle\Big). \tag{6.8}$$

Here A is the single-particle BdG operator associated with $\hat{A}$, $|\alpha\rangle := |\alpha(0)\rangle$ denotes the α-th eigenstate of $H(0)$ and $|\alpha(t)\rangle$ obeys

$$i\hbar\partial_t\,|\alpha(t)\rangle = H(t)\,|\alpha(t)\rangle\,. \tag{6.9}$$

The evolution of the state $|\alpha(t)\rangle$ is calculated numerically using the python package Tkwant [97, 120–123]. This approach has numerical complications as it requires to evolve all the N states in S^- in order to achieve convergence (see App. 6.A.2).

We resolve this issue by writing A in terms of the basis of eigenstates of $H(0)$:

$$\langle \hat{A}(t)\rangle - \langle \hat{A}(0)\rangle = \mathrm{Re}\sum_{\substack{\alpha\in S^-\\ \mu\in S^+}}\sum_{\nu\in S}\langle\alpha(t)|\mu\rangle\,\langle\mu|\,A\,|\nu\rangle\,\langle\nu|\alpha(t)\rangle\,. \tag{6.10}$$

Here the sets S^+ and S^- denote positive and negative energy state indices respectively[1] and S their union $S^+\cup S^-$. In contrast with Eq. (6.8) (see App. 6.A.2), this form only gives non-zero contributions in a finite range around $E=0$. This allows us to approximate this expression by truncating the sum and discarding all terms above some energy cut-off, i.e terms with $|E_{\alpha,\mu,\nu}| > E_{\mathrm{max}}$.

6.3. Results

In this section we present the main results of our simulation. We show the charge signature of the braiding protocol and calculate the corresponding parity switch. We consider a system where W is smaller, but comparable to the injection time $vt_{\mathrm{inj}} \approx 2W$. While the theoretical description, relying

---

[1] Notice that particle-hole symmetry enforces that the eigenstates of the BdG Hamiltonian H come in pairs of opposite energies. The eigenspace of zero modes of H must be even dimensional and there must exist a basis of particle-hole partners in it. For each pair, we arbitrarily chose one state to be in S^+ and put its partner in S^-. Thus, in general, S^+ contains zero modes. Overall it contains half of the states (n states) and if we act on them with the particle-hole symmetry operator, we obtain S^-.

on the adiabatic limit, no longer holds for this system we show that the main predictions remain unchanged.

6.3.1. Quantized charge measurement

We first consider the charge signature that can be measured at the exit of the device, after the fusion of the edge vortices. For this we evaluate the current density operator $\hat{\jmath}_y(\boldsymbol{x}) = (ev/a^2)\hat{\Psi}^\dagger(\boldsymbol{x})\nu_0\sigma_y\hat{\Psi}(\boldsymbol{x})$ in the y-direction using Eq. (6.10). Here, ν_0 is the identity acting on the particle-hole degree of freedom. Defining the current as:

$$I(t) = a \sum_{\boldsymbol{x}|y=y_{\text{exit}}} \langle \hat{\jmath}_y(\boldsymbol{x},t)\rangle - \langle \hat{\jmath}_y(\boldsymbol{x},0)\rangle \tag{6.11}$$

the net charge creation is given by the time integral:

$$Q(t) = \int_0^t I(t')\mathrm{d}t'. \tag{6.12}$$

With this, we can calculate the charge pumped during the braiding protocol at the exit of the device (y_{exit}). The spatial separation L between the two Josephson junctions allows to distinguish between two characteristic charge signatures. When $L \gg vt_{\text{inj}}$, the injection events at each junction are well separated in space. In this case, the two pairs of edge-vortices produce separate signals of $\pm\frac{e}{2}$ charge at the exit. The charge contribution of the second pair of edge vortices experiences a sign flip in the presence of bulk vortices, as a consequence of braiding [107]. The theoretical predictions from Refs. 38, 107 are compared with numerical results in the left panel of Fig. 6.4. On the other hand when $L \lesssim vt_{\text{inj}}$, the injection events at both junctions are close, so that the overlapping electrical signals add up, producing a unit charge signature (Fig. 6.4 (b)).

The transferred charge is an indirect probe of the braiding event as it is a result of the fusion between the edge vortices. It is therefore only quantized if the path lengths of the two vortices between injection and fusion are the same [107]. In contrast, the parity exchange is topologically protected, it does not depend on microscopic details. We will check this numerically.

6.3.2. Parity switch of edge-vortices

The phase rotation $\varphi(t) : 0 \to 2\pi$ in the superconductor changes the parity locally carried by the two bulk vortices. Since parity must be

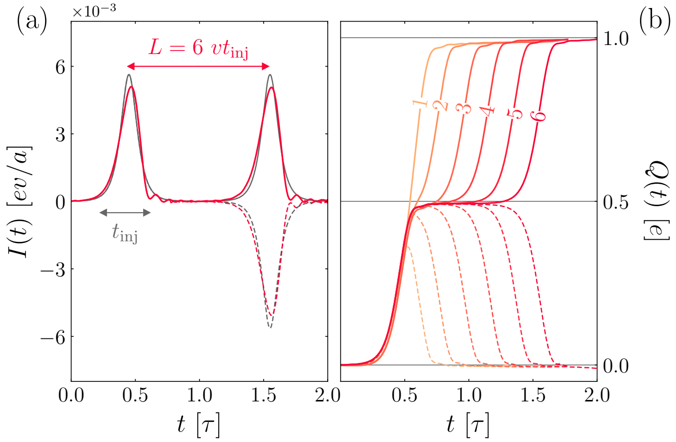

Figure 6.4: (a) Simulated (pink) and theoretical (gray) current density at the exit of the superconductor. A system without (with) vortices is represented with dashed (solid) lines. The pulse width $t_{\mathrm{inj}} \approx \tau/5.17$ is indicated. (b) Corresponding charge increase, for different values of the inter-junction separation L, with values of $L/v\tau$ shown on top of the curves. All simulations have $\tau = 500a/v$ and $W = 42a$.

globally conserved, then necessarily there must be an odd number of excitations elsewhere in the system –namely carried by the edges [38]. This change of parity is a direct consequence of braiding between the bulk and edge vortices. To characterize this process we first identify the parity subsectors that correspond to the states in the bulk vortices and the edges.

The full parity operator can be written –up to the sign of the initial ground state parity– in terms of the Bogoliubov operators as:

$$\hat{P} = \prod_{\alpha \in S^+} \left(1 - 2d^\dagger_\alpha d_\alpha\right). \tag{6.13}$$

We provide a further explanation for this form in App. 6.B.1. In our device, $\hat{P}$ can be split in a product of two terms, the first one corresponding to the bulk vortex excitation (i.e. the fermionic superposition of the two vortex

Majorana zero-modes) and the second one containing all other excitations:

$$\begin{aligned}\hat{P} &= \left(1 - 2d^\dagger_{\alpha_v} d_{\alpha_v}\right) \cdot \prod_{\substack{\alpha\in S^+\\ \alpha\neq\alpha_v}} \left(1 - 2d^\dagger_\alpha d_\alpha\right) \\ &:= \hat{P}_{\text{vortices}} \cdot \hat{P}'\end{aligned} \tag{6.14}$$

where α_v is the index of the fermionic state bound to the vortices. This can be done if the vortex state is well isolated from the rest (i.e. there is no hybridization between vortex and edge states). $\hat{P}'$ can be evolved in the Heisenberg picture and expressed in terms of the Bogoliubov operators of the initial Hamiltonian $\{d_\beta\}_{\beta\in S}$. As we show in App. 6.B.1, the time evolution of each d_α can be expanded as

$$\hat{U}^\dagger d_\alpha \hat{U} = \sum_{\beta\in S} \chi_{\alpha\beta} d_\beta \quad \text{with} \quad \chi(t)_{\alpha\beta} = \langle\alpha(0)|\beta(t)\rangle \tag{6.15}$$

The time evolution of $\hat{P}'$ can then be expressed as a sum of terms of different orders in d operators

$$\begin{aligned}\hat{U}^\dagger \hat{P}' \hat{U} = \Big(1 &- 2\sum_{\alpha\in S^+}\sum_{\mu,\nu\in S} \chi^*_{\alpha\mu}\chi_{\alpha\nu} d^\dagger_\mu d_\nu \\ &+ 4 \sum_{\substack{\alpha,\beta\in S^+\\ E_\beta > E_\alpha}} \sum_{\mu,\nu,\sigma,\tau\in S} \chi^*_{\alpha\mu}\chi_{\alpha\nu}\chi^*_{\beta\sigma}\chi_{\beta\tau} d^\dagger_\mu d_\nu d^\dagger_\sigma d_\tau + \cdots\Big).\end{aligned} \tag{6.16}$$

Its expectation value in the ground state $|\Omega\rangle$ can then be calculated making use of Wick's theorem up to all orders. The final equation can be found in App. 6.B.1 (Eq. (6.52)).

In our numerical calculation we neglect correlators of order higher than four, and only include states within an energy window E_{max}. This energy window is chosen to match the maximum excitation energy in order for the parity calculation to converge (see App. 6.C).

Since edge and junction states are hybridized, $\hat{P}'$ cannot be decomposed similarly in edge and junction sectors. However, after the bias pump, the expectation value $\langle\hat{P}'\rangle$ can be identified with the parity carried by the edges $\langle\hat{P}_{\text{edge}}\rangle$ as long as the filling of junction states – which only exist for energies $E \geq \Delta_{\text{J}}$ – is negligible. The different intensities of red in Fig. 6.5 show the value obtained for $\hat{P}'$ as we increase E_{max}. We see that convergence is achieved before we need to include any states with energies around Δ_J. This identification of $\langle\hat{P}'\rangle \approx \langle\hat{P}_{\text{edge}}\rangle$ is further supported in

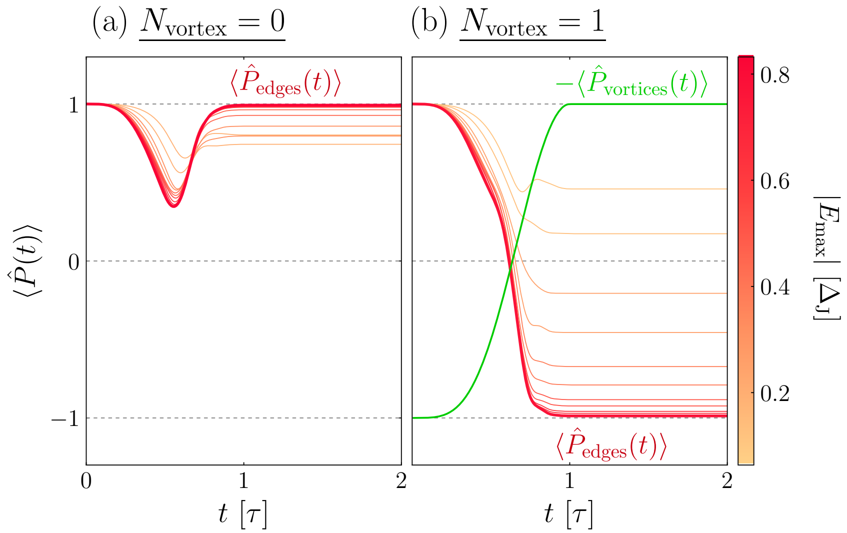

Figure 6.5: Evolution of the parity operator expectation value in the initial ground state without (a) and with vortices (b). In panel (b), the parity of the vortices is separated from the edges, and a parity switch is observed. Convergence of the curves as a function of E_{max} is shown in color.

Sec. 6.4 and App. 6.C.

Fig. 6.5, shows that the parity expectation of the edges is unchanged when there are no vortices, but it switches in the presence of bulk vortices. This demonstrates that, for this set of parametes, the braiding of edge-vortices holds dynamically, and that the internal degrees of freedom in the junction do not spoil the exchange of parity. This implies that neither the adiabatic nor the point junction limits need to be satisfied for braiding to be realised.

6.3.3. Topological protection of the edge vortices

The phase domain wall created during the quench corresponds to a pair of edge vortices that propagate along the edges. As one of them surrounds the bulk vortex it picks up a phase that realises the parity switch [107]. Since a π domain wall cannot be unwound, this mechanism is protected from all local sources of disorder. In this part, we verify that the dynamically injected vortices are topologically protected by introducing irregularities in the spatial profile of $\Delta_0(\boldsymbol{x})$. We show how an additional

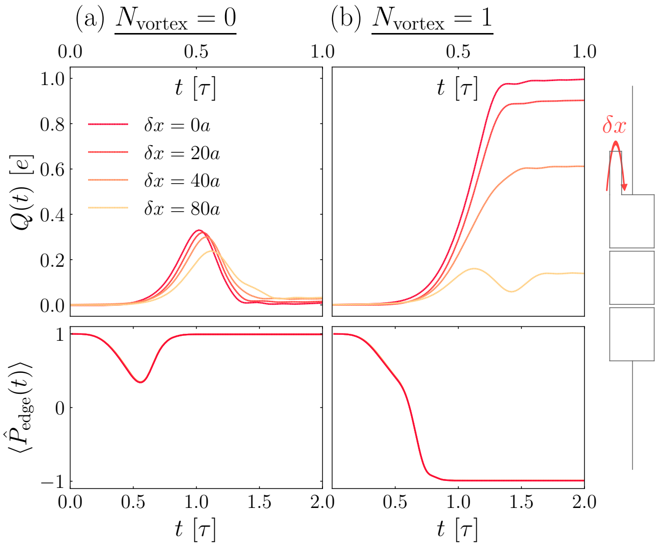

Figure 6.6: (Top) Net charge increase at the exit of the superconductors without (a) and with (b) vortices, with four geometrically induced path length differences between the edges δx for $\tau = 500a/v$. (Bottom) Parity of the edge sector for the same data sets. The calculated parity is independent of δx. In this case the data sets overlap making the different curves indistinguishable.

path-length δx in the upper edge (see the top panel of Fig. 6.6) influences the charge signature, fully spoiling the quantization discussed in Sec. 6.3.1 in agreement with the predictions in Ref. 107. In contrast, our calculation of parity (see the bottom panel of Fig. 6.6) remains unaffected by the local changes in the system, demonstrating the topological protection of the edge-vortex excitations. This confirms that even for a finite junction, edge-vortices can be used to encode protected quantum information.

6.4. Long junction dynamics

Our results so far have considered the particular case $vt_{\text{inj}} \sim 2W$ where the injection process is not spoiled by the excitation of junction modes. In this section, we consider the more general case where the ratio vt_{inj}/W is varied. In particular, we investigate how trapped excitations can influence the creation of edge-vortices for sufficiently long-junctions.

6.4.1. Quasi-particle excitation spectrum

To understand the behaviour in the junction we first study the quasi-particle excitation spectrum $E(\varphi)$. Within the superconducting gap, this spectrum consists of states localized in the bulk vortices, junction and edges. The injection process is characterized by the gap closing at $\varphi = \pi$ with the dispersion $E_\mathrm{J} = \pm\Delta_\mathrm{J}\cos\varphi/2$ seen before in Fig. 6.2. In our case, the junction states couple with the edge states, forming hybridized bands seen in Fig. 6.7 (gray lines). We calculate the occupation number of these energy levels:

$$\hat{N}(\varphi) = \sum_{E_\mu(\varphi)\in S^+} d^\dagger_\mu(\varphi) d_\mu(\varphi) \tag{6.17}$$

where each term $d^\dagger_\mu(\varphi) d_\mu(\varphi)$ counts the quasi-particle occupation within a single energy level μ. The expectation value in the evolved state $\hat{U}(t)\left|\Omega\right\rangle$ is then given by:

$$\langle\hat{N}(\varphi,t)\rangle = \mathrm{Re}\sum_{\substack{\alpha\in S^-\\ \mu\in S^+}}\sum_{\nu\in S}\langle\alpha(t)|\mu^\varphi\rangle\left\langle\mu^\varphi\right|N\left|\nu^\varphi\right\rangle\langle\nu^\varphi|\alpha(t)\rangle \tag{6.18}$$

where $\left|\mu^\varphi\right\rangle$ denotes an eigenstate of $H(\varphi)$ and $N = \mathbb{1}$.

The occupation of each level through-out the quench is shown by thick lines in Fig. 6.7, where the color is used to distinguish between edge (red) and junction (blue) states.[2] The slow injection case (a) treated in Sec. 6.3 shows that the junction states are only occupied near values of $\varphi = \pi$ and fully emptied in the edges at the end of the injection. In panel (b), the injection is short enough to create excitations in the levels $E > \Delta_\mathrm{J}$. Note that, in this case, the approximation $\langle\hat{P}'\rangle$ made in Sec. 6.3.2 fails because of nonzero occupation in the junction. This means that the parity switch is no longer fully carried by the edge modes, which we attribute to trapped excitations in the Josephson junction.

6.4.2. Trapped excitations

In the presence of a finite Josephson junction the coupling between the two edges is mediated by their hybridization with the chiral states in the Josephson junction. This hybridization is only supported for a duration t_inj around $\varphi = \pi$, when the junction is effectively gapless. We have shown that when $vt_\mathrm{inj} \sim 2W$ the travel time W/v is short enough to allow the

---

[2] The color at a value φ and band μ is proportional to the value $\sum_{\boldsymbol{x}\in\text{junctions}}|\langle\mu^\varphi|\boldsymbol{x}\rangle|^2$.

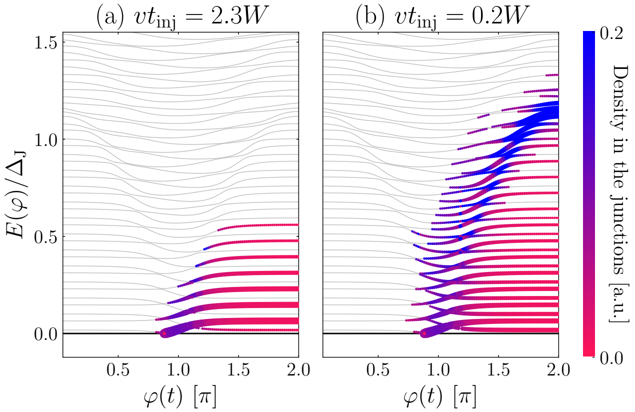

Figure 6.7: Quasi-particle occupation of the energy levels (thick colored lines; a thick line signifies a strong occupation) above the ground state level ($E = 0$), superimposed on the time-independent energy spectrum of $H(\varphi)$ (thin gray lines). The color of the lines distinguishes between junction (blue) and edge (red) states. At fast injection (b), the quasiparticle occupation in the junction levels $E_\mu \geq \Delta_{\mathrm{J}}$ at final time is high. We have removed the vortex state from this figure.

excitations to escape the junctions before the gap re-opens. Here we show that in the alternative regime $vt_{\mathrm{inj}} < W$, the excitation is partially trapped in the gapped bound state of the junction.

In order to describe the quasi-particles inside the junction, we define an excitation density via a spatial projection of the quasi-particle number $N(\boldsymbol{x}) = \mathcal{P}(\boldsymbol{x}) N \mathcal{P}(\boldsymbol{x})$. This is done similarly to our description of charge (i.e. $\langle \boldsymbol{x}' | N(\boldsymbol{x}) | \boldsymbol{x}'' \rangle = \sigma_0 \nu_0 \delta_{\boldsymbol{x}',\boldsymbol{x}''} \delta_{\boldsymbol{x},\boldsymbol{x}'}$) arriving to the expression:

$$\langle \hat{\rho}_\varphi(x,t) \rangle = \mathrm{Re} \sum_{\substack{\mu \in S^+ \\ \alpha \in S^-}} \sum_{\nu \in S} \langle \alpha(t) | \mu^\varphi \rangle \langle \mu^\varphi | N(\boldsymbol{x}) | \nu^\varphi \rangle \langle \nu^\varphi | \alpha(t) \rangle \,. \tag{6.19}$$

Note that when integrated over the whole system, the Eq. (6.18) is recovered. Integrating this density locally gives the number of quasi-particle inside junctions $\langle \hat{N}_{\mathrm{junc}}(t) \rangle$ and edges $\langle \hat{N}_{\mathrm{edges}}(t) \rangle$.

In Fig. 6.8, we show how the quasi-particle changes with time for two different systems. When the injection is slow (a) the quasi-particle number in the junction is fully transferred to the edges as anticipated. In the alternate case when the injection is very fast (b), the particle number slowly

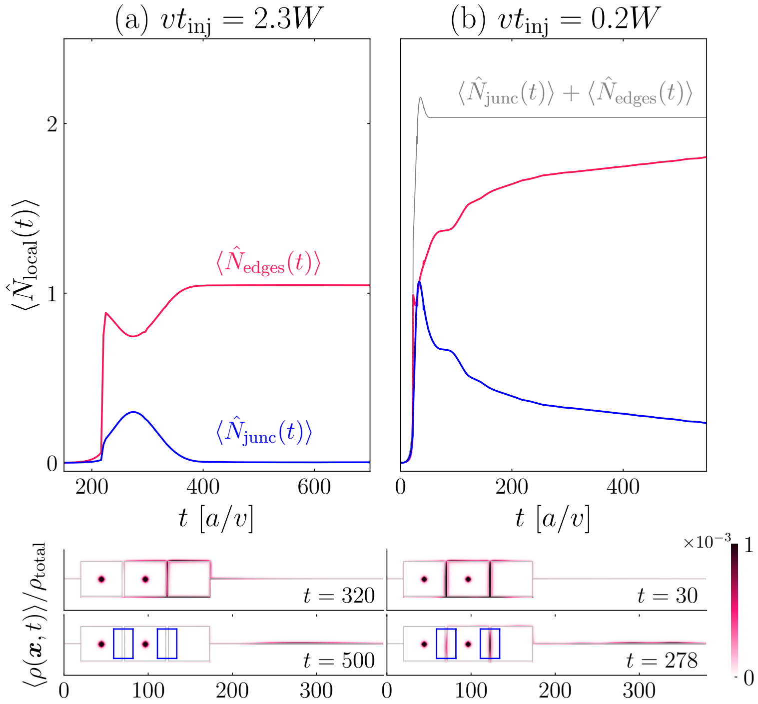

Figure 6.8: Bogoliubov quasi-particle number inside the junction (red) and inside the edges (blue) as a function of time. Panel (a) shows that the junction excitation fully escapes into the edges, while in (b), at short injection time, the junction contains residual quasi-particles. The bottom panels show the corresponding quasi-particle densities at two different times times. The integration window used to calculate the quasi-particle number inside the junction is marked with a blue rectangle. An animated visualisation can be found in http://link.aps.org/supplemental/10.1103/PhysRevB.108.235309.

decays towards a constant residual value in the junctions corresponding to quasi-particles occupying the lowest bound state in the Josephson junctions. As this trapped excitation can carry a part of the parity exchange it can spoil the injection protocol as well as the characteristic charge signature (shown in App. 6.C). For this reason, it is important to find a bound for t_{inj} above which the trapped excitations in the junction can be neglected.

6.4.3. Particle number in the junction

In the adiabatic theory Ref. 38, the total particle number produced in the edges at final time is equal to 1.037. The non-quantized number is due to particle-hole pairs production during the injection process. At slow injection, we find a comparable value $\langle \hat{N}_{\mathrm{junc}} \rangle + \langle \hat{N}_{\mathrm{edge}} \rangle = 1.049$ as indicated in Fig. 6.8 (a), close to the adiabatic theory. For the fast injection in Fig. 6.8, this is $\langle \hat{N}_{\mathrm{junc}} \rangle + \langle \hat{N}_{\mathrm{edge}} \rangle = 2.033$ instead.

We therefore turn to a quantitative description of the residual particle number in the junction $\langle \hat{N}_{\mathrm{junc}} \rangle$ for different values of vt_{inj}/W. We achieve this by simulating different values of τ in Fig. 6.9. In Fig. 6.9 (a), the particle number is shown as a function of time for different values of vt_{inj}/W, where we distinguish between the two regimes $vt_{\mathrm{inj}} > W$ and $vt_{\mathrm{inj}} < W$ by two colors. In panel (b), we show that the residual excitation number in the junction decreases fast as the injection time becomes long. We match this with an exponential shown in Fig. 6.9. After $vt_{\mathrm{inj}} > 2W$, this value has nearly decayed to zero. In an experimental setting, this provides us with an upper bound on the flux bias change rate $|\mathrm{d}\Phi/\mathrm{d}t| < \Phi_0 v/2W^2\Delta_{\mathrm{J}}$ when the parity exchange is fully carried by the edges corresponding, ensuring a successful injection of edge vortices.

6.5. Conclusion

In this work we have shown how a braiding protocol introduced in Ref. 38 can be dynamically simulated as a tight-binding many-body system. With this setup we were able to fully probe the braiding process away from the limitations of the effective model. This allowed us to investigate the relevant scales in the system as well as compare the current signature with analytical predictions. We were able to study dynamically the local parity switch present in the edge states and show the topological protection of this exchange. We have shown that the injection and braiding of edge-vortices is uncompromised by a finite junction when $vt_{\mathrm{inj}} > 2W$, so that all the parity exchange is contained in the edge states. Additionally we studied

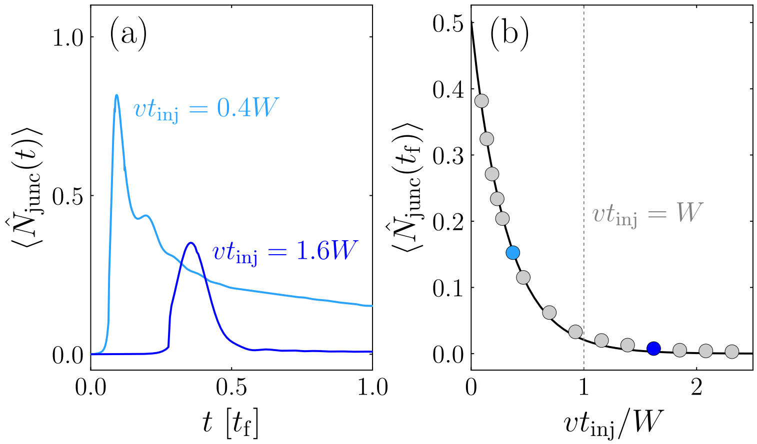

Figure 6.9: (a) Quasi-particle number inside the junction as a function of time, for two values of the injection time. (b) Residual quasi-particle number in the junction at some final time $t_f = 500a/v$ as a function of the ratio vt_{inj}/W. An exponential fit yields $\langle \hat{N}_{\mathrm{junc}}(t_{\mathrm{f}}) \rangle = N_0 \cdot \exp(vt_{\mathrm{inj}}/W\beta)$ with $\beta = 0.31$ and $N_0 = 0.5$.

this system away from this limit and investigated the excitations in the junction. Here, we showed that the lowest bound state of the junction remains excited long after the quench for sufficiently fast injections. While the parity switch $\langle \hat{P}' \rangle$ is still protected in this limit, we can no longer conclude that it is fully carried in the edge states, therefore providing a limitation for the use of such device as a topological qubit. For this reason we show the interplay of scales vt_{inj} and W to find a parameter regime, where the injection of edge vortices is well defined. We see that the adiabatic condition $vt_{\mathrm{inj}} \gg W$ discussed in previous works can be relaxed to $vt_{\mathrm{inj}} \gtrsim W$, while keeping the braiding predictions intact. This is helpful for future experimental work as it allows large deviations from the point junction limit.

6.A. Time-evolution of single-body operators in BdG

6.A.1. From second to first quantization

In a tight-binding system, any single-body operator $\hat{A}$ can be written as

$$\hat{A} = \sum_{\alpha,\beta=1}^{n} A^e_{\alpha\beta}\hat{\psi}^\dagger_\alpha \hat{\psi}_\beta, \qquad A^e_{\alpha\beta} = \langle 0| \hat{\psi}_\alpha \hat{A} \hat{\psi}^\dagger_\beta |0\rangle \,, \tag{6.20}$$

where $|0\rangle$ denotes the vacuum of electrons, which can be rewritten into the BdG form as

$$\hat{A} = \frac{1}{2}\hat{\Psi}^\dagger A \hat{\Psi} + \frac{1}{2}\operatorname{Tr} A^e \tag{6.21}$$

with

$$\begin{aligned} A &= \begin{pmatrix} A^e & 0 \\ 0 & -\sigma_y A^{e*}\sigma_y \end{pmatrix} \\ \hat{\Psi} &:= \Big(\hat{\psi}_{1\uparrow} \quad \hat{\psi}_{1\downarrow}\cdots \quad \hat{\psi}_{N/2\uparrow} \quad \hat{\psi}_{N/2\downarrow} \\ &\qquad \hat{\psi}^\dagger_{1\downarrow} \quad -\hat{\psi}^\dagger_{1\uparrow}\cdots \quad \hat{\psi}^\dagger_{N/2\downarrow} \quad -\hat{\psi}^\dagger_{N/2\uparrow}\Big)^T \end{aligned} \tag{6.22}$$

We can evolve this operator in the Heisenberg picture to obtain

$$\hat{U}^\dagger \hat{A} \hat{U} = \frac{1}{2}\hat{\Psi}(t)^\dagger A \hat{\Psi}(t) + \frac{1}{2}\operatorname{Tr} A^e \tag{6.23}$$

where we defined $\hat{\psi}_\alpha(t) = \hat{U}^\dagger \hat{\psi}_\alpha \hat{U}$. Since we intend to evaluate this operator in the ground state $|\Omega\rangle$ of the initial Hamiltonian, we need to write it in terms of the Bogoliubov operators $\{d_\beta\}_{\nu\in S}$ of $\hat{H}(0)$. It is possible to prove (see App. 6.A.3) that the $\{\hat{\psi}_\alpha(t)\}_{\nu\in S}$ operators can be written as linear combinations of these Bogoliubov operators as

$$\hat{\psi}_\alpha(t) = \sum_{\beta\in S}\Phi_{\alpha\beta}(t) d_\beta \qquad \text{i.e.} \qquad \hat{\Psi}(t) = \Phi(t)\mathbf{d} \tag{6.24}$$

where $\Phi(0)$ is the matrix that diagonalises the BdG Hamiltonian at $t = 0$, (i.e. $H(0) = \Phi(0)\mathcal{E}\Phi^\dagger(0)$) and $\Phi(t)$ is the solution of

$$i\hbar\partial_t\Phi(t) = H(t)\Phi(t). \tag{6.25}$$

Notice that this means that the columns of Φ are none other than the eigenstates of $H(0)$ evolved according to the Schrödinger equation for $H(t)$. With this, we can express

$$\hat{U}^\dagger \hat{A} \hat{U} = \frac{1}{2}\mathbf{d}^\dagger \Phi^\dagger A \Phi \mathbf{d} + \frac{1}{2}\operatorname{Tr} A^e \tag{6.26}$$

Finally, using the fact that by definition $\langle\Omega| d_\alpha^\dagger d_\beta |\Omega\rangle = \delta_{\alpha\beta}$ if $E_\alpha < 0$ and $\langle\Omega| d_\alpha^\dagger d_\beta |\Omega\rangle = 0$ otherwise, we obtain

$$\langle\hat{A}(t)\rangle - \langle\hat{A}(0)\rangle = \frac{1}{2}\sum_{\alpha\in S^-}\left(\Phi^\dagger(t) A \Phi(t) - \Phi^\dagger(0) A \Phi(0)\right)_{\alpha\alpha}, \tag{6.27}$$

which in Dirac notation becomes

$$\langle\hat{A}(t)\rangle - \langle\hat{A}(0)\rangle = \frac{1}{2}\sum_{\alpha\in S^-}\Big(\langle\alpha(t)| A |\alpha(t)\rangle - \langle\alpha(0)| A |\alpha(0)\rangle\Big). \tag{6.28}$$

With this, we have mapped our original problem of evolving many-body states in a Hilbert space of dimension 2^n into n first quantization problems in a Hilbert space of dimension $2n$.

6.A.2. Convergence

The fact that Eq. (6.28) involves all n negative energy eigenstates of H poses two problems. First, we only aim at describing the system accurately at low energies. Any realistic system will not share the specific high-energy behaviour of our tight-binding description far from the Fermi energy. Secondly, we should be able to understand our system by considering only states close to the Fermi energy, so evolving all of them is a waste of computational resources. Unfortunately we have no reason to belive that the contribution of both terms in Eq. (6.28) will cancel out as we go away from the Fermi energy. This was actually studied numerically and it was verified that the value of $\langle\hat{\jmath}_y(\boldsymbol{x},t)\rangle - \langle\hat{\jmath}_y(\boldsymbol{x},0)\rangle$ as given by Eq. (6.28) does not converge –instead it oscillates– as we increase the amount of states evolved (see Fig. 6.10). This section is devoted to rewrite this equation in a form that solves this issue. To do so, let us explicitly make use of basis of the eigenstates of $H(0)$ and introduce the completeness relation around

A in the first term of Eq. (6.28) to obtain

$$
\begin{aligned}
&\frac{1}{2}\sum_{\alpha\in S^-} \langle\alpha(t)|\, A\, |\alpha(t)\rangle = \\
&\frac{1}{2}\sum_{\alpha\in S^-}\sum_{\mu,\nu\in S} \langle\alpha(t)|\mu\rangle\, \langle\mu|\, A\, |\nu\rangle\, \langle\nu|\alpha(t)\rangle = \\
&\frac{1}{2}\sum_{\alpha\in S^-}\sum_{\mu,\nu\in S^-} \Big(\langle\alpha(t)|\mu\rangle\, \langle\mu|\, A\, |\nu\rangle\, \langle\nu|\alpha(t)\rangle \\
&\quad + \langle\alpha(t)|\mathcal{C}\mu\rangle\, \langle\mathcal{C}\mu|\, A\, |\nu\rangle\, \langle\nu|\alpha(t)\rangle \\
&\quad + \langle\alpha(t)|\mu\rangle\, \langle\mu|\, A\, |\mathcal{C}\nu\rangle\, \langle\mathcal{C}\nu|\alpha(t)\rangle \\
&\quad + \langle\alpha(t)|\mathcal{C}\mu\rangle\, \langle\mathcal{C}\mu|\, A\, |\mathcal{C}\nu\rangle\, \langle\mathcal{C}\nu|\alpha(t)\rangle \Big).
\end{aligned}
\tag{6.29}
$$

where $\mathcal{C} = \sigma_y\nu_y\mathcal{K}$ is the BdG charge conjugation operator and $\mathcal{C}\mu$ denotes the particle-hole partner of the state labeled μ. Since $\hat{A}$ is a single-particle operator, it satisfies $\mathcal{C}A\mathcal{C} = -A$. Given that $\{|\alpha(t)\rangle : \alpha \in (S^- \cup S^+)\}$ is a complete basis of the BdG Hilbert space, we can write the first term of Eq. (6.29) as

$$
\begin{aligned}
&\frac{1}{2}\sum_{\alpha\in S^-}\sum_{\mu,\nu\in S^-} \langle\alpha(t)|\mu\rangle\, \langle\mu|\, A\, |\nu\rangle\, \langle\nu|\alpha(t)\rangle = \\
&\qquad \frac{1}{2}\sum_{\mu\in S^-} \langle\mu|\, A\, |\mu\rangle \\
&-\frac{1}{2}\sum_{\alpha\in S^+}\sum_{\mu,\nu\in S^-} \langle\mathcal{C}\alpha(t)|\mu\rangle\, \langle\mu|\, A\, |\nu\rangle\, \langle\nu|\mathcal{C}\alpha(t)\rangle
\end{aligned}
\tag{6.30}
$$

If we plug this in Eq. (6.29) and then in Eq. (6.28), a few simplifications happen. The first term of this equation will cancel with the second term of Eq. (6.28), and the second term of Eq. (6.30) is real and equal to the last term of Eq. (6.29) (this follows from the properties of $\mathcal{C}$). In addition, the second and third terms of Eq. (6.29) are each other's complex conjugate. Taking all of this into account we can write down Eq. (6.28) as

$$
\begin{aligned}
&\langle\hat{A}(t)\rangle - \langle\hat{A}(0)\rangle = \\
&\mathrm{Re}\sum_{\alpha\in S^-}\sum_{\mu,\nu\in S^+} \Big(\langle\alpha(t)|\mu\rangle\, \langle\mu|\, A\, |\nu\rangle\, \langle\nu|\alpha(t)\rangle \\
&\quad + \langle\alpha(t)|\mu\rangle\, \langle\mu|\, A\, |\mathcal{C}\nu\rangle\, \langle\mathcal{C}\nu|\alpha(t)\rangle \Big)
\end{aligned}
\tag{6.31}
$$

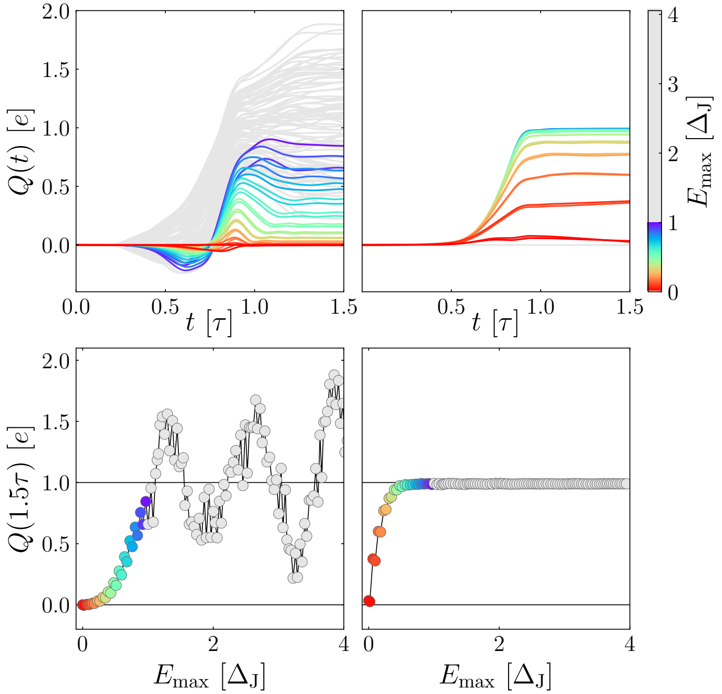

Figure 6.10: Convergence of the charge at the exit with two methods. Left: with charge expressed in the local basis using Eq. (6.27) where E_{max} is the maximum energy of the states in the sum over α. Right: With charge expressed in the basis of eigenstates of $H(0)$ using Eq. (6.32) where E_{max} is the maximum energy of the states in the sums over α, μ and ν.

which we write more simply in the main text as

$$\langle \hat{A}(t) \rangle - \langle \hat{A}(0) \rangle = \text{Re} \sum_{\substack{\alpha \in S^- \\ \mu \in S^+}} \sum_{\nu \in S} \langle \alpha(t) | \mu \rangle \langle \mu | A | \nu \rangle \langle \nu | \alpha(t) \rangle \tag{6.32}$$

This formula includes overlaps between positive energy and evolved negative energy states which ensures non-zero contributions to only exist around $E = 0$. In Fig. 6.10 we show how the contribution of the terms in the sum vanishes as we go further away from the Fermi energy, which lets us avoid having to evolve all negative energy states.

6.A.3. Proof of time evolution method

In this section we prove the following statement:

Proposition. *Let* $\hat{\Psi}$ *be the Nambu spinor of fermion creation and annihilation operators as defined in Eq. (6.22) satisfying* $\{\hat{\psi}_\alpha, \hat{\psi}_\beta^\dagger\} = \delta_{\alpha,\beta}$ *and* $\{\hat{\psi}_\alpha, \hat{\psi}_\beta\} = \delta_{\alpha,\mathcal{C}\beta}$ *where* $\mathcal{C}\alpha$ *is the index of* $(\hat{\psi}_\alpha)^\dagger$ *in* $\hat{\Psi}$ *(i.e.* $\hat{\psi}_{\mathcal{C}\alpha} = \hat{\psi}_\alpha^\dagger$*). Let*

$$\hat{H}(t) = \frac{1}{2}\hat{\Psi}^\dagger H(t)\hat{\Psi}$$

be the time-dependent BdG Hamiltonian describing a tight-binding superconducting system of fermions. Let $\hat{U}(t)$ *be its corresponding evolution operator. Let* $\mathcal{C}$ *be the antiunitary charge conjugation operator satisfying* $\mathcal{C}^2 = 1$ *and* $\{\mathcal{C}, H\} = 0$*. Let* $V(t)$ *be a matrix that diagonalises* $H(t)$ *and let* $\mathbf{d} = (d_1, d_2, \cdots, d_{2n})$ *be the spinor of Bogoliubov operators diagonalising* $\hat{H}(0)$*.*

Then, the time evolution of $\hat{\Psi}$ *can we written as*

$$\hat{\Psi}(t) := \hat{U}(t)^\dagger \hat{\Psi}\hat{U}(t) = \Phi(t)\mathbf{d} \tag{6.33}$$

where Φ *obeys*

$$i\hbar\partial_t\Phi(t) = H(t)\Phi(t), \qquad \Phi(0) = V(0) \tag{6.34}$$

Proof. According to Heisenberg's picture evolution equation we have

$$i\partial_t\hat{\psi}_\alpha(t) = \left[\hat{\psi}_\alpha(t), \hat{U}(t)^\dagger\hat{H}(t)\hat{U}(t)\right]. \tag{6.35}$$

Since $\hat{H}$ is quadratic in $\hat{\Psi}$, we know that $\hat{\psi}_\alpha(t)$ can be expanded in terms of the initial $\hat{\psi}$'s as

$$\hat{\psi}_\alpha(t) = \sum_\beta \zeta_{\alpha\beta}(t)\hat{\psi}_\beta, \tag{6.36}$$

or in matrix notation

$$\hat{\Psi}(t) = \zeta(t)\hat{\Psi}. \tag{6.37}$$

Notice that the unitarity of $\hat{U}$ imposes that the operators in $\hat{\Psi}(t)$ satisfy the same commutation algebra as the initial ones. In turn, this imposes unitarity on ζ. We can use Eq. (6.36) to write the commutator in Eq. (6.35) as

$$\left[\hat{\psi}_\kappa(t), \hat{U}(t)^\dagger\hat{H}(t)\hat{U}(t)\right] = \frac{1}{2}\sum_{\alpha\beta\mu\nu\lambda} H_{\alpha\beta}\zeta^*_{\alpha\mu}\zeta_{\beta\nu}\zeta_{\kappa\lambda}[\hat{\psi}_\lambda, \hat{\psi}_\mu^\dagger\hat{\psi}_\nu] \tag{6.38}$$

It is easy to check that

$$[\hat{\psi}_\lambda, \hat{\psi}^\dagger_\mu \hat{\psi}_\nu] = \hat{\psi}_\nu \delta_{\lambda,\mu} - \hat{\psi}^\dagger_\mu \delta_{\lambda,\mathcal{C}\nu}, \tag{6.39}$$

so we get

$$\begin{aligned}\left[\hat{\psi}_\kappa(t), \hat{U}(t)^\dagger \hat{H}(t) \hat{U}(t)\right] &= \frac{1}{2} \sum_{\alpha\beta\mu\nu} H_{\alpha\beta} \zeta^*_{\alpha\mu} \zeta_{\beta\nu} \zeta_{\kappa\mu} \hat{\psi}_\nu \\ &- \frac{1}{2} \sum_{\alpha\beta\mu\nu} H_{\alpha\beta} \zeta^*_{\alpha\mu} \zeta_{\beta\nu} \zeta_{\kappa\mathcal{C}\nu} \hat{\psi}^\dagger_\mu.\end{aligned} \tag{6.40}$$

Using $\hat{\psi}^\dagger_\mu = \hat{\psi}_{\mathcal{C}\mu}$ and relabeling in the last term we can rewrite

$$\begin{aligned}&\left[\hat{\psi}_\kappa(t), \hat{U}(t)^\dagger \hat{H}(t) \hat{U}(t)\right] = \\ &\frac{1}{2} \sum_{\alpha\beta\mu\nu} H_{\alpha\beta} \zeta^*_{\alpha\mu} \zeta_{\beta\nu} \zeta_{\kappa\mu} \hat{\psi}_\nu - \frac{1}{2} \sum_{\alpha\beta\mu\nu} H_{\alpha\beta} \zeta^*_{\alpha\mu} \zeta_{\beta\nu} \zeta_{\kappa,\mathcal{C}\nu} \hat{\psi}_{\mathcal{C}\mu} = \\ &\frac{1}{2} \sum_{\alpha\beta\mu\nu} H_{\alpha\beta} \zeta^*_{\alpha\mu} \zeta_{\beta\nu} \zeta_{\kappa\mu} \hat{\psi}_\nu - \frac{1}{2} \sum_{\alpha\beta\mu\nu} H_{\alpha\beta} \zeta^*_{\alpha,\mathcal{C}\nu} \zeta_{\beta,\mathcal{C}\mu} \zeta_{\kappa\mu} \hat{\psi}_\nu.\end{aligned} \tag{6.41}$$

Comparing with the left-hand side of Eq. (6.35) we can deduce that

$$i\partial_t \zeta_{\kappa\nu} = \frac{1}{2} \sum_{\alpha\beta\mu} H_{\alpha\beta} \zeta^*_{\alpha\mu} \zeta_{\beta\nu} \zeta_{\kappa\mu} - \frac{1}{2} \sum_{\alpha\beta\mu} H_{\alpha\beta} \zeta^*_{\alpha,\mathcal{C}\nu} \zeta_{\beta,\mathcal{C}\mu} \zeta_{\kappa\mu} \tag{6.42}$$

From $\hat{\psi}^\dagger_\alpha(t) = \psi_{\mathcal{C}\alpha}(t)$, we have $\zeta_{\alpha\beta} = \zeta^*_{\mathcal{C}\alpha,\mathcal{C}\beta}$ so the previous equation becomes

$$i\partial_t \zeta_{\kappa\nu} = \frac{1}{2} \sum_{\alpha\beta\mu} H_{\alpha\beta} \zeta^*_{\alpha\mu} \zeta_{\beta\nu} \zeta_{\kappa\mu} - \frac{1}{2} \sum_{\alpha\beta\mu} H_{\alpha\beta} \zeta_{\mathcal{C}\alpha,\nu} \zeta^*_{\mathcal{C}\beta,\mu} \zeta_{\kappa\mu} \tag{6.43}$$

The particle-hole symmetry of H ($\mathcal{C}H\mathcal{C} = -H$) can be expressed element-wise as $H_{\mathcal{C}\alpha,\mathcal{C}\beta} = -H_{\beta,\alpha}$. After some relabeling on the last term, this lets us rewrite the previous equation as

$$i\partial_t \zeta_{\kappa\nu} = \sum_{\alpha\beta\mu} H_{\alpha\beta} \zeta^*_{\alpha\mu} \zeta_{\beta\nu} \zeta_{\kappa\mu} \tag{6.44}$$

The unitarity of ζ implies $\sum_\mu \zeta^*_{\alpha\mu} \zeta_{\kappa\mu} = \delta_{\alpha\kappa}$ so the previous expression becomes

$$i\partial_t \zeta_{\alpha\beta} = \sum_{\mu} H_{\alpha\mu}\zeta_{\mu\beta} \tag{6.45}$$

or in matrix notation

$$i\partial_t \zeta = H\zeta, \qquad \zeta(0) = \mathbb{1} \tag{6.46}$$

Now notice that we can compose Eq. (6.36) with $\hat{\Psi} = V(0)\mathbf{d}$ and define $\Phi(t) = \zeta(t)V(0)$ that satisfies Eq. (6.33). Since $V(0)$ is time-independent, Eq. (6.34) follows immediately from Eq. (6.46). ☐

6.B. Parity

6.B.1. Time evolution of the parity operator

The parity operator is defined as:

$$\hat{P} = (-1)^{\sum_{\alpha=1}^{n} \hat{\psi}_\alpha^\dagger \hat{\psi}_\alpha} = \prod_{\alpha=1}^{n} \left(1 - 2\hat{\psi}_\alpha^\dagger \hat{\psi}_\alpha\right). \tag{6.47}$$

Since it commutes with $\hat{H}$, its ground state is an eigenstate of parity. This, together with the fact that the BdG operators switch the parity of a state, implies that we can also write down our parity operator in terms of them:

$$\hat{P} = p_\Omega \prod_{\alpha\in S^+}^{n} \left(1 - 2d_\alpha^\dagger d_\alpha\right) \tag{6.48}$$

where $p_\Omega = \pm 1$ stands for the parity of the ground state. In general, we can express the parity of a set of quasi-particle states S as

$$\hat{P}_S = \prod_{\alpha\in S} \left(1 - 2d_\alpha^\dagger d_\alpha\right) \tag{6.49}$$

The time evolution of this operator is given by substituting each d_α for $d_\alpha(t) = \hat{U}^\dagger d_\alpha \hat{U}$. From the results of App. 6.A.1, it is straightforward to obtain the expression of $d_\alpha(t)$ in terms of $\{d_\alpha\}_{\alpha\in S}$:

$$\hat{U}^\dagger \mathbf{d} \hat{U} = \hat{U}^\dagger V(0)^\dagger \hat{\Psi} \hat{U} = V(0)^\dagger \hat{\Psi}(t) = V(0)^\dagger \Phi(t)\mathbf{d} \tag{6.50}$$

Thus, if we define $\chi(t) = V(0)^\dagger \hat{\Psi}(t)$ we have

$$\hat{U}^\dagger d_\alpha \hat{U} = \sum_{\beta \in S} \chi(t)_{\alpha\beta} d_\beta \qquad \chi(t)_{\alpha\beta} = \langle \alpha | \beta(t) \rangle \tag{6.51}$$

We can expand the product in Eq. (6.49) and use Wick's theorem to obtain an expression for the time evolution of $\langle \hat{P}_S \rangle$

$$\langle \hat{P}_S(t) \rangle = \sum_{m=0}^{n_S} (-2)^m \sum_{\substack{0<\alpha_1 \\ <\ldots<\alpha_m}} \sum_{c \in C_m} (-1)^{s(c)} \prod_{k=1}^{m} \Theta^{X_k(c) Y_k(c)}_{\alpha_{i_k(c)} \alpha_{j_k(c)}} . \tag{6.52}$$

This formula contains several elements. First, we have a sum over all orders $0 < m < n_S$ (the term corresponding to $m = 0$ is equal to 1). For each order m we sum over all unordered choices of m states among n_S. For every such choice, we sum over all possible Wick contractions of that order (C_m denotes the set of all Wick contractions of order m). For some order m, each contraction (c denotes a specific contraction) in this sum results in a specific product of m numbers of the form $\Theta^{XY}_{\alpha\beta}$ defined as

$$\begin{aligned}
\Theta^{00}_{\alpha\beta} &= \sum_{\mu \in S^-} \chi^*_{\alpha,\mu} \chi_{\beta,\mu} \\
\Theta^{01}_{\alpha\beta} &= \sum_{\mu \in S^-} \chi^*_{\alpha,\mu} \chi^*_{\beta,\mathcal{C}\mu} \\
\Theta^{10}_{\alpha\beta} &= \sum_{\mu \in S^-} \chi_{\alpha,\mathcal{C}\mu} \chi_{\beta,\mu} = \Theta^{01*}_{\beta\alpha} \\
\Theta^{11}_{\alpha\beta} &= \sum_{\mu \in S^-} \chi_{\alpha,\mathcal{C}\mu} \chi^*_{\beta,\mathcal{C}\mu} = \delta_{\alpha\beta} - \Theta^{00*}_{\alpha\beta}
\end{aligned} \tag{6.53}$$

Each contraction c of order m corresponds to a permutation of the numbers $\{1, 2, \cdots, 2m\}$ under the following restriction: when the elements of the permutation are split in pairs $\{(a_k(c), b_k(c))\}_{k=1}^{m}$ they must satisfy $a_k(c) < b_k(c) \in \{1, \ldots, 2m\}$ and $a_1(c) < a_2(c) < \cdots < a_m(c)$. Each pair yields $i_k(c) = \lfloor (a_k(c)+1)/2 \rfloor$, $j_k(c) = \lfloor (b_k(c)+1)/2 \rfloor$, $X_k(c) = (a_k(c)+1) \bmod 2$ and $Y_k(c) = b_k(c) \bmod 2$. The overall sign $s(c)$ is the sign of the permutation. It is possible to write a script that procedurally generates all valid permutations and calculates the indices $X_k(c)$, $Y_k(c)$, $\alpha_{i_k(c)}$ and $\alpha_{j_k(c)}$ corresponding to every contraction c.

6.B.2. Convergence of parity

The amount of terms in equation Eq. (6.52) is

$$1 + \sum_{m=1}^{n_S} \binom{n_S}{m} (2m-1)!!. \tag{6.54}$$

This number is out of reach in practice, so we are forced to truncate the sums. It was checked that restricting ourselves to order $m_{\text{max}} = 4$ is sufficient to get an accurate result. In addition, the operator $\langle P' \rangle$ defined in 6.14 in principle contains $n_S = n - 1$ Bogoliubov operators, but in practice we must truncate the product to a maximum number of states n_{max}, or equivalently, a cut-off energy E_{max}. In Sec. 6.3.2, we have argued that it is necessary to keep $E_{\text{max}} < \Delta_{\text{J}}$ so that $\langle \hat{P}' \rangle$ represents the parity of the edges. This is true for the case where $vt_{\text{inj}}/W = 2.3$ studied in Sec. 6.3. We show this explicitly in Fig. 6.11, where convergence is reached approximately at $0.85\Delta_{\text{J}}$, ensuring that no junction states participate in the calculation of the parity. We also show a few other cases with smaller values of vt_{inj}/W. For these values, convergence of parity requires including up to 35 states with energies above Δ_{J}. In this case the calculation includes the hybridized edge and bound states of the junction, which does not allow us to isolate the edge parity sector from the junction.

6.C. Supplemental results

In this section, we present the results of our simulation for variable quenching times, supplementing the results in the main text.

6.C.1. Local representation of observables

The calculations of current and quasi-particle number made in the main text have been integrated over specific areas. Here we show a few snapshots of the local current density and the local excitation density for two values of vt_{inj}/W (left and right panels of Fig. 6.12). We show three different times in which the injection and fusion can be observed.

In the left panels, for long injections, the excitation entirely leaves the junction. In the right panel (which corresponds with Fig. 6.8), the excitation density slowly decays from the junction, at times even after $t > \tau = 50a/v$ when the quench is over.

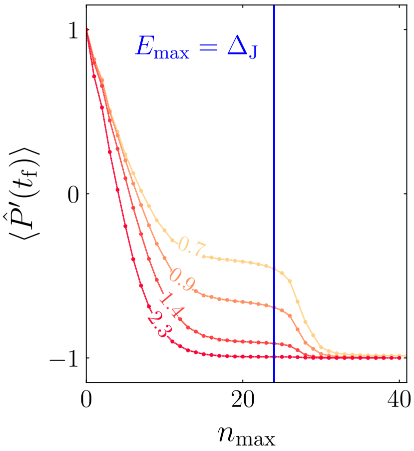

Figure 6.11: Convergence of the parity sector $\hat{P}'$ at final time $t_{\rm f}$ as a function of the index $n_{\rm max}$ which counts the number of eigenstates included in the calculation. This is done for different values of $vt_{\rm inj}/W$ which are displayed on the curves. For energies above $E_{\rm max} = \Delta_{\rm J}$, the hybridized edge-junction states are necessary in the convergence of the operator.

The current density is zero in the superconducting region as the Majorana fermions are chargeless. Only upon fusion, the excitations produce charge. Here, the charge production at short injection times is much smaller, which is shown quantitatively in the next part. It is worth noting that while the excitations can remain trapped in the junction, they do not carry charge.

6.C.2. Current density in the long junction regime

For completeness, we include the calculations of charge at the exit for the different quenching times. In Fig. 6.13 we show the excitation spectrum, quasi-particle number, current and charge for different values of $vt_{\rm inj}/W$ discussed in Sec. 6.4. We can see how the the occupancy of the junction increases when the injection time becomes shorter.

As the contribution of the excitations in the junction became sufficient the predictions for quantized charge are no longer valid. This can be seen in the bottom part of Fig. 6.13 charge is no longer quantized. In the cases $vt_{\rm inj}/W = 0.1, 0.2$, not only the lowest mode but also the next higher mode of the junction is populated by excitations. Additionally as shown in Fig. 6.12, a fast injection causes a large path-length difference as the

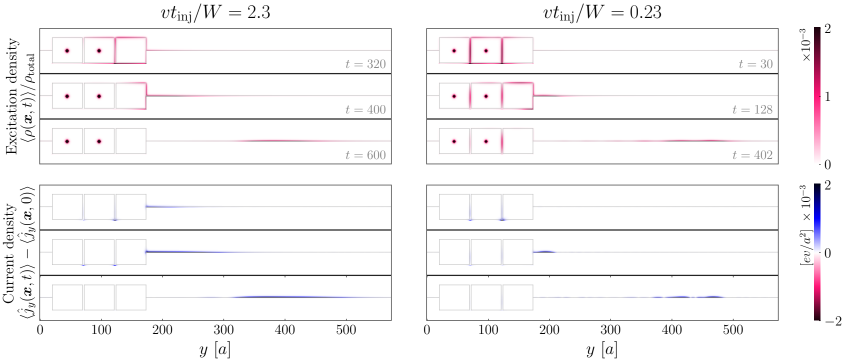

Figure 6.12: Three snapshots of the braiding protocol for two values of vt_{inj}/W (left column and right column). the top panel shows the snapshots in terms of the local excitation density, and the bottom panel shows them in terms of the local current density.

junction traps the excitations and leaks them into the top and bottom edges at different rates. This results in further interference effects upon fusion.

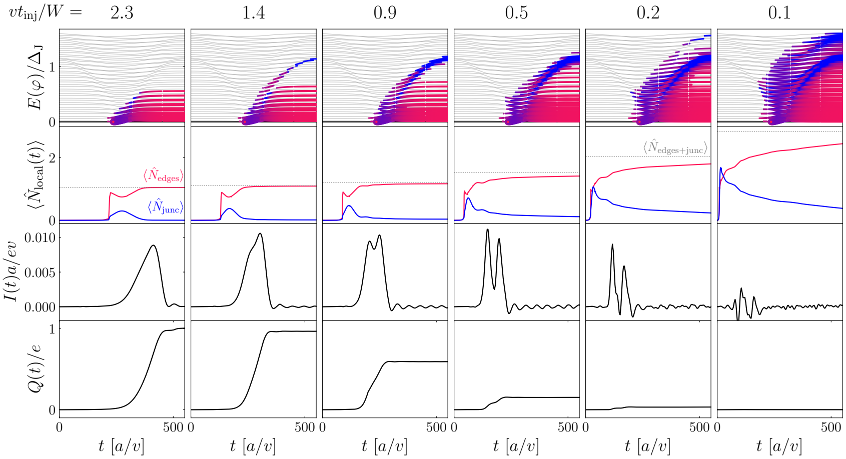

Figure 6.13: First row: Quasi-particle occupation of the energy levels (thick colored lines). The color of the lines distinguishes between junction (blue) and edge (red) states. Second row: Quasi-particle number in the junction (blue), edges (red) and their sum at final value (gray dashed line). Third row: Current at the exit of the superconductor. Fourth row: Net charge creation at the exit of the superconductor.

Bibliography

[1] P. R. Wallace. The band theory of graphite. *Phys. Rev.*, **71**, 622–634 (1947).

[2] K. S. Novoselov, A. K. Geim, S. V. Morozov, D. Jiang, M. I. Katsnelson, I. V. Grigorieva, S. V. Dubonos & A. A. Firsov. Two-dimensional gas of massless Dirac fermions in graphene. *Nature*, **438**, 197–200 (2005).

[3] H. Nielsen & M. Ninomiya. A no-go theorem for regularizing chiral fermions. *Phys. Lett. B*, **105**, 219–223 (1981).

[4] D. B. Kaplan. A method for simulating chiral fermions on the lattice. *Physics Letters B*, **288**, 342–347 (1992).

[5] Y. Shamir. Chiral fermions from lattice boundaries. *Nuclear Physics B*, **406**, 90–106 (1993).

[6] H. Neuberger. Exactly massless quarks on the lattice. *Physics Letters B*, **417**, 141–144 (1998).

[7] H. Neuberger. More about exactly massless quarks on the lattice. *Physics Letters B*, **427**, 353–355 (1998).

[8] R. Stacey. Eliminating lattice fermion doubling. *Phys. Rev. D*, **26**, 468–472 (1982).

[9] C. Le, Z. Yang, F. Cui, A. P. Schnyder & C.-K. Chiu. Generalized fermion doubling theorems: Classification of two-dimensional nodal systems in terms of wallpaper groups. *Phys. Rev. B*, **106**, 045126 (2022).

[10] H. Tasaki. Physics and mathematics of quantum many-body systems. *Springer* (2020).

[11] K. G. Wilson. Confinement of quarks. *Phys. Rev. D*, **10**, 2445–2459 (1974).

[12] L. Susskind. Lattice fermions. *Phys. Rev. D*, **16**, 3031–3039 (1977).

[13] S. D. Drell, M. Weinstein & S. Yankielowicz. Strong-coupling field theories. II. fermions and gauge fields on a lattice. *Phys. Rev. D*, **14**, 1627–1647 (1976).

[14] P. H. Ginsparg & K. G. Wilson. A remnant of chiral symmetry on the lattice. *Phys. Rev. D*, **25**, 2649–2657 (1982).

[15] S. Hong, V. Diep, S. Datta & Y. P. Chen. Modeling potentiometric measurements in topological insulators including parallel channels. *Phys. Rev. B*, **86**, 085131 (2012).

[16] K. M. M. Habib, R. N. Sajjad & A. W. Ghosh. Chiral tunneling of topological states: Towards the efficient generation of spin current using spin-momentum locking. *Phys. Rev. Lett.*, **114**, 176801 (2015).

[17] B. Messias de Resende, F. C. de Lima, R. H. Miwa, E. Vernek & G. J. Ferreira. Confinement and fermion doubling problem in dirac-like hamiltonians. *Phys. Rev. B*, **96**, 161113 (2017).

[18] A. L. Araújo, R. P. Maciel, R. G. F. Dornelas, D. Varjas & G. J. Ferreira. Interplay between boundary conditions and wilson's mass in dirac-like hamiltonians. *Phys. Rev. B*, **100**, 205111 (2019).

[19] J. Kogut & L. Susskind. Hamiltonian formulation of Wilson's lattice gauge theories. *Phys. Rev. D*, **11**, 395–408 (1975).

[20] J. P. Costella. A new proposal for the fermion doubling problem, arXiv:hep-lat/0207008 (2002).

[21] Z.-X. Li, A. Vaezi, C. B. Mendl & H. Yao. Numerical observation of emergent spacetime supersymmetry at quantum criticality. *Science Adv.*, **4**, eaau1463 (2018).

[22] T. C. Lang & A. M. Läuchli. Quantum Monte Carlo simulation of the chiral Heisenberg Gross-Neveu-Yukawa phase transition with a single Dirac cone. *Phys. Rev. Lett.*, **123**, 137602 (2019).

[23] Y. Da Liao, X. Y. Xu, Z. Y. Meng & Y. Qi. Caution on Gross-Neveu criticality with a single Dirac cone: Violation of locality and its consequence of unexpected finite-temperature transition. *Phys. Rev. B*, **108**, 195112 (2023).

[24] Z. Wang, F. Assaad & M. Ulybyshev. Validity of slac fermions for the (1+1)-dimensional helical luttinger liquid. *Phys. Rev. B*, **108**, 045105 (2023).

[25] C. M. Bender, K. A. Milton & D. H. Sharp. Consistent formulation of fermions on a Minkowski lattice. *Phys. Rev. Lett.*, **51**, 1815–1818 (1983).

[26] M. J. Pacholski, G. Lemut, J. Tworzydło & C. W. J. Beenakker. Generalized eigenproblem without fermion doubling for Dirac fermions on a lattice. *SciPost Phys.*, **11**, 105 (2021).

[27] L. Fu & C. L. Kane. Superconducting proximity effect and Majorana Fermions at the surface of a topological insulator. *Phys. Rev. Lett.*, **100**, 096407 (2008).

[28] C. Kallin & J. Berlinsky. Chiral superconductors. *Rep. Prog. Phys.*, **79**, 054502 (2016).

[29] Z. Zhu, M. Papaj, X.-A. Nie, H.-K. Xu, Y.-S. Gu, X. Yang et al. Discovery of segmented Fermi surface induced by Cooper pair momentum. *Science*, **374**, 1381–1385 (2021).

[30] G. E. Volovik. Quantum phase transitions from topology in momentum space. *Lect. Notes Phys.*, **718**, 31–73 (2007).

[31] C. W. J. Beenakker. Bogoliubov Fermi surface revealed. *J. C. Cond. Matt. Phys.* (2020).

[32] S. Rao. Introduction to non-abelian anyons. *arXiv:1610.09260* (2016).

[33] A. Kitaev. Fault-tolerant quantum computation by anyons. *Ann. Phys.*, **303**, 2–30 (2003).

[34] N. Read & G. Moore. Fractional Quantum Hall Effect and Nonabelian Statistics. *Prog. Theor. Phys. Supp.*, **107**, 157–166 (1992).

[35] R. L. Willett, C. Nayak, K. Shtengel, L. N. Pfeiffer & K. W. West. Magnetic-field-tuned Aharonov-Bohm oscillations and evidence for non-abelian anyons at $\nu = 5/2$. *Phys. Rev. Lett.*, **111**, 186401 (2013).

[36] C. W. J. Beenakker. Search for non-Abelian Majorana braiding statistics in superconductors. *SciPost Phys. Lect. Notes*, page 15 (2020).

[37] P. Fendley, M. P. A. Fisher & C. Nayak. Edge states and tunneling of non-Abelian quasiparticles in the $\nu = 5/2$ quantum Hall state and $p + ip$ superconductors. *Phys. Rev. B*, **75**, 045317 (2007).

[38] C. W. J. Beenakker, P. Baireuther, Y. Herasymenko, I. Adagideli, L. Wang & A. R. Akhmerov. Deterministic creation and braiding of chiral edge vortices. *Phys. Rev. Lett.*, **122**, 146803 (2019).

[39] M. Z. Hasan & C. L. Kane. Topological insulators. *Rev. Mod. Phys.*, **82**, 3045–3067 (2010).

[40] X.-L. Qi & S.-C. Zhang. Topological insulators and superconductors. *Rev. Mod. Phys.*, **83**, 1057–1110 (2011).

[41] C. L. Kane. Topological band theory and the $\mathbb{Z}_2$ invariant. *Contemporary Concepts of Condensed Matter Science*, **6**, 3–34 (2013).

[42] J. W. Braun, Q. Su & R. Grobe. Numerical approach to solve the time-dependent Dirac equation. *Phys. Rev. A*, **59**, 604–612 (1999).

[43] P. Krekora, Q. Su & R. Grobe. Klein paradox in spatial and temporal resolution. *Phys. Rev. Lett.*, **92**, 040406 (2004).

[44] G. R. Mocken & C. H. Keitel. FFT-split-operator code for solving the Dirac equation in 2+1 dimensions. *Comp. Phys. Comm.*, **178**, 868–882 (2008).

[45] F. Fillion-Gourdeau, E. Lorin & A. D. Bandrauk. Numerical solution of the time-dependent Dirac equation in coordinate space without fermion-doubling. *Comp. Phys. Comm.*, **183**, 1403–1415 (2012).

[46] J. Tworzydło, C. W. Groth & C. W. J. Beenakker. Finite difference method for transport properties of massless Dirac fermions. *Phys. Rev. B*, **78**, 235438 (2008).

[47] M. Suzuki. Fractal decomposition of exponential operators with applications to many-body theories and Monte Carlo simulations. *Phys. Lett. A*, **146**, 319–323 (1990).

[48] N. Watanabe & M. Tsukada. Fast and stable method for simulating quantum electron dynamics. *Phys. Rev. E*, **62**, 2914–2923 (2000).

[49] A. Chaves, L. Covaci, K. Y. Rakhimov, G. A. Farias & F. M. Peeters. Wave-packet dynamics and valley filter in strained graphene. *Phys. Rev. B*, **82**, 205430 (2010).

[50] K. Mochizuki, T. Bessho, M. Sato & H. Obuse. Topological quantum walk with discrete time-glide symmetry. *Phys. Rev. B*, **102**, 035418 (2020).

[51] S. Ryu, A. P. Schnyder, A. Furusaki & A. W. W. Ludwig. Topological insulators and superconductors: tenfold way and dimensional hierarchy. *New J. Phys*, **12**, 065010 (2010).

[52] C. Roiesnel. Definition of the covariant lattice Dirac operator. *Phys. Rev. D*, **87**, 074505 (2013).

[53] A. D. Vela, G. Lemut, M. J. Pacholski, J. Tworzydło & C. W. J. Beenakker. Reflectionless Klein tunneling of Dirac fermions: Comparison of split-operator and staggered-lattice discretization of the Dirac equation. *J. Phys. Cond. Matt.*, **34**, 364003 (2022).

[54] A. George. Nested dissection of a regular finite element mesh. *SIAM J. Numer. Anal.*, **10**, 345–363 (1973).

[55] A. George & E. Ng. On the complexity of sparse *QR* and *LU* factorization of finite-element matrices. *SIAM J. Sci. Stat. Comput.*, **9**, 849–861 (1988).

[56] X. S. Li & J. W. Demmel. SuperLU_DIST: A scalable distributed-memory sparse direct solver for unsymmetric linear systems. *ACM Trans. Math. Softw.*, **29**, 110–140 (2003).

[57] P. E. Allain & J. N. Fuchs. Klein tunneling in graphene: optics with massless electrons. *Eur. Phys. J. B*, **83**, 301 (2011).

[58] C. W. J. Beenakker. Andreev reflection and Klein tunneling in graphene. *Rev. Mod. Phys.*, **80**, 1337–1354 (2008).

[59] O. Vafek & A. Vishwanath. Dirac fermions in solids: From high-T_c cuprates and graphene to topological insulators and Weyl semimetals. *Ann. Rev. Cond. Matt. Phys.*, **5**, 83–112 (2014).

[60] T. Kimura. Domain-wall, overlap, and topological insulators, arXiv:1511.08286 (2015).

[61] R. Hammer, W. Pötz & A. Arnold. Single-cone real-space finite difference scheme for the time-dependent Dirac equation. *J. Comp. Phys.*, **265**, 50–70 (2014).

[62] W. Pötz. Single-cone finite-difference schemes for the (2+1)-dimensional Dirac equation in general electromagnetic textures. *Phys. Rev. E*, **96**, 053312 (2017).

[63] A. Donís Vela, M. J. Pacholski, G. Lemut, J. Tworzydło & C. W. J. Beenakker. Massless Dirac fermions on a space-time lattice with a topologically protected Dirac cone. *Ann. Phys. (Berl.)*, **534**, 2200206 (2022).

[64] R. Hammer & W. Pötz. Dynamics of domain-wall Dirac fermions on a topological insulator: A chiral fermion beam splitter. *Phys. Rev. B*, **88**, 235119 (2013).

[65] W. Pötz & R. Hammer. Chiral fermion dynamics in 2d magnetic vortices: Manifestation of momentum-spin-locking. *J. Appl. Phys.*, **120**, 193903 (2016).

[66] W. Pötz & M. Schreilechner. Single-cone finite difference scheme for the (2+1)D Dirac von Neumann equation. *J. Comp. Phys.*, **348**, 591–611 (2017).

[67] W. Pötz. Perfectly matched layers for the Dirac equation in general electromagnetic texture. *Phys. Rev. E*, **103**, 013301 (2021).

[68] R. Hammer & W. Pötz. Staggered grid leap-frog scheme for the (2+1)D Dirac equation. *Comp. Phys. Comm.*, **185**, 40–52 (2014).

[69] R. Stacey. Gauge invariance and fermion doubling on the lattice. *Z. Phys. C*, **19**, 75–78 (1983).

[70] C. J. Griffin & T. D. Kieu. Fermion doubling and gauge invariance on random lattices. *Phys. Rev. Lett.*, **70**, 3844–3847 (1993).

[71] D. Tong. Lattice gauge theory, lecture notes at `https://www.damtp.cam.ac.uk/user/tong/gaugetheory.html` (2018).

[72] B. A. Bernevig & T. L. Hughes. Topological Insulators and Topological Superconductors. *Princeton* (2013).

[73] I. I. Rabi. Das freie Elektron im homogenen Magnetfeld nach der Diracschen Theorie. *Z. Physik*, **49**, 507–511 (1928).

[74] J. W. McClure. Diamagnetism of graphite. *Phys. Rev.*, **104**, 666–671 (1956).

[75] P. Cheng, C. Song, T. Zhang, Y. Zhang, Y. Wang, J.-F. Jia et al. Landau quantization of topological surface states in $\mathrm{Bi_2Se_3}$. *Phys. Rev. Lett.*, **105**, 076801 (2010).

[76] T. Hanaguri, K. Igarashi, M. Kawamura, H. Takagi & T. Sasagawa. Momentum-resolved Landau-level spectroscopy of Dirac surface state in $\mathrm{Bi_2Se_3}$. *Phys. Rev. B*, **82**, 081305 (2010).

[77] Y. Jiang, Y. Wang, M. Chen, Z. Li, C. Song, K. He, L. Wang, X. Chen, X. Ma & Q.-K. Xue. Landau quantization and the thickness limit of topological insulator thin films of $\mathrm{Sb_2Te_3}$. *Phys. Rev. Lett.*, **108**, 016401 (2012).

[78] S. K. Chong, R. Tsuchikawa, J. Harmer, T. D. Sparks & V. V. Deshpande. Landau levels of topologically-protected surface states probed by dual-gated quantum capacitance. *ACS Nano*, **14**, 1158–1165 (2020).

[79] A. J. M. Giesbers, U. Zeitler, M. I. Katsnelson, L. A. Ponomarenko, T. M. Mohiuddin & J. C. Maan. Quantum-Hall activation gaps in graphene. *Phys. Rev. Lett.*, **99**, 206803 (2007).

[80] C.-K. Chiu, J. C. Y. Teo, A. P. Schnyder & S. Ryu. Classification of topological quantum matter with symmetries. *Rev. Mod. Phys.*, **88**, 035005 (2016).

[81] Y. Aharonov & A. Casher. Ground state of a spin-1/2 charged particle in a two-dimensional magnetic field. *Phys. Rev. A*, **19**, 2461–2462 (1979).

[82] L. Alvarez-Gaumé. Supersymmetry and the Atiyah-Singer index theorem. *Comm. Math. Phys.*, **90**, 161–173 (1983).

[83] M. I. Katsnelson. Graphene — Carbon in two dimensions. *Cambridge* (2012).

[84] F. Bruckmann, G. Endrődi, M. Giordano, S. D. Katz, T. G. Kovács, F. Pittler & J. Wellnhofer. Landau levels in QCD. *Phys. Rev. D*, **96**, 074506 (2017).

[85] G. S. Bali, B. B. Brandt, G. Endrődi & B. Glässle. Meson masses in electromagnetic fields with Wilson fermions. *Phys. Rev. D*, **97**, 034505 (2018).

[86] C. W. J. Beenakker & L. Kouwenhoven. A road to reality with topological superconductors. *Nature Phys.*, **12**, 618–621 (2016).

[87] M. Sato & Y. Ando. Topological superconductors: a review. *Rep. Prog. Phys.*, **80**, 076501 (2017).

[88] N. Read & D. Green. Paired states of fermions in two dimensions with breaking of parity and time-reversal symmetries and the fractional quantum Hall effect. *Phys. Rev. B*, **61**, 10267–10297 (2000).

[89] A. P. Mackenzie, T. Scaffidi, C. W. Hicks & Y. Maeno. Even odder after twenty-three years: the superconducting order parameter puzzle of Sr_2RuO_4. *npj Quantum Materials*, **2**, 40 (2017).

[90] M. Kayyalha, D. Xiao, R. Zhang, J. Shin, J. Jiang, F. Wang et al. Absence of evidence for chiral Majorana modes in quantum anomalous Hall-superconductor devices. *Science*, **367**, 64–67 (2020).

[91] M. Tinkham. Introduction to Superconductivity. *Dover Publications* (2004).

[92] N. F. Q. Yuan & L. Fu. Zeeman-induced gapless superconductivity with a partial Fermi surface. *Phys. Rev. B*, **97**, 115139 (2018).

[93] M. Papaj & L. Fu. Creating Majorana modes from segmented Fermi surface. *Nature Comm.*, **12**, 577 (2021).

[94] M. J. Pacholski, G. Lemut, O. Ovdat, i. d. I. Adagideli & C. W. J. Beenakker. Deconfinement of Majorana vortex modes produces a superconducting Landau level. *Phys. Rev. Lett.*, **126**, 226801 (2021).

[95] T. Yokoyama, C. Iniotakis, Y. Tanaka & M. Sigrist. Chirality sensitive effect on surface states in chiral p-wave superconductors. *Phys. Rev. Lett.*, **100**, 177002 (2008).

[96] I. Seroussi, E. Berg & Y. Oreg. Topological superconducting phases of weakly coupled quantum wires. *Phys. Rev. B*, **89**, 104523 (2014).

[97] C. W. Groth, M. Wimmer, A. R. Akhmerov & X. Waintal. Kwant: a software package for quantum transport. *New J. Phys.*, **16**, 063065 (2014).

[98] G. Lemut, M. J. Pacholski, i. d. I. Adagideli & C. W. J. Beenakker. Effect of charge renormalization on the electric and thermoelectric transport along the vortex lattice of a Weyl superconductor. *Phys. Rev. B*, **100**, 035417 (2019).

[99] A. Yamakage, Y. Tanaka & N. Nagaosa. Evolution of edge states and critical phenomena in the rashba superconductor with magnetization. *Phys. Rev. Lett.*, **108**, 087003 (2012).

[100] D. A. Ivanov. Non-Abelian statistics of half-quantum vortices in p-wave superconductors. *Phys. Rev. Lett.*, **86**, 268 (2001).

[101] C. Nayak, S. H. Simon, A. Stern, M. Freedman & S. Das Sarma. Non-Abelian anyons and topological quantum computation. *Rev. Mod. Phys.*, **80**, 1083–1159 (2008).

[102] S. D. Sarma, M. Freedman & C. Nayak. Majorana zero modes and topological quantum computation. *npj Quantum Information*, **1**, 15001 (2015).

[103] J.-P. Xu, C. Liu, M.-X. Wang, J. Ge, Z.-L. Liu, X. Yang et al. Artificial topological superconductor by the proximity effect. *Phys. Rev. Lett.*, **112**, 217001 (2014).

[104] X. Ma, C. J. O. Reichhardt & C. Reichhardt. Braiding Majorana fermions and creating quantum logic gates with vortices on a periodic pinning structure. *Phys. Rev. B*, **101**, 024514 (2020).

[105] H.-Y. Ma, D. Guan, S. Wang, Y. Li, C. Liu, H. Zheng & J.-F. Jia. Braiding Majorana zero mode in an electrically controllable way. *J. Phys. D*, **54**, 424003 (2021).

[106] V. Vlasko-Vlasov, A. Rydh, R. Divan, D. Rosenmann, A. Glatz & W.-K. Kwok. Magnetic circuit for Abrikosov vortices: Vortex motion in a periodic labyrinth of magnetic T and I-shaped elements under a superconducting film. *J. Magn. Magn. Mater.*, **557**, 169476 (2022).

[107] I. Adagideli, F. Hassler, A. Grabsch, M. Pacholski & C. W. J. Beenakker. Time-resolved electrical detection of chiral edge vortex braiding. *SciPost Phys.*, **8**, 013 (2020).

[108] F. Hassler, A. Grabsch, M. J. Pacholski, D. O. Oriekhov, O. Ovdat, I. Adagideli & C. W. J. Beenakker. Half-integer charge injection by a Josephson junction without excess noise. *Phys. Rev. B*, **102**, 045431 (2020).

[109] A. Nag & J. D. Sau. Diabatic errors in Majorana braiding with bosonic bath. *Phys. Rev. B*, **100**, 014511 (2019).

[110] M. Sekania, S. Plugge, M. Greiter, R. Thomale & P. Schmitteckert. Braiding errors in interacting Majorana quantum wires. *Phys. Rev. B*, **96**, 094307 (2017).

[111] J. Fu. Majorana orthogonal transformation and Majorana zero modes in free fermionic systems. *Ann. Phys.*, **432**, 168564 (2021).

[112] M. Cheng, R. M. Lutchyn, V. Galitski & S. Das Sarma. Splitting of Majorana-fermion modes due to intervortex tunneling in a $p_x + ip_y$ superconductor. *Phys. Rev. Lett.*, **103**, 107001 (2009).

[113] C.-X. Liu, S.-C. Zhang & X.-L. Qi. The quantum anomalous Hall effect: Theory and experiment. *Annu. Rev. Condens. Matter Phys.*, **7**, 301–321 (2016).

[114] X. Kou, L. Pan, J. Wang, Y. Fan, E. S. Choi, W.-L. Lee et al. Metal-to-insulator switching in quantum anomalous Hall states. *Nature Comm.*, **6**, 8474 (2015).

[115] Y. Feng, X. Feng, Y. Ou, J. Wang, C. Liu, L. Zhang et al. Observation of the zero Hall plateau in a quantum anomalous Hall insulator. *Phys. Rev. Lett.*, **115**, 126801 (2015).

[116] X.-L. Qi, T. L. Hughes & S.-C. Zhang. Chiral topological superconductor from the quantum Hall state. *Phys. Rev. B*, **82**, 184516 (2010).

[117] J. Wang, Q. Zhou, B. Lian & S.-C. Zhang. Chiral topological superconductor and half-integer conductance plateau from quantum anomalous Hall plateau transition. *Phys. Rev. B*, **92**, 064520 (2015).

[118] L. Fu & C. L. Kane. Superconducting proximity effect and Majorana fermions at the surface of a topological insulator. *Phys. Rev. Lett.*, **100**, 096407 (2008).

[119] E. Grosfeld & A. Stern. Observing Majorana bound states of Josephson vortices in topological superconductors. *PNAS*, **108**, 11810–11814 (2011).

[120] T. Kloss, J. Weston, B. Gaury, B. Rossignol, C. Groth & X. Waintal. Tkwant: a software package for time-dependent quantum transport. *New J. Phys.*, **23**, 023025 (2021).

[121] J. Weston & X. Waintal. Towards realistic time-resolved simulations of quantum devices. *J. Comput. Electron.*, **15**, 1148–1157 (2016).

[122] T. Bautze, C. Süssmeier, S. Takada, C. Groth, T. Meunier, M. Yamamoto, S. Tarucha, X. Waintal & C. Bäuerle. Theoretical, numerical, and experimental study of a flying qubit electronic interferometer. *Phys. Rev. B*, **89**, 125432 (2014).

[123] B. Rossignol, T. Kloss, P. Armagnat & X. Waintal. Toward flying qubit spectroscopy. *Phys. Rev. B*, **98**, 205302 (2018).

Samenvatting

Paul Dirac bedacht de vergelijking die de beweging van een relativistisch deeltje in vacuüm beschrijft. Bij lage energieën vereenvoudigt de Diracvergelijking tot de Schrödingervergelijking omdat de relativistische effecten wegvallen. Aangezien de fysica van de gecondenseerde materie de elektronen bestudeert bij zeer lage energieën, is de Schrödingervergelijking meestal toereikend. Er is echter een geval waarin deze vereenvoudiging niet opgaat. Als het deeltje massaloos is, verschilt de Diracvergelijking kwalitatief van de Schrödingervergelijking, hoe laag de energie ook is. Met andere woorden, de massaloze Diracvergelijking is nog steeds zinvol, terwijl er niet zoiets bestaat als de "massaloze Schrödingervergelijking". In sommige systemen, zoals het oppervlak van een drie-dimensionale topologische isolator, zijn de elektronen effectief massaloos en moeten we noodzakelijkerwijs de massaloze Diracvergelijking gebruiken om ze te beschrijven.

Een handige manier om deze vergelijkingen numeriek op te lossen is door ze te discretiseren. Hiermee bedoelen we dat we een rooster over de ruimte — en mogelijk ook de tijd — leggen en het deeltje alleen op de punten van dit rooster laten bestaan. Als we dit doen, worden de differentiaaloperatoren verschiloperatoren en dit stelt ons in staat om onze differentiaalvergelijking om te zetten in een algebraïsche vergelijking die gemakkelijk door een computer kan worden opgelost. Als men dit zorgvuldig doet, benadert de oplossing van de discrete versie de continue mits het rooster fijn genoeg is.

In tegenstelling tot de Schrödingervergelijking kan de Diracvergelijking niet eenvoudigweg gediscretiseerd worden. De stelling van Nielsen-

Ninomiya zegt dat er bij een naïeve discretizatie extra niet-fysische massaloze fermionen verschijnen, die aanleiding geven tot een aantal ongewenste artefacten. Dit staat bekend als *fermionverdubbeling*, en het centrale doel van dit proefschrift is om dit probleem aan te pakken via de discretisatiemethode van *tangens-fermionen*.

De hoofdstukken 2, 3 en 4 zijn gewijd aan de ontwikkeling van verschillende aspecten van deze methode. In hoofdstuk 2 introduceren we een manier om de Diracvergelijking op te lossen voor massaloze fermionen in een ruimte-tijd rooster. We laten zien dat deze methode bijzonder is omdat het fermionverdubbeling vermijdt en de topologische bescherming van de Dirac-kegel behoudt.

In hoofdstuk 3 wordt deze aanpak gebruikt om de dynamica te simuleren van een massaloos elektron dat naar een potentiële barrière beweegt. De theorie voorspelt dat massaloze deeltjes niet tegengehouden kunnen worden door de barrière, dit fenomeen staat bekend als Klein-tunnelen. In tegenstelling tot andere methodes kan onze methode het effect met grote nauwkeurigheid reproduceren.

In hoofdstuk 4 breiden we de tangens-fermionen methode uit om rekening te houden met het effect van magnetische velden op massaloze fermionen. We laten zien hoe onze benadering de verbreding van het nulde Landauniveau in aanwezigheid van magnetische wanorde voorkomt, een artefact dat anders ontstaat door fermionverdubbeling.

De hoofdstukken 5 en 6 zijn niet direct gerelateerd aan de methode van tangens-fermionen, maar beschrijven wel processen die optreden in materialen met een Dirac-achtige dispersierelatie. In hoofdstuk 5 bestuderen we het effect van een niet-nul netto superstroom parallel aan de randen van een topologische supergeleider. We vinden dat de superstroom een “chiraliteitsinversie” kan induceren van de Majorana-randmodes die in dit systeem bestaan.

In het laatste hoofdstuk simuleren we numeriek de injectie van “randwervelingen” in de randen van een topologische supergeleider. Dit zijn een soort quasideeltjes die theoretisch gebruikt kunnen worden om een fouttolerante quantumcomputer te realiseren.

Summary

Paul Dirac came up with the equation that describes the motion of a relativistic particle in vacuum. At low energies, the Dirac equation simplifies to the Schrödinger equation because the relativistic effects fade away. Since condensed matter physics studies electrons at very low energies, the Schrödinger equation is adequate for it most of the time. However, there is a case in which this simplification breaks down. If the particle is massless, the Dirac equation is qualitatively different from the Schrödinger equation no matter how low the energy is. In other words, the massless Dirac equation is still meaningful, while there is no such thing as the "massless Schrödinger equation". In some condensed matter systems, such as the surface of a 3D topological insulator, the electrons are effectively massless and we must necessarily use the massless Dirac equation to describe them.

A very convenient way to numerically solve these equations is to discretise them. By this we mean to lay a lattice over space — and possibly also time — and only allow the particle to exist on the points of this lattice. When we do this, differential operators become finite difference ones and this allows us to transform our differential equation into an algebraic one that can be readily solved by a computer. If one does this carefully, the solution of the discrete version approximates the continuous one if the lattice is fine enough.

Unlike the Schrödinger equation, the Dirac equation cannot be trivially discretised. The Nielsen-Ninomiya theorem proves that if we try to do it naively, extra unphysical massless fermion species appear, giving rise to a number of undesired artefacts. This is known as *fermion doubling*, and the main focus of this thesis is to tackle this problem via the discretisation method of *tangent fermions*.

Chapters 2, 3 and 4 are devoted to developing various aspects of this method. In chapter 2, we introduce a way to use it to solve the Dirac equation for massless fermions in a space-time lattice. We show that this method is unique in that it avoids fermion doubling and preserves the topological protection of the Dirac cone.

In chapter 3, this approach is used to simulate the dynamics of a massless electron that moves towards a potential barrier. Theory predicts that massless particles cannot be stopped by the barrier, this phenomenon is known as Klein tunneling. We contrast our method with others and show that it reproduces the effect with excellent accuracy.

In chapter 4, we extend the tangent fermions method to account for the effect of magnetic fields on massless fermions. We show how our approach prevents the broadening of the zeroth Landau level in presence of magnetic disorder, an artefact that otherwise arises due to fermion doubling.

Chapters 5 and 6 are not directly related to the method of tangent fermions but still describe processes that arise in materials with a Dirac-like dispersion relation. In chapter 5, we study the effect a non-zero net supercurrent parallel to the edges of a topological superconductor. We find that the supercurrent can induce a “chirality inversion” of the Majorana edge modes that exist in this system.

In the last chapter, we numerically simulate the injection of “edge-vortices” into the edges of a topological superconductor. These are a type of quasiparticles that can theoretically be used to realise a fault tolerant quantum computer.

Resumen

Paul Dirac ideó la ecuación que describe el movimiento de una partícula relativista en el vacío. A bajas energías, la ecuación de Dirac se simplifica en la ecuación de Schrödinger porque los efectos relativistas se desvanecen. Dado que la física de la materia condensada estudia electrones a muy bajas energías, la ecuación de Schrödinger es adecuada en la mayoría de las ocasiones. Sin embargo, hay un caso en el que esta simplificación falla. Si la partícula no tiene masa, la ecuación de Dirac es cualitativamente diferente de la ecuación de Schrödinger independientemente de lo baja que sea la energía. En otras palabras, la ecuación de Dirac sin masa sigue teniendo sentido, pero no existe tal cosa como la “ecuación de Schrödinger sin masa”. En algunos sistemas de materia condensada, los electrones carecen de masa efectiva y debemos usar necesariamente la ecuación de Dirac sin masa para describirlos.

Una manera muy conveniente de resolver estas ecuaciones es discretizarlas. Con esto queremos decir colocar una red sobre el espacio — y posiblemente el tiempo — y solamente permitir a la partícula existir en los puntos de dicha red. Cuando hacemos esto, los operadores diferenciales pasan a ser operadores de diferencias finitas y esto permite transformar nuestra ecuación diferencial en una algebraica que puede ser prontamente resuelta por un ordenador. Si esto se hace cuidadosamente, la solución de la versión discreta aproxima la continua si la red es suficientemente fina.

A diferencia de la ecuación de Schrödinger, no es trivial discretizar la ecuación de Dirac. El teorema de Nielsen-Ninomiya demuestra que si intentamos hacerlo ingenuamente, especies de fermiones extra sin significado físico aparecen, dando lugar a varios efectos no deseados. Esto se conoce como *duplicación de fermiones*, y el foco principal de esta tesis es abordar este problema a través del método de *fermiones tangentes*.

Los capítulos 2, 3 y 4 están dedicados a desarrollar varios aspectos de este método. En el capítulo 2, introducimos una manera de utilizarlo para resolver la ecuación de Dirac para fermiones sin masa en una red espacio-temporal. Demostramos que este método es único en cuanto a que evita la duplicación de fermiones y preserva la protección topológica del cono de Dirac.

En el capítulo 3, este enfoque es utilizado para simular la dinámica de un electrón sin masa que se mueve hacia una barrera de potencial. La teoría predice que las partículas sin masa no pueden ser detenidas por la barrera, fenómeno que se como efecto túnel de Klein. Contrastamos nuestro método con otros y mostramos que reproduce el efecto con excelente precisión.

En el capítulo 4, extendemos el método de fermiones tangentes para dar cuenta del efecto de campos magnéticos en los fermiones sin masa. Demostramos cómo nuestro enfoque impide el ensanchamiento del nivel cero de Landau en presencia de desorden magnético, efecto no deseado que de otra forma surge a causa de la duplicación de fermiones.

Los capítulos 5 y 6 no están directamente relacionados con el método de fermiones tangentes pero sí que describen procesos que surgen en materiales con una relación de dispersion de Dirac. En el capítulo 5, estudiamos el efecto de una supercorriente neta distinta de cero paralela a los bordes de un superconductor topológico. Encontramos que la supercorriente puede inducir una “inversión de quiralidad” de los modos de borde de Majorana que existen en este sistema.

En el último capítulo, simulamos numéricamente la inyección de “vórtices de borde” en los bordes de un superconductor topológico. Estos son un tipo de cuasipartículas que teóricamente pueden ser utilizadas para construir un ordernador cuántico tolerante a fallos.

Curriculum Vitæ

I was born in Valladolid, Spain, in 1996. I attended primary and secondary education in Colegio San José and I obtained my high school diploma in 2014, after which I received the *Premio Extraordinario de Bachillerato* awarded by the Autonomous Community of Castilla y León.

Having developed a liking for exact sciences, from 2014 to 2018 I pursued a Bachelor's degree in Physics at the University of Valladolid. There, I had my first experience with research in the summer of 2017, when I interned in the G-FOR research group under the supervision of Dr. J. C. García Escartín. Later that year, I was awarded a grant by the Spanish Ministry of Education to engage in an internship in the department of Theoretical and Atomic Physics and Optics in the same university under the supervision of Prof. dr. J. A. Alonso Martín and Prof. dr. M. J. López Santodomingo. During these years, I also worked part time as a private tutor for high school students.

In 2018, I moved to the Netherlands to pursue a Master's degree in Theoretical Physics in Leiden University. At the Lorentz Institute, I joined the Theoretical Nanophysics group lead by Prof. dr. C. W. J. Beenakker as a Master's student. Being admitted to the Casimir Master Track, I also had the opportunity to work on a short research project in the lab of Dr. S. Goswami in the Technical University of Delft. In 2019, I was employed by Leiden University as a teaching assistant in two different Bachelor's courses. I obtained my Master's degree diploma *summa cum laude* in 2020 and was awarded the Hendrik Casimir prize.

In the same year, I started my Ph.D. studies on the topic of topological states of matter under the supervision of Prof dr. C. W. J. Beenakker and Prof. dr. J Tworzydło. My research first focused in transport properties in mesoscopic topological superconductors, and later shifted towards the development of methods for simulating massless fermions on a lattice. I also worked on the simulation of the dynamics of non-Abelian anyons in a superconducting device while supervising a Master's student. During these years I have attended several schools and conferences, presenting my work in Spain, France, Italy, the Netherlands, Germany and the USA. I have also been a teaching assistant in four different Master's courses and received the Teaching Assistant Prize in the fall of 2022.

List of publications

- A. Donís Vela & J. C. Garcia-Escartin. A quantum primality test with order finding. *Quantum Information and Computation*, **18**, 1143-1151 (2018).

- A. Donís Vela, M. J. López, & J. A. Alonso. Bimetallic Al-Sn clusters: mixing at the nanoscale. *Physical Chemistry Chemical Physics*, **21**, 22919-22929 (2019).

- G. Lemut, A. Donís Vela, M. J. Pacholski, J. Tworzydło & C. W. J. Beenakker. Magnetic breakdown spectrum of a Kramers–Weyl semimetal. *New Journal of Physics*, **22**, 093022 (2020).

- A. Donís Vela, G. Lemut, M. J. Pacholski & C. W. J. Beenakker. Chirality inversion of Majorana edge modes in a Fu–Kane heterostructure. *New Journal of Physics*, **32**, 103006 (2021).

  [Chapter 5 is based on this publication.]

- A. Donís Vela, M. J. Pacholski, G. Lemut, J. Tworzydło & C. W. J. Beenakker. Massless Dirac fermions on a space-time lattice with a topologically protected Dirac cone. *Annalen der Physik*, **534**, 2200206 (2022).

  [Chapter 2 is based on this publication.]

- A. Donís Vela, G. Lemut, M. J. Pacholski, J. Tworzydło & C. W. J. Beenakker. Reflectionless Klein tunneling of Dirac fermions: Comparison of split-operator and staggered-lattice discretization of the Dirac equation. *Journal of Physics: Condensed Matter*, **34**, 364003 (2022).
  [Chapter 3 is based on this publication.]
- A. Donís Vela, G. Lemut, J. Tworzydło & C. W. J. Beenakker. Method to preserve the chiral-symmetry protection of the zeroth Landau level on a two-dimensional lattice. *Annals of Physics*, **456**, 169208 (2023).
  [Chapter 4 is based on this publication.]
- C. W. J. Beenakker, A. Donís Vela, G. Lemut, M. J. Pacholski & J.Tworzydło. Tangent Fermions: Dirac or Majorana fermions on a lattice without fermion doubling. *Annalen der Physik*, **535**, 2300081 (2023).
  [Part of chapter 1 is based on this publication.]
- I. M. Flór, A. Donís Vela, C. W. J. Beenakker & G. Lemut. Dynamical simulation of the injection of vortices into a Majorana edge mode. *Physical Review B*, **108**, 235309 (2023).
  [Chapter 6 is based on this publication.]

Stellingen

behorende bij het proefschrift

Tangent fermions: massless fermions on a lattice

1. The topological protection of a single Dirac cone on a space-time lattice requires not only chiral symmetry, but also the continuity of the evolution operator in the reciprocal space. [Chapter 2]
2. It is impossible to have a gauge invariant lattice formulation of massless fermions with a single topologically protected zeroth Landau level. [Chapter 4]
3. In a topological superconductor, a supercurrent cannot produce an inversion of velocity of the Majorana edge modes if the pairing is p-wave. [Chapter 5]
4. The injection of edge-vortices in a topological superconductor can be spoiled by the entrapment of excitations in the Josephson junction of the injector. [Chapter 6]
5. A zigzag-edge boundary condition for Dirac fermions can be replaced by a large vector potential parallel to the boundary.
6. The thermal-metal-insulator transition in a chiral p-wave superconductor is a percolation transition for Majorana fermions.
7. The exceptional points of a non-Hermitian Hamiltonian do not produce a singularity in the Josephson effect.
8. Although the Hamiltonian for tangent fermions is non-local, it can be written as a matrix product operator of finite bond dimension.
9. Within a given research area, there is a negative correlation between the length of the title of a scientific article and its quality.

Álvaro Donís Vela
Leiden, 3 juli 2024